NASA-CR-162524
19800005893

The Deep Space Network Progress Report 42-54

September and October 1979

December 15, 1979

National Aeronautics and
Space Administration

Jet Propulsion Laboratory
California Institute of Technology
Pasadena, California

The Deep Space Network Progress Report 42-54

September and October 1979

December 15, 1979

National Aeronautics and
Space Administration

Jet Propulsion Laboratory
California Institute of Technology
Pasadena, California

The research described in this publication was carried out by the Jet Propulsion Laboratory, California Institute of Technology, under NASA Contract No NAS7-100

Preface

This report presents DSN progress in flight project support, tracking and data acquisition (TDA) research and technology, network engineering, hardware and software implementation, and operations Each issue presents material in some, but not all, of the following categories in the order indicated

Description of the DSN

Mission Support
- Ongoing Planetary/Interplanetary Flight Projects
- Advanced Flight Projects

Radio Astronomy

Special Projects

Supporting Research and Technology
- Tracking and Ground-Based Navigation
- Communications-Spacecraft/Ground
- Station Control and Operations Technology
- Network Control and Data Processing

Network and Facility Engineering and Implementation
- Network
- Network Operations Control Center
- Ground Communications
- Deep Space Stations
- Quality Assurance

Operations
- Network Operations
- Network Operations Control Center
- Ground Communications
- Deep Space Stations

Program Planning
- TDA Planning

In each issue, the part entitled "Description of the DSN" describes the functions and facilities of the DSN and may report the current configuration of one of the seven DSN systems (Tracking, Telemetry, Command, Monitor & Control, Test & Training, Radio Science, and Very Long Baseline Interferometry)

The work described in this report series is either performed or managed by the Tracking and Data Acquisition organization of JPL for NASA.

This Page Intentionally Left Blank

Contents

DESCRIPTION OF THE DSN

MISSION SUPPORT

Ongoing Planetary/Interplanetary Flight Projects

SUPPORTING RESEARCH AND TECHNOLOGY

Communications – Spacecraft/Ground

Station Control and Operations Technology

NETWORK AND FACILITY ENGINEERING AND IMPLEMENTATION

Network

Deep Space Stations

Network Functions and Facilities

N A Renzetti
Office of Tracking and Data Acquisition

The objectives, functions, and organization of the Deep Space Network are summarized, deep space station, ground communication, and network operations control capabilities are described

The Deep Space Network was established by the National Aeronautics and Space Administration (NASA) Office of Space Tracking and Data Systems and is under the system management and technical direction of the Jet Propulsion Laboratory (JPL) The network is designed for two-way communications with unmanned spacecraft traveling approximately 16,000 km (10,000 miles) from Earth to the farthest planets and to the edge of our solar system It has provided tracking and data acquisition support for the following NASA deep space exploration projects Ranger, Surveyor, Mariner Venus 1962, Mariner Mars 1964, Mariner Venus 1967, Mariner Mars 1969, Mariner Mars 1971, and Mariner Venus-Mercury 1973, for which JPL has been responsible for the project management, the development of the spacecraft, and the conduct of mission operations, Lunar Orbiter, for which the Langley Research Center carried out the project management, spacecraft development, and conduct of mission operations, Pioneer, for which Ames Research Center carried out the project management, spacecraft development, and conduct of mission operations, and Apollo, for which the Lyndon B Johnson Space Center was the project center and the Deep Space Network supplemented the Manned Space Flight Network, which was managed by the Goddard Space Flight Center The network is currently providing tracking and data acquisition support for Helios, a joint U S /West German project, Viking, for which Langley Research Center provided the Lander spacecraft and project management until May, 1978, at which time project management and mission operations were transferred to JPL, and for which JPL provided the Orbiter spacecraft, Voyager, for which JPL provides project management, spacecraft development, and is conducting mission operations, and Pioneers, for which the Ames Research Center provides project management, spacecraft development, and conduct of mission operations The network is adding new capability to meet the requirements of the Galileo mission to Jupiter, for which JPL is providing the Orbiter spacecraft, and

the Ames Research Center the probe In addition, JPL will carry out the project management and the conduct of mission operations

The Deep Space Network (DSN) is one of two NASA networks The other, the Spaceflight Tracking and Data Network (STDN), is under the system management and technical direction of the Goddard Space Flight Center (GSFC) Its function is to support manned and unmanned Earth-orbiting satellites The Deep Space Network supports lunar, planetary, and interplanetary flight projects

From its inception, NASA has had the objective of conducting scientific investigations throughout the solar system It was recognized that in order to meet this objective, significant supporting research and advanced technology development must be conducted in order to provide deep space telecommunications for science data return in a cost effective manner Therefore, the Network is continually evolved to keep pace with the state of the art of telecommunications and data handling It was also recognized early that close coordination would be needed between the requirements of the flight projects for data return and the capabilities needed in the Network This close collaboration was effected by the appointment of a Tracking and Data Systems Manager as part of the flight project team from the initiation of the project to the end of the mission By this process, requirements were identified early enough to provide funding and implementation in time for use by the flight project in its flight phase

As of July 1972, NASA undertook a change in the interface between the Network and the flight projects Prior to that time, since 1 January 1964, in addition to consisting of the Deep Space Stations and the Ground Communications Facility, the Network had also included the mission control and computing facilities and provided the equipment in the mission support areas for the conduct of mission operations The latter facilities were housed in a building at JPL known as the Space Flight Operations Facility (SFOF) The interface change was to accommodate a hardware interface between the support of the network operations control functions and those of the mission control and computing functions This resulted in the flight projects assuming the cognizance of the large general-purpose digital computers which were used for both network processing and mission data processing They also assumed cognizance of all of the equipment in the flight operations facility for display and communications necessary for the conduct of mission operations The Network then undertook the development of hardware and computer software necessary to do its network operations control and monitor functions in separate computers A characteristic of the new interface is that the Network provides direct data flow to and from the stations, namely, metric data, science and engineering telemetry, and such network monitor data as are useful to the flight project This is done via appropriate ground communication equipment to mission operations centers, wherever they may be.

The principal deliveries to the users of the Network are carried out by data system configurations as follows

(1) The DSN Tracking System generates radio metric data, i e , angles, one- and two-way doppler and range, and transmits raw data to Mission Control

(2) The DSN Telemetry System receives, decodes, records, and retransmits engineering and scientific data generated in the spacecraft to Mission Control

(3) The DSN Command System accepts spacecraft commands from Mission Control and transmits the commands via the Ground Communications Facility to a Deep Space Station The commands are then radiated to the spacecraft in order to initiate spacecraft functions in flight

(4) The DSN Radio Science System generates radio science data, i e , the frequency and amplitude of spacecraft transmitted signals affected by passage through media such as the solar corona, planetary atmospheres, and planetary rings, and transmits these data to Mission Control

(5) The DSN Very Long Baseline Interferometry System generates time and frequency data to synchronize the clocks among the three Deep Space Communications complexes It will generate universal time and polar motion and relative Deep Space Station locations as by-products of the primary data delivery function

The data system configurations supporting testing, training, and network operations control functions are as follows

(1) The DSN Monitor and Control System instruments, transmits, records, and displays those parameters of the DSN necessary to verify configuration and validate the Network It provides the tools necessary for Network Operations personnel to control and monitor the Network and interface with flight project mission control personnel

(2) The DSN Test and Training System generates and controls simulated data to support development, test, training and fault isolation within the DSN It participates in mission simulation with flight projects

The capabilities needed to carry out the above functions have evolved in the following technical areas

(1) The Deep Space Stations, which are distributed around Earth and which, prior to 1964, formed part of the Deep Space Instrumentation Facility The technology involved in equipping these stations is strongly related to the state of the art of telecommunications and flight-ground design considerations, and is almost completely multimission in character

(2) The Ground Communications Facility provides the capability required for the transmission, reception, and monitoring of Earth-based, point-to-point communications between the stations and the Network Operations Control Center at JPL, Pasadena, and to the JPL Mission Operations Centers Four communications disciplines are provided teletype, voice, high-speed, and wideband The Ground Communications Facility uses the capabilities provided by common carriers throughout the world, engineered into an integrated system by Goddard Space Flight Center, and controlled from the communications Center located in the Space Flight Operations Facility (Building 230) at JPL

The Network Operations Control Center is the functional entity for centralized operational control of the Network and interfaces with the users It has two separable functional elements, namely, Network Operations Control and Network Data Processing The functions of the Network Operations Control are

(1) Control and coordination of Network support to meet commitments to Network users

(2) Utilization of the Network data processing computing capability to generate all standards and limits required for Network operations

(3) Utilization of Network data processing computing capability to analyze and validate the performance of all Network systems

The personnel who carry out the above functions are located in the Space Flight Operations Facility, where mission operations functions are carried out by certain flight projects Network personnel are directed by an Operations Control Chief The functions of the Network Data Processing are

(1) Processing of data used by Network Operations Control for control and analysis of the Network

(2) Display in the Network Operations Control Area of data processed in the Network Data Processing Area

(3) Interface with communications circuits for input to and output from the Network Data Processing Area

(4) Data logging and production of the intermediate data records

The personnel who carry out these functions are located approximately 200 meters from the Space Flight Operations Facility The equipment consists of minicomputers for real-time data system monitoring, two XDS Sigma 5s, display, magnetic tape recorders, and appropriate interface equipment with the ground data communications

DSN Radio Science System, Mark III-80

A L Berman
TDA Engineering Office

This article describes the key characteristics, functional operation, and functional requirements of the DSN Radio Science System, Mark III-80 Particularly emphasized is "medium bandwidth" capability, which will enable support of the Voyager Saturn Ring Experiment in November 1980

I. Introduction

The DSN Radio Science System, Mark III-80, is one of eight DSN Data Systems which provide major data types and functional capabilities to the flight projects In the broadest sense, the DSN Data Systems encompass the equipment, software, personnel, documentation, procedures, and resources necessary to deliver the required data to the flight projects The Radio Science System was brought into existence on February 4, 1977, at which time the system requirements were reviewed and accepted by the Radio Science Review Board, The February 4, 1977 Radio Science Requirements Review has been described by Mulhall (Ref 1)

The DSN Radio Science System, Mark III-78, configuration has been described in detail in a previous report (Ref 2) The major difference between the Mark III-78 and Mark III-80 configurations is the addition of the capability necessary to support the Voyager Saturn Ring Experiment Hence, it is the new capabilities being implemented in support of the Saturn Ring Experiment which will serve as the focus of this article

A. Radio Science System Definition

The DSN Radio Science System is defined as follows

> The DSN Radio Science System generates radio science data (digitized amplitude samples) from spacecraft signals which are both left circularly polarized (LCP) and right circularly polarized (RCP) and are at S-band and X-band frequencies The radio science data bandwidth is reduced in either real time or nonreal time via differencing with a predicted signal profile Bandwidth-reduced radio science data are delivered to the project via computer-compatible magnetic tape
>
> The DSN Radio Science System additionally provides real-time graphical displays of both radio metric and radio science data

Figure 1 illustrates the Radio Science System functions and interfaces The Radio Science System functional block dia-

gram is shown in Fig 2 Note that Fig 2 also includes DSN Tracking System functional capabilities, which deliver the closed-loop radio science (radio metric) data Finally, Fig 3 illustrates the Radio Science System functions and data flow

B. Radio Science System Key Characteristics

The key characteristics of the DSN Radio Science System, Mark III-80, are as follows

(1) Acquires left and right circularly polarized spacecraft signals at S- and X-band frequencies

(2) Digitizes and bandwidth-reduces up to four open-loop receiver channels simultaneously by means of an automatically controlled programmed oscillator

(3) Digitizes and records wide bandwidth open-loop receiver output

(4) Generates programmed oscillator frequency predictions that incorporate refractive effects due to planetary atmospheres

(5) Performs real-time system performance monitoring and provides system performance data in real time to the project

(6) Transmits radio science data from the Deep Space Stations (DSSs) to the Network Operations Control Center (NOCC) via Wideband Data Line (WBDL)

(7) Performs nonreal-time bandwidth reduction of wide bandwidth radio science data

(8) Provides wide bandwidth backup of all unique radio science events

(9) Provides radio science data to the project via computer-compatible magnetic tape

C. Flight Project Users of the DSN Radio Science System

Flight projects with active spacecraft supported by the Radio Science System are

(1) Voyager

(2) Pioneer Venus

(3) Pioneer Saturn

(4) Helios

(5) Viking

New or anticipated flight projects that can be expected to utilize the Radio Science System are

(1) Solar Polar

(2) Galileo

(3) VOIR

(4) Solar Probe

II. Radio Science System Functional Description

The DSN Radio Science System, Mark III-80, provides four major functional capabilities

(1) *Wide Bandwidth Recording and Subsequent Nonreal-Time Bandwidth Reduction.* Wide bandwidth is defined as being greater than 500 kHz Wide bandwidth recording and subsequent nonreal-time bandwidth reduction capability was initially implemented to support the Pioneer Venus DLBI Experiment, and since has been utilized to provide a wide bandwidth backup for occultation operations

(2) *Real-Time Bandwidth Reduction*[1] *(Narrow/Very Narrow Bandwidth)* Narrow bandwidth is defined as being between 1 kHz and 50 kHz, while very narrow bandwidth is defined as being less than 1 kHz Real-time bandwidth reduction is utilized in support of solar corona experiments (very narrow bandwidth) and planetary occultation experiments (narrow bandwidth)

(3) *Real-Time Bandwidth Reduction (Medium Bandwidth)* Medium bandwidth is defined as being between 50 kHz and 500 kHz Real-time bandwidth reduction (medium bandwidth) capability will be used to support the Voyager Saturn Ring Experiment

(4) *Real-Time System Performance Validation* This capability provides graphical displays of both radio science and radio metric data to the Network Operations Control Team and the appropriate flight project

Wide bandwidth recording and subsequent nonreal-time bandwidth reduction, real-time bandwidth reduction (narrow/very narrow bandwidth), and real-time system performance validation were described in detail in Ref 2 A detailed functional description of real-time bandwidth reduction (medium bandwidth) is presented in Section III

[1] The expression "real-time bandwidth reduction" is here defined as the process of programming the open-loop receiver local oscillator with frequency predictions, and subsequently filtering, digitizing, and recording a narrow baseband bandwidth containing the hetrodyned signal

III. Real-Time Bandwidth Reduction (Medium Bandwidth) Functional Description

As previously described, real-time bandwidth reduction (medium bandwidth) capability is being implemented to support the Voyager Saturn Ring Experiment The goals of the Saturn Ring Experiment are described by Eshleman et al (Ref 3) as follows

> "The goals of these observations are to measure the complex (amplitude and phase) radio extinction and angular scattering function of the rings as a function of wavelength, polarization, and radial distance from Saturn These observations would then be used to infer the first several moments of the ring particle size distribution, the total amount of material in the rings, the radial distribution of that material, and limits to possible particle shapes and constituents "

The functional description of real-time bandwidth reduction (medium bandwidth) is categorized below by subsystem functions

A. The Network Operations Control Center (NOCC) Radio Science Subsystem (NRS)

The NRS provides two main functions during the Saturn Ring Experiment Radio Science predictions and real-time system performance validation

Radio science predictions are generated by the "POEAS" software program following receipt from the flight project of a spacecraft state vector The POEAS program generates frequency-independent observables which have been corrected for planetary atmospheric refraction These data are written on a magnetic tape (polynominal coefficient tape or PCT) and are passed to the NOCC Support Subsystem

In performing real-time system performance validation, digital data originating from the (DSS) Spectral Signal Indicator (SSI) are reconstructed into spectral displays and are provided on digital television in NOCC and the project radio science area via the NOCC Display Subsystem

B. The NOCC Support Subsystem (NSC)

The NSC utilizes the software program "PREDIK" to generate frequency-dependent radio science predictions for the Deep Space Stations (DSSs) Inputs are the PCT from the NRS and spacecraft frequencies from the flight project The output is radio science predictions which are transmitted via High-Speed Data Line (HSDL) to the DSS Radio Science Subsystem (DRS)

C. The DSS Antenna Microwave Subsystem (UWV)

The UWV provides S- and X-band signals that are both right circularly polarized (RCP) and left circularly polarized (LCP) via an orthomode polarizer The UWV functional block diagram is seen in Fig 4.

D. The DSS Receiver-Exciter Subsystem (RCV)

The RCV provides two main functions during the Saturn Ring Experiment acquisition of four signals simultaneously and real-time spectral analysis of a reconstructed analog signal received from the DRS

The RCV utilizes the four-channel medium bandwidth Multimission Open-Loop Receiver (MMR) to acquire the four signals (permutations of S- and X-band, and LCP and RCP) simultaneously The MMR contains a programmed oscillator which heterodynes the signals down from S- and X-band to medium bandwidth The programmed oscillator is driven by a (predicted) frequency profile provided by the DRS The output medium bandwidth signals are appropriately filtered and provided to the Medium Bandwidth Converter Subassembly of the DRS The programmed oscillator frequency (initially at 41 MHz) is heterodyned down to the MHz level and provided to the DRS for recording A functional block diagram of the MMR is seen in Fig 5

During MMR operations, the RCV is provided a reconstructed medium bandwidth signal by the DRS This signal is analyzed by the Spectral Signal Indicator (SSI), with the output being real-time spectrum displays These displays are provided to the DRS in digital form for eventual display via the NRS

E. The DSS Radio Science Subsystem (DRS)

The DRS has the major functions of providing the predicted doppler profile to the MMR programmed oscillator and the subsequent digitization and recording of the receiver medium bandwidth output signals

Radio science predictions in the form of frequency and time pairs are received by the Occultation Data Assembly (ODA) These are converted to an initial frequency and subsequent frequency rates and provided to the MMR Programmed Oscillator Control Assembly

The four signals output by the MMR are digitized by the Medium Bandwidth Converter Subassembly of the ODA and recorded on the Digital Recording Assembly (DRA) The

MMR provides the down-converted programmed oscillator frequency to the Frequency Monitor Subassembly (FMS), where it is counted and recorded by the ODA The ODA also records the frequency predictions provided to the programmed oscillator, as well as the commanded programmed oscillator frequencies on integer second intervals

A reconstructed analog signal is provided to the SSI of the RCV, and the resulting digital spectrum data from the SSI are received by the ODA, and formatted for and transmitted via WBDL to NOCC

The ODA provides real-time status, configuration, and alarm data locally via the DSS Monitor and Control Subsystem and via HSDL to the NOCC

Subsequent to the generation of radio science data, the ODA and DRA recorded tapes are shipped to the Network Radio Science Subsystem (WRS) for further processing A functional block diagram of the DRS is provided in Fig 6, while Fig 7 provides a DRA functional block diagram

F. The Network (NWK) Radio Science Subsystem (WRS)

The WRS receives the DRA recorded data from the DSS, plays back the DRA recorded data and rewrites (one signal per pass through) the digitized data onto computer-compatible tapes These tapes plus the ODA recorded tapes, which contain the programmed oscillator information, constituting the sum total of radio science data, are then delivered to the flight project

IV. Real-Time Bandwidth Reduction (Medium Bandwith) Functional Requirements

The functional requirements for real-time bandwidth reduction (medium bandwidth) are presented below

A. Radio Frequency Bands

The Radio Science System shall acquire spacecraft signals at S- and X-bands

B. Signal Polarization

Medium bandwidth requirements are for simultaneous reception of both RCP and LCP at both S- and X-bands

C. System Noise Temperature

(1) Calibration precision 1%

(2) Accuracy at 0 1-second sample interval 2%

(3) Stability over one pass 10%

D. Radio Frequency Phase Stability

The Radio Science System shall provide a highly phase-stable radio frequency (RF) signal acquisition capability, specific medium bandwidth requirements are stated as follows

(1) The maximum deviation after calibration from an ideal linear phase response shall be

(a) Single S-band channel 36° or less

(b) Single X-band channel 132° or less

(c) Differenced S - X channel S-band minus 3/11 · X-band, less than 10°

(d) Differenced RCP minus LCP channels, at both S- and X-bands, less than 1°

(2) Phase response measurement conditions are

(a) Signal measured at the filtered receiver output and across the spanned -1 dB bandwidth

(b) 100-second measurement period

E. Programmed Oscillator Control

The receiver first local oscillator shall be automatically controlled to follow a predicted frequency versus time profile

F. Output Bandwidths

Specific medium bandwidth requirements for the output ("sampled") bandwidth are as follows

(1) 50 kHz for LCP and RCP S-band

(2) 150 kHz for LCP and RCP X-band

G. Radio Frequency Amplitude Response

The multimission Radio Science System amplitude response requirements are

(1) The 100 percent bandwidth shall be defined as the "sampled" bandwidth

(2) The "usable" bandwidth, defined by the -1 dB points, shall be $\geqslant 83$ percent of the sampled bandwidth

(3) ±37 percent of the (sampled) bandwidth relative to the bandpass center shall have an amplitude ripple of less than ±0 2 dB

(4) The "rejection" bandwidth, defined by the -23 dB points, shall be $\leqslant 117$ percent of the sampled bandwidth

H. Analog to Digital (A-D) Conversion

Analog to digital conversion shall be performed with $\geq$ 8-bit quantization

I. Timing Information

Data shall be time-tagged to the following specifications

(1) *Time Offset* Time tag offset from station time shall be less than 10 microseconds

(2) *Sampling Rate Accuracy* Sampling rate accuracy $(\Delta F/F)$ shall be better than $10^{-5} \cdot (\text{bandwidth})^{-1}$.

(3) *Sampling Jitter* Sampling jitter shall be less than $(2^8 \cdot \text{bandwidth})^{-1}$

J. Programmed Oscillator Frequency Recording

Programmed oscillator frequency output shall be time-tagged and recorded as follows

(1) *Counted Frequency Recording.* The programmed oscillator frequency shall be counted and recorded at one-second intervals on the integer second

(2) *Counted Frequency Accuracy* The counted programmed oscillator frequency shall be accurate to 0 5 Hz at S-band (RMS)

(3) *Commanded Frequency Recording* The commanded programmed oscillator frequency shall be recorded at one-second intervals on the integer second

(4) *Predicted Frequency Recording* The predicted programmed oscillator initial frequency and subsequent frequency rates shall be recorded

K. Data Return

Data shall be provided to the flight project on computer-compatible tape

V. Implementation Schedule

Medium bandwidth capability is required to be implemented at DSS 63 by April 1, 1980 Specific elements include

(1) Medium bandwidth data handling (ODA, DRA)

(2) SSI remote display (SSI, ODA, NRS)

(3) Radio science data return via WBDL

(4) DRS-NRS interface via HSDL

(5) Medium bandwidth MMR

(6) X-band orthomode (UWV)

(7) Four channel wide bandwidth backup (RCV, DRA)

(8) Precision Power Monitor (PPM)

References

1 Mulhall, B D L., "DSN Radio Science System Description and Requirements," in *The Deep Space Network Progress Report 42-39*, pp 119-129, Jet Propulsion Laboratory, Pasadena, Calif , June 15, 1977

2 Berman, A L , "DSN Radio Science System, Mark III-78," in *The Deep Space Network Progress Report 42-47*, pp 4-13, Jet Propulsion Laboratory, Pasadena, Calif , Oct 15, 1978

3 Eshleman, V R., et al., "Radio Science Investigations with Voyager," *Space Science Reviews*, Vol 21, 1977

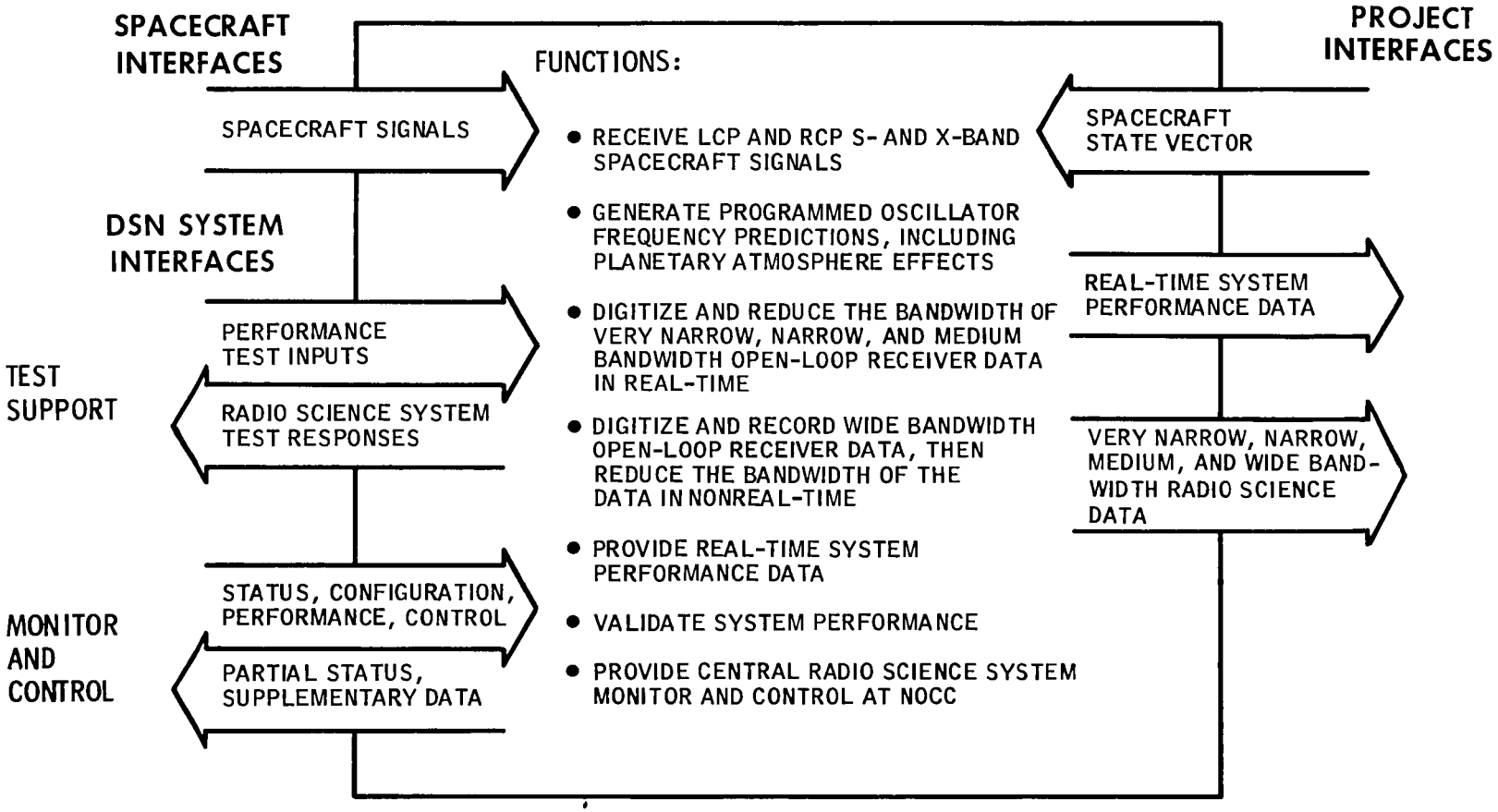

Fig. 1 Radio Science System, Mark III-80, functions and interfaces

This Page Intentionally Left Blank

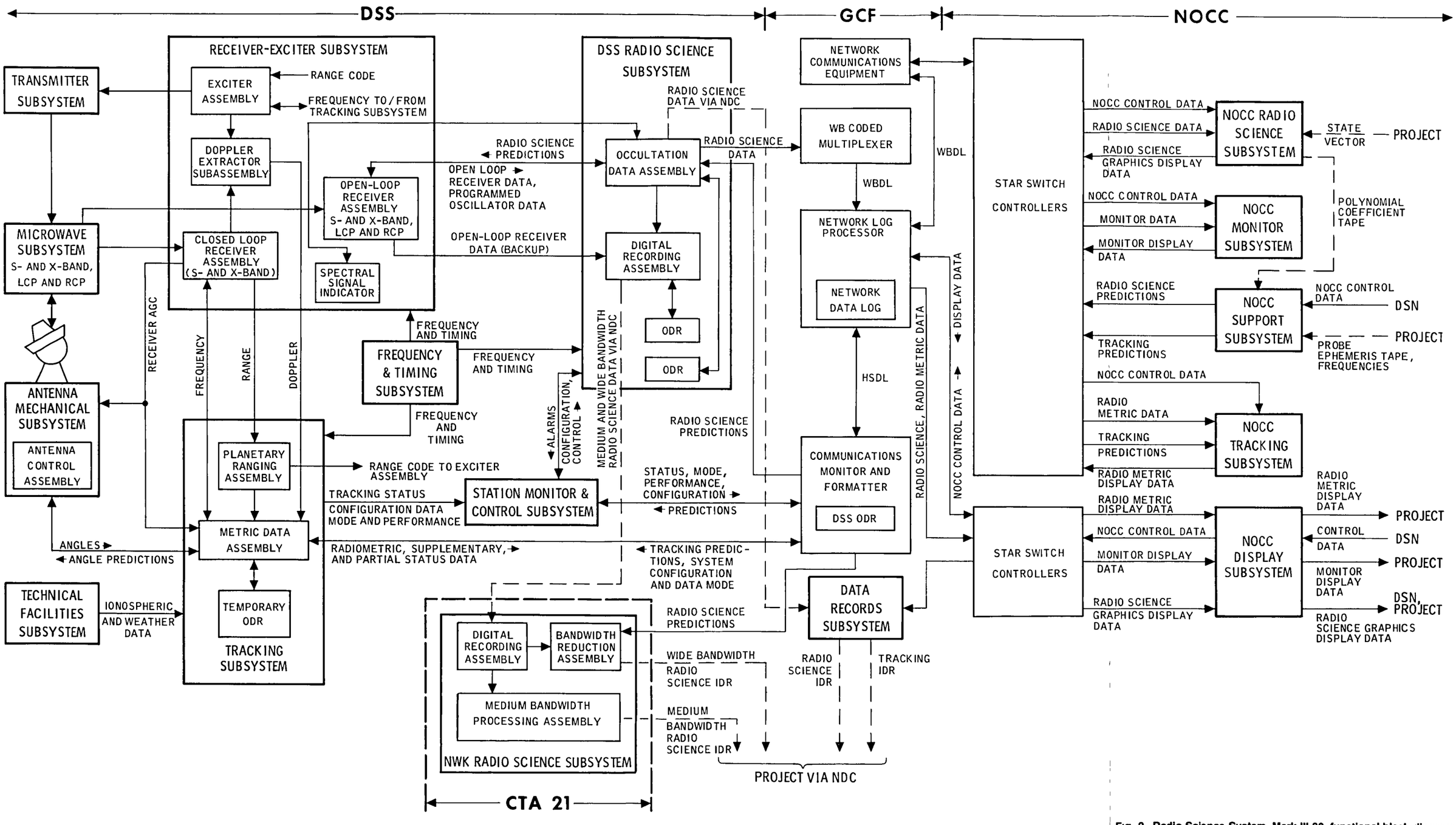

Fig. 2. Radio Science System, Mark III-80, functional block diagram

This Page Intentionally Left Blank

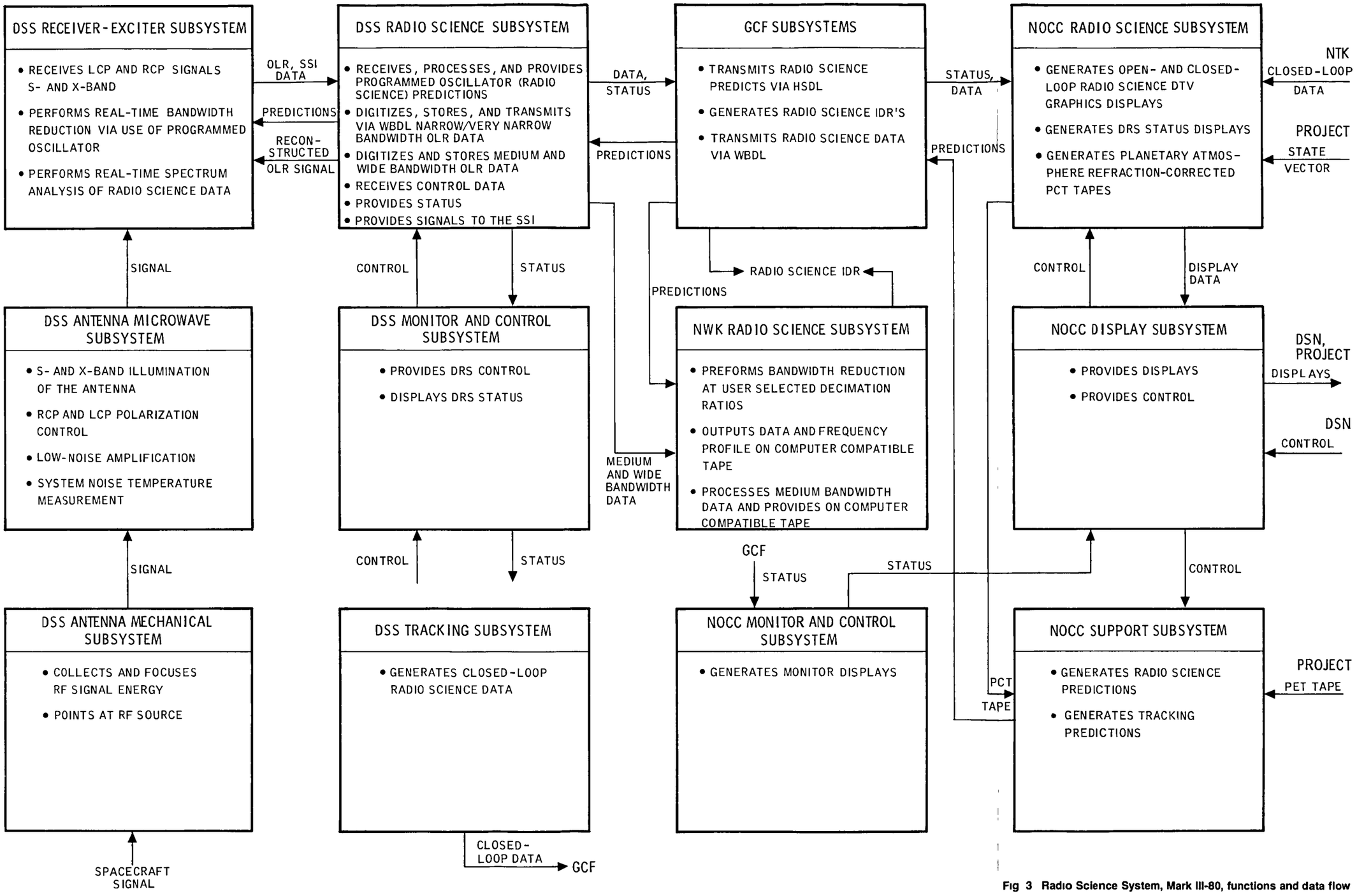

Fig 3 Radio Science System, Mark III-80, functions and data flow

This Page Intentionally Left Blank

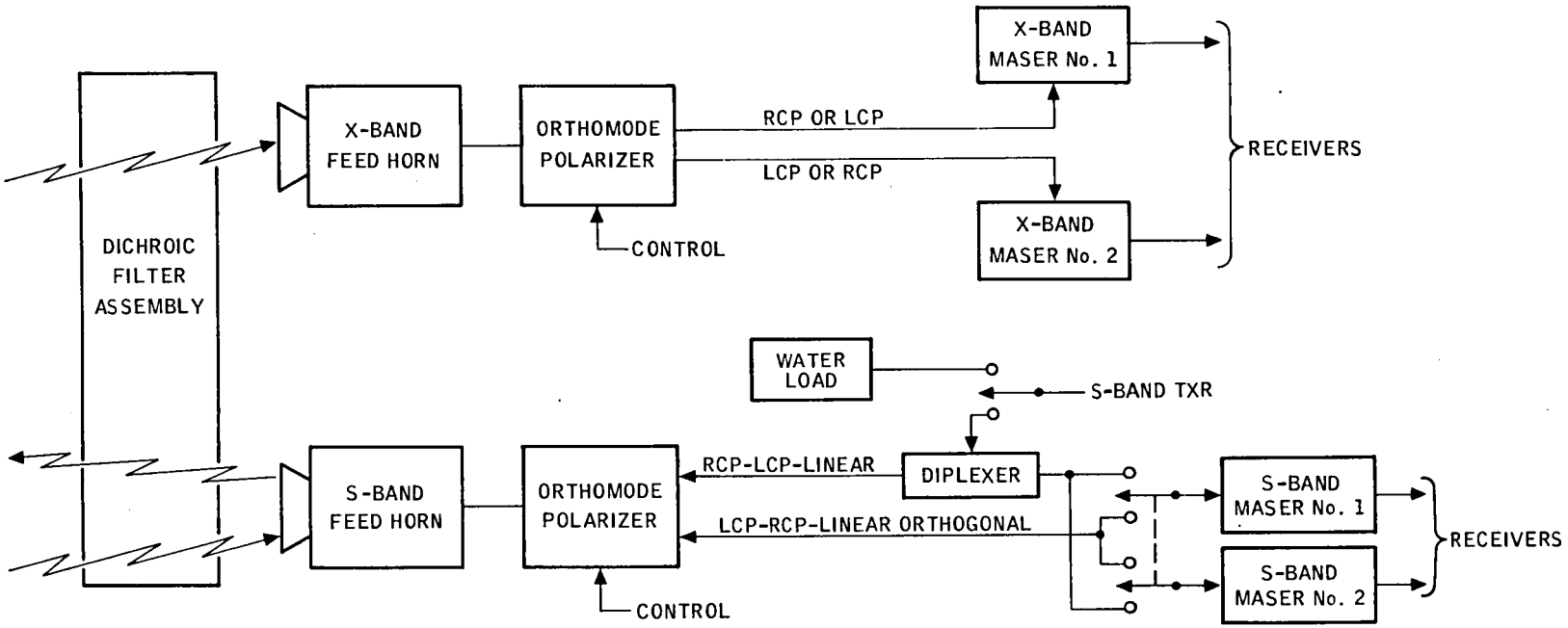

Fig. 4. DSS Antenna Microwave Subsystem functional block diagram—orthomode polarizer

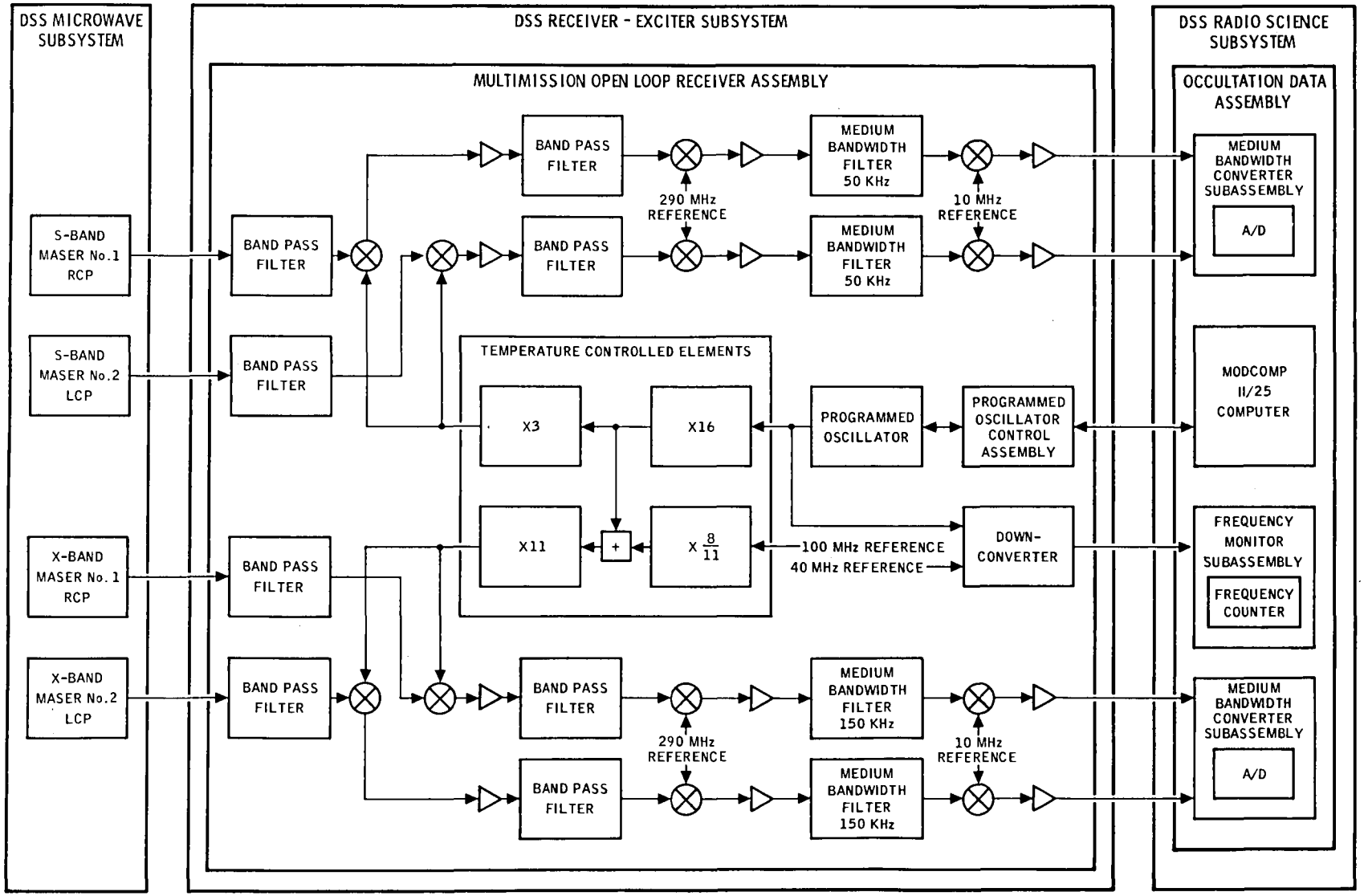

Fig. 5. DSS Receiver-Exciter Subsystem functional block diagram—Multimission Open-Loop Receiver (MMR)

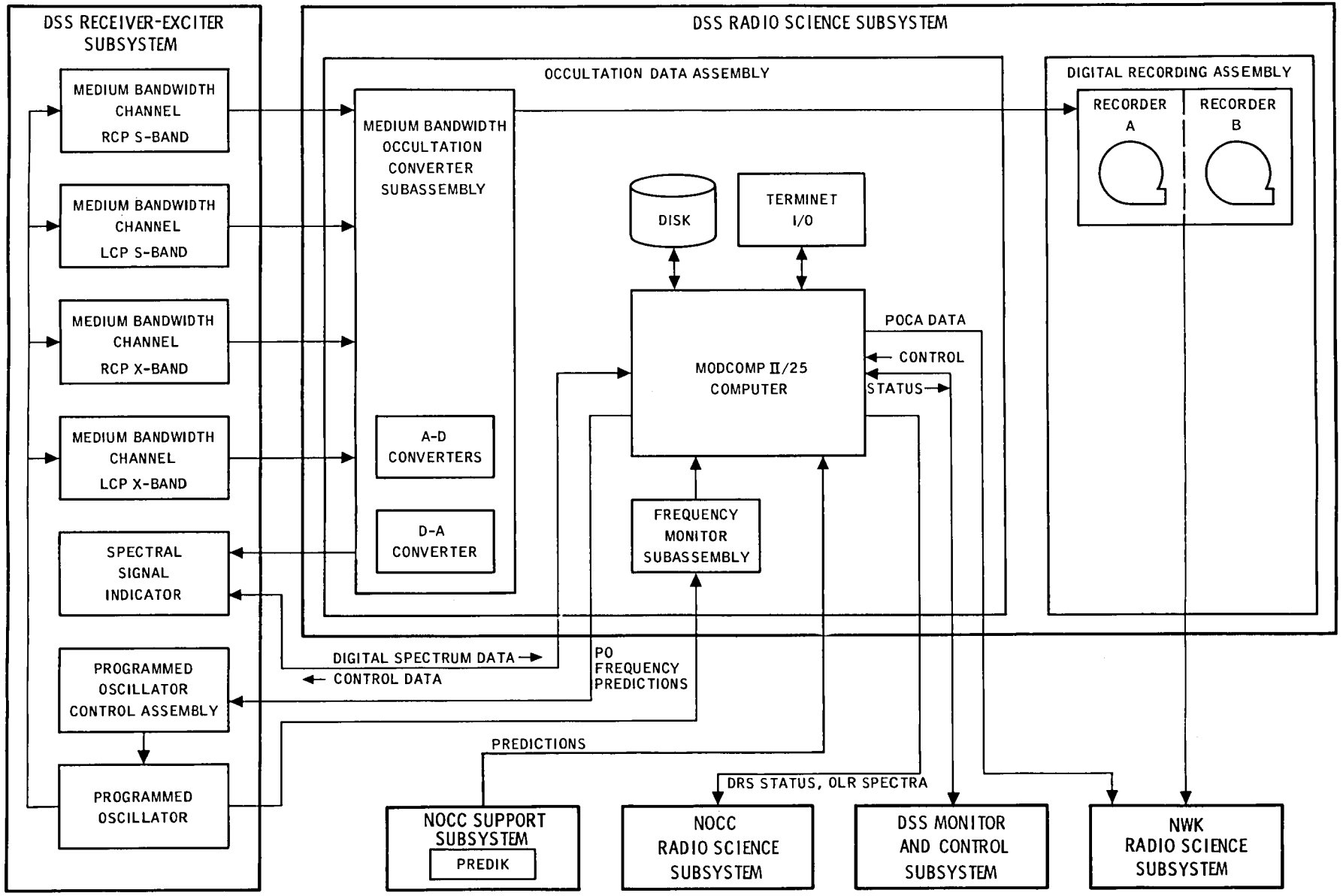

Fig. 6. DSS Radio Science Subsystem functional block diagram—medium bandwidth configuration

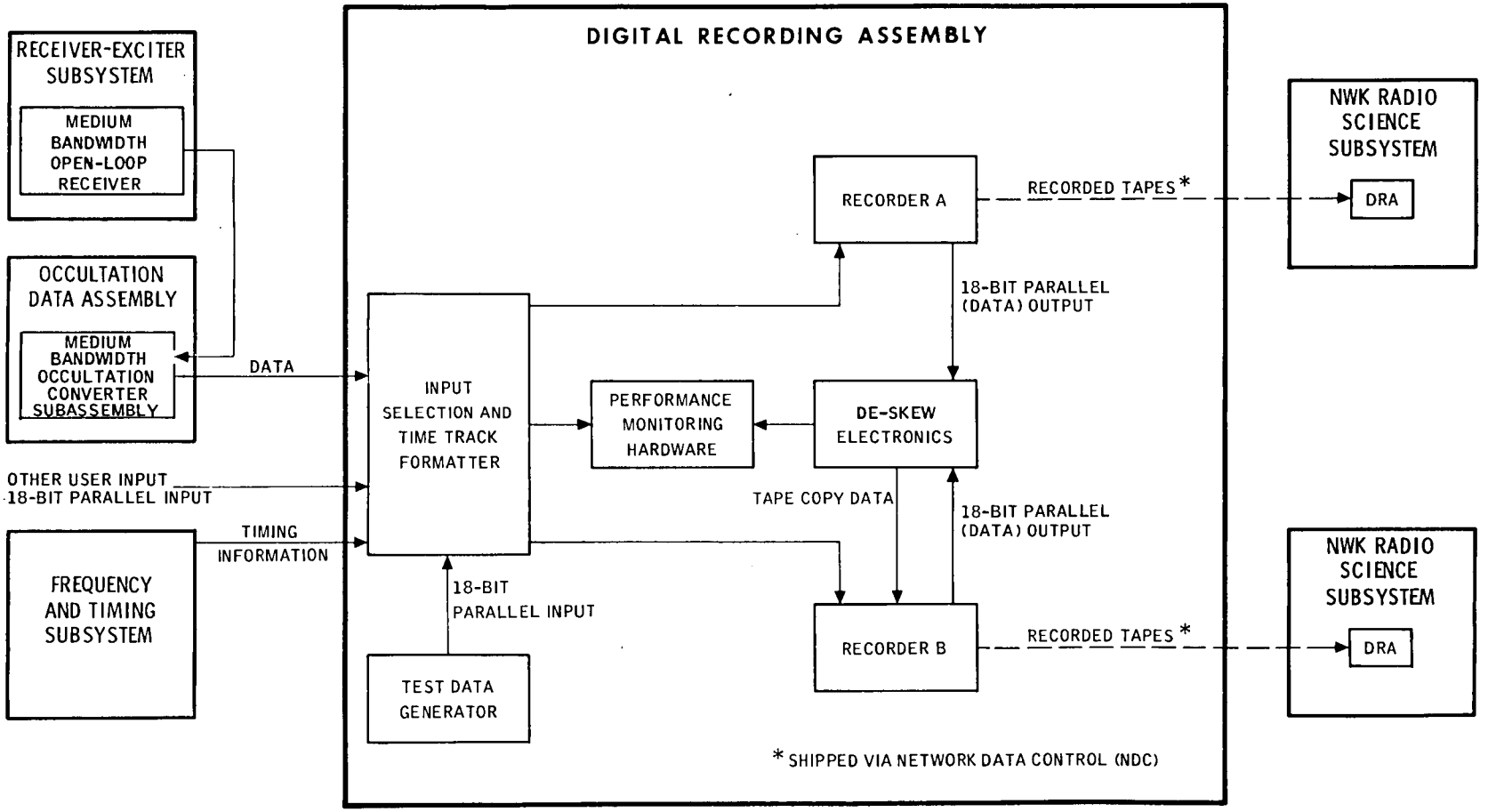

Fig. 7. Digital Recording Assembly functional block diagram—medium bandwidth configuration

Voyager Mission Support

N. Fanelli and H. Nance
Deep Space Network Operations Section

This is a continuation of the Deep Space Network report on tracking and data acquisition for Project Voyager. This report covers the postencounter period for Voyager 2 and the Saturn cruise period for Voyager 1, August-September 1979.

I. Introduction

Voyager 1 continued in its Saturn Cruise phase with solar conjunction activities during the period of August 8 through 20, 1979. Voyager 2 completed the Post Encounter activities on August 28, 1979 and entered the Saturn Cruise phase. Solar conjunction activities were observed during the period August 8 through 29, 1979.

II. DSN Operations

A. Radio Science

One of the primary activities supported by the DSN during July and August was the special radio science activity conducted during the solar conjunction of both Voyager spacecraft and Pioneer spacecraft.

1. Experiment objective. The solar conjunction provided the Voyager Project with the unique opportunity to perform observations of the solar wind and solar corona as the ray paths from the Voyager spacecraft passed near the Sun. The observations greatly enhanced the knowledge of variations of the solar wind and corona in the region of the Sun. When combined with observations taken nearly simultaneously from Pioneer 11 and Pioneer Venus orbiter, the data are expected to yield important new information related to the plasma distribution near the disc of the Sun and over its north pole. The listing below outlines representative dates and changes in the Sun-Earth-probe (SEP) angle during the solar conjunction.

Date, 1979	Voyager 1, deg	Voyager 2, deg
August 2	14	8
August 8	11	5
August 12	7	2
August 14	6	1
August 16	4	2
August 18	3	3
August 20	2	4
August 21	1	5
August 24	2	7
August 26	3	8
August 28	4	9
August 29	5	10
September 1	7	12

Forty seven passes were scheduled for support of the solar conjunction activity; 24 passes were scheduled for Goldstone, Calif., 9 passes for Canberra, Australia, and 14 passes for Madrid, Spain. Each of the Voyager 2 passes required four

hours of occultation data assembly (ODA) recording, and Voyager 1 passes required three hours of ODA recording. Data collection began on July 24, 1979, from Madrid, on July 31 from Goldstone and on August 8 from Canberra.

2. Station configuration. Special configuration, and in some cases extra equipment, was required during the support recording period. The extra equipment comprised an open loop receiver (OLR) and a multi-mission receiver (MMR) used to provide data to the ODA recorder. The standard closed loop receiver configuration for S-band and X-band radio metric data was used with selected doppler sample rates as specified for the particular pass.

The MMR/ODA equipment was used for the open loop data at Goldstone and Madrid, and the OLR/ODA equipment was used at Canberra. Filters, sample rates, and record number were changed during the activity based on experience gained and modified requirements. 1-kHz S-band and 3-kHz X-band filters were selected initially with 2000 sample/second and 8 bits quantization sample rate. Later, after special installation, 100-Hz filters were used with 200 sample/second and 8 bits quantization for S/X-band.

With the 1/3-kHz filters, Goldstone and Madrid calibrated the MMR output/ODA input power level for S/X-band at plus 16 dBm. Canberra OLR output/ODA input power level for the S/X-band was set at plus 12 dbm. With the 100-Hz filter used at all stations for S/X-band, the ODA input power level was set at plus 20 dBm.

Special ODA predicts were generated and made available from JPL for one- and two-way spacecraft modes. To minimize tape usage, the number of ODA records was initially set at 29,000 records or a record time per tape of 4.1 hours, but later changed to 25,000 records or 3.5 hours of data to insure that all data was included on one tape.

As the SEP became smaller, it was found that the solar plasma exceeded prediction and the 100-Hz bandwidth was exceeded. The stations were instructed to return to the 1/3-kHz filters and the 2000 sample/second and 8 bits quantization sample rate. The signal noise temperature (SNT) also increased with the decrease in SEP, and it became necessary to reduce the MMR/OLR output power to the ODA to prevent saturation. Solar activity was more intense than expected; therefore, a table of SNT vs MMR/OLR output power reduction was required. The resultant values were:

SNT, K	Reduction in MMR/OLR output, dB
40	1
80	2
125	3
200	4
500	5
800	6
1260	7

However, in no case was the output power reduced to less than plus 13 dBm.

To compensate for this changing calibration requirement, the stations were required to obtain the S/X-band SNT from the strip chart recorders for each pass. The SNTs were recorded for future reference. When time permitted, the current SNT was used to update the MMR/OLR output power levels for the pass; if time did not permit, the data obtained from the previous pass was used. The station equipment and personnel responded effectively under these changing and varying conditions, and the total data requirement was met by the DSN.

B. Command Capability

Up to the time of the Voyager solar conjunction, there were no quantitative data on command link performance degradation at small SEP angles. As a result, each flight project was forced to adopt a conservative command policy as it approached a solar conjunction. The Voyager Project used the opportunity during the solar conjunction period to collect such data. Command capability demonstration tests were conducted on selected Voyager 1 passes when the SEP angle was 5 degrees or less. The tests consisted of four dummy commands transmitted to Voyager 1 four separate times during the test period. Each series of commands was transmitted at a different uplink power level. The four uplink power levels were obtained by using different levels of transmitter power and modulation suppression of the uplink.

To meet this requirement, the stations were required to perform special calibrations. Additional pretrack preparation time was included in the schedule to support this requirement. The 64-meter stations were required to calibrate their transmitters for 10 kW, 6 kW and 4 kW. 26-meter stations calibrated their transmitters at 18 kW, 12 kW and 8 kW. Range modulation suppression was calibrated at the 64-meter stations for 3 dB, 4 dB and 16 dB, while the calibration at the

26-meter stations was for 3 and 10 dB. All stations verified that command modulation suppression values were calibrated with 3 dB and 0.54 dB.

The tests were successfully supported by the scheduled stations. The activity was highly successful in providing capability data. The results for the period of August 9-29 are contained in Table 1. The levels at which commands were and were not processed is contained in Fig. 1.

C. Other

During the period the stations routinely supported the various spacecraft activities and tests, such as radio frequency subsystem automatic gain control, command detector unit signal-to-noise ratio, antenna and sun sensor calibration, periodic engineering and science calibration, plasma calibration, magnetometer calibration, low energy charged particles, tracking loop capacitor, etc. These efforts all required special preparation and tracking activities by the stations. The resulting support provided by the DSN was excellent.

III. DSN Status

A. DSS 61 – Madrid

On August 9, 1979, the Madrid station was decommitted from project support operations and began an upgrade that will convert the station from a 26- to a 34-meter capability. This upgrade primarily increases the antenna size and included receivers for the reception of X-band signals. The station will return to an operational status on March 9, 1980.

B. DSS 62 – Madrid

The programmed oscillator control assembly was moved from DSS 61 to DSS 62 for the period of upgrade activities so that the capability would be available to uplink Voyager 2. With the loss of the radio frequency tracking loop capacitor in Receiver 2 and complete loss of Receiver 1 (see *Deep Space Network Progress Report 42-49*) it is necessary for the Voyager 2 uplink to be continually tuned to maintain the uplink. This equipment relocation allows a combination of a 26- and 64-m station coverage for both Voyagers during the viewperiod over the Spanish sector.

Table 1. Voyager 1 command capability demonstration test information

Test number	GMT DOY	SEP angle in, deg	First set of 4 commands			Second set of 4 commands			Third set of 4 commands			Fourth set of 4 commands			Total number of commands processed	
			S/C RCVR AGC, dBm	Predicted uplink, dBm	dB above command threshold	S/C RCVR AGC, dBm	Predicted uplink, dBm	dB above command threshold	S/C RCVR AGC, dBm	Predicted uplink, dBm	dB above command threshold	S/C RCVR AGC, dBm	Predicted uplink, dBm	dB above command threshold		
1	221	10	-124	-123	17	-135	-134	6	-137	-136	4	-137	-138	2	16	
2	229	4.4	-121 -129	-123	17	-133 -138	-134	6	-134 -145	-136	4	-137 -142	-138	2	16	Command No. 13 had 1 error corrected by CCS.
3	230	4.2	-122 -126	-123	17	-131 -135	-134	6	-133 -139	-136	4	-135 -141	-138	2	14	CMD 14 and 16 not processed. All lock changes were counted by CCS.
4	232	2.6	a	-123	17	a	-134	6	a	-136	4	a	-136	4	13	Confirmed by CCS hr summary on next day; due to bad D/L data.
5	234	1.4	a	-122	18	a	-125	15	a	-128	12	a	-131	9	15	One of the last 3 commands was not processed.
6	235	1.2	a	-123	17	a	-128	12	a	-132	8	a	-138	2	13	Confirmed next day by CCS hourly summary.
7	236	1.3	a	-123	17	a	-134	6	a	-136	4	a	-138	2	15	Confirmed next day by CCS hourly summary.
8	239	3.0	a	-123	17	a	-134	6	a	-136	4	a	-138	2	13	Confirmed next day by CCS hourly summary.
9	240	3.7	-120 -130	-123	17	-133 -139	-134	6	-131 -147	-136	4	-138 -150	-138	2	14	2 of the last 4 commands were not processed.
10	241	4.4	-122 -130	-123	17	-135 -138	-134	6	-137 -142	-136	4	-139 -140	-138	2	16	CMD 7 and 10 each had 1 error corrected by CCS.

[a]No usable downlink data.

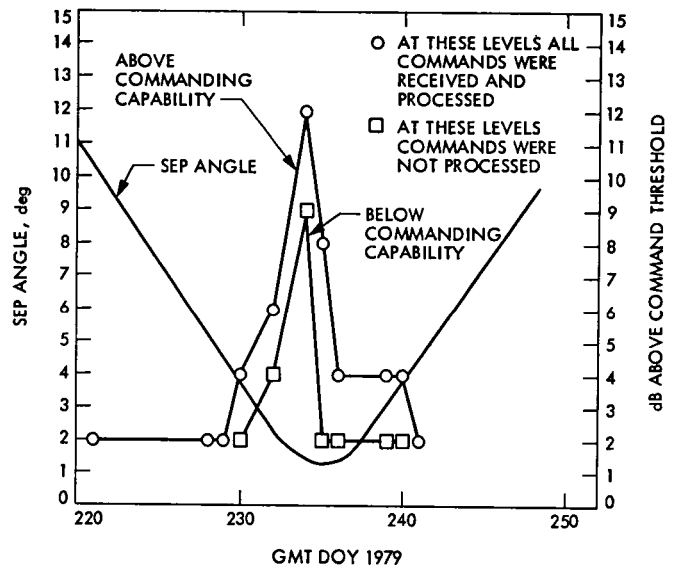

Fig. 1. Command threshold vs SEP angle

Pioneer 11 Saturn Encounter Mission Support

R. B. Miller
TDA Mission Support

Pioneer 11 spacecraft flew by the planet Saturn in August and September 1979. The DSN performance during the support of the first Saturn encounter is described.

I. Introduction

The Pioneer 11 spacecraft was launched on 6 April 1973, and flew by the planet Jupiter with the closest approach on 3 December 1974. After nearly six and one-half years of flight, the Pioneer 11 spacecraft flew within 1.33 Saturn radii of the planet Saturn on 1 September 1979. The trajectory, major mission events, and mission objectives were described in Ref. 1. The overall Deep Space Network (DSN) support plans were also described in Ref. 1 with a more detailed description of operational plans and specific configurations for support of the encounter in Ref. 2.

Although the references should be consulted for more details, the key DSN efforts in support of the Pioneer 11 Saturn encounter are summarized below. The efforts fell in four major areas.

The first major area of DSN support was trying to obtain satisfactory data return at Saturn with a spacecraft designed for a Jovian distance. The activities included the installation of lower noise S-band ruby masers at the overseas stations, and the use of the listen-only mode at the 64-meter diameter antennas while simultaneously transmitting for command purposes from 34-meter diameter stations. At Goldstone an experimental real-time combiner was used to array the large and small antennas. In addition, all telemetry reception stations put in an extensive effort in selecting the "best" of what would ordinarily be considered "identical" equipment in order to eke out every fraction of a dB of improved performance. Telemetry recovery at each station involves a string of equipment from receiver through subcarrier and bit detection to telemetry processing, and the selection process involves testing redundant equipment to select the best performing combination of equipment at a particular station.

The second major area was concerned with taking extra precaution to avoid losing any data during the critical ring plane crossing and periapsis. Besides special procedures, equipment originally installed for the Pioneer-Venus Multiprobe entry was modified and re-implemented as a means of recovering the telemetry data after the fact, without real-time coherent detection, in the event the data were lost in real time. As it turns out, things seem to have gone well enough in real time that it should not be necessary to process any of these data except for a few minutes at enter occultation.

The third major area was to accommodate the very high doppler rates of up to 70 Hz per second that occurred during closest approach. This was accommodated at the 64-meter stations by using the existing programmable local oscillator (PLO) capability of pre-programming rates into the receivers. PLO-controlled receivers were not available at DSS 12, the 34-meter station at Goldstone, and in order to retain that station's receivers in lock as a part of the arraying, PLO control for the receivers were installed on a temporary basis.

There was late identification of an impact on radio science due to the long round-trip light time where extensive amounts of two-way data would not be available. The losses occur at station handovers and, most important, for the critical day of closest approach because of the high doppler rates and the fact that only the 34-meter stations were two-way, and PLO control for the receivers had not been planned and was not available for the Spanish station, DSS 62. When this problem was identified, the personnel at DSS 62 took it upon themselves to put together a team of receiver operators who manually tuned the receivers for several hours of high-rate doppler, spelling each other in a round-robin fashion to relieve fatigue. By this means, DSS 62 was able to provide good two-way doppler for the majority of the pre-closest approach pass, except for a brief time period where the rates were greater than even the manual tuning could accommodate.

The last major area was the need to provide the Project a means of safing the spacecraft and continuing major sequences in the event of the loss of ground communications or the computers at the control center at the Ames Research Center. This involved a potential use of manual real-time commanding well beyond that which the system was originally designed to accommodate. This effort involved special procedures and an extensive amount of testing and training for all station crews to support this contingency commanding activity. In the actual mission, it never became necessary to call on this capability.

II. DSN Performance During Week Leading to Closest Approach

All of the efforts in trying to improve telecommunications performance were aimed at the objective of trying to achieve a 1024-bps data rate for the Saturn encounter. The principal driver for this data rate was the imaging photopolarimeter. This instrument constructs images by a spin-scan method, where for each rotation of the spacecraft the equivalent of one line of the image is taken over a portion of the spin and that line must be read out over the remainder of the spin period before the next line of data is taken. The field of view of the instrument is 28 degrees of roll, and it takes a 1024-bit rate in order to read all of the data back before the buffer is overwritten by the next scan line. If it is necessary to lower the data rate to 512 bps, there are two choices in the imaging mode of the instrument. First is to let the next scan line overwrite the buffer before the previous scan line is completely read out, and this means that only one-half of the scan line would be recovered, which, therefore, results in a picture only 14 degrees high instead of 28 degrees high, but with the same resolution. There is a second possible choice, which is to change the instrument to a lower resolution mode that retains the 28 degrees field of view but with essentially half the resolution. For a more detailed description of this instrument, see Ref. 3.

In the early part of August, based on previous test data and available predictions of the effect the sun would have on the telecommunications link, it was anticipated that 1024 bps would be possible for on the order of three or four hours around zenith in Australia, five or six hours around zenith in Spain. Because of the additional performance added by the arraying, it was anticipated that 1024 bps should be possible for eight hours at Goldstone. In August, early tests of the arraying for the Pioneer case were not successful, and, in fact, over the entire encounter period, a monumental effort was required to get the arraying operating and keep it operating for the encounter. It must be remembered that the real-time combining equipment involved in the arraying is experimental and not operational equipment. Also, the arraying depended heavily on having the proper equipment performance outside of the real-time combiner at both stations. Over the course of the month, the majority of problems found with the arraying were actually outside of the real-time combiner itself. For example, a lot of the early failures at DSS 14 were isolated to poorer performance near threshold of the Block IV Subcarrier Demodulator Assemblies (SDAs) at the specific Pioneer 11 data rate of 1024 bps compared to the Block III SDAs.

The first planned arraying support of the encounter on 25 August, seven days before closest approach, found the arrayed pair of DSSs 12 and 14 performing very well with a gain of 0.4 to 0.5 dB compared to the non-arrayed overseas sites. The listen-only Australian DSS 43 track, which followed on 26 August, had very poor quality data at 1024 bps. The weather was quite bad on this track with occasional heavy rainfall, and the missing performance was attributed to this fact at the time. The Spanish listen-only track went as expected; however, the Goldstone-arrayed track on Sunday, 26 August, showed no apparent gain. The basis for judging the arraying was that one telemetry string would be operated on the output of the real-time combiner at DSS 14, while the redundant telemetry string was operated on the uncombined signal at DSS 14. On this particular day, there was no difference in performance observed between these two strings. An extensive trouble-shooting effort took place at DSSs 12 and 14 between the time of this and the next track with nothing discovered to explain the lack of observed gain. It was felt at the time that the problem may have been in the microwave link between DSSs 12 and 14, but this was never confirmed. For Monday's Australian track, the Project elected to stay at 512 bps because of predicted potential bad weather. The Spanish track continued to have usable 1024 bps, while the following arrayed DSS 12 and 14 track found the arraying to be working perfectly again.

For the next Australian track on 28 August, the Project again elected to stay at 512 bps, and the Spanish track did not attempt any 1024 bps, since the listen-only mode was not used, in order to perform the last precession maneuver until after closest approach. Between tracks Australia was also making special efforts to do testing in order to be assured that they were using the best possible configuration from a performance standpoint. The weather explanation for their poorer performance was not entirely satisfying.

During the arrayed track on 28 August following the precession maneuver, at the scheduled time that the Project had commanded to go to 1024 bps, due to an error the spacecraft stayed in a mode with its feed offset used for conscanning; therefore, the telemetry performance was lower than predicted. This resulted in a round-trip light time of nearly three hours, wherein it was not possible to lock the unarrayed telemetry system at DSS 14 at all. The telemetry data out of the arrayed telemetry string had a very high deletion rate, but was still usable. For this entire time period, it was elected to put both telemetry strings at DSS 14 on the output of the real-time combiner. In other words, if it had not been for the real-time combiner, this three hours of data would have been a total loss. For the following Australian track on 29 August, the Project again elected to remain at 512 bps (Note: times and dates are quoted in GMT, and for the Australian tracks the GMT date is one day later than for PST). The quality of the 1024-bps data at the Spanish station on 29 August was poorer than expected, and the evidence was piling up that something else was going on besides weather problems in Australia. The arrayed 1024-bps data at Goldstone on 29 August was of acceptable quality, although the system noise temperature was registering higher than at previous tracks at DSS 14. On the 30 August Australian track, the Project again elected to stay at 512 bps; however, the signal-to-noise ratio computed by the telemetry system indicated that four hours of 1024 bps would have been possible during that track. During the following Spanish track, the Spaniards reported RFI observed at both the 34-meter and 64-meter stations, but the feeling was developing that what we were really observing was the sun affecting the telecommunications link a full eight days sooner than anticipated and in a more random off-again-on-again fashion in telemetry than in previously observed solar superior conjunctions. Note that on the day of closest approach, the spacecraft was 8 degrees from the sun and closing as observed from the Earth.

The criterion for "good" 1024-bps data was set by the Project as about a 1 percent frame deletion rate. It was discovered in these various bouts of "bad" 1024-bps data from Spain and earlier from Australia that, when the deletion rate got up in the region of 7 percent, the Ames Research Center computer system would go off-line, and no 1024-bps data could be observed at all by Ames in real time. This compounded the problems of trying to assess the telecommunications performance because the key criterion for valid 1024-bps data was the frame deletion rate, and the DSN computation of the frame deletion rate was different from the Ames computation and was not reliable for looking at real-time changes in performance. There were two reasons for the off-lining of the computers at Ames: the additional computer time used in printing alarms when the deletion rate climbed, and the fact that Ames was observing the incoming data as being bursty in time. That is, the data did not flow at a steady rate into the computers, but, rather, there would be a pause and then several frames hit the computer at one time. At first it was thought that this was caused by error correction-detection not being turned off or some other problem in the communications computer at the tracking station, but it turned out to be a natural characteristic of how the convolutional decoder is implemented at the deep space station. In the DSN implementation, when a frame cannot be successfully decoded, the software will give up to four frame times to decode that frame and then the following three frames will be given only a single frame time, so that frames are not lost. When operating on the ragged edge of threshold (or actually below threshold as we were during this encounter), non-regular spacing of the data flow would result. Note that when this problem occurred the data were only lost to Ames in real time and could be played back from the tracking station after the fact.

The fields and particles experimenters at Ames were very concerned about the amount of data that was not seen in real time and the general corruption of their data in trying to achieve high enough data rate to maximize the imaging return. This meant that there was pressure to reduce the "experimentation" with trying to maintain the 1024 bps and to take a more conservative approach.

However, on the next Australian track, based on the measured performance on the previous Australian track and the preceding arrayed track at Goldstone, the Project elected to try for 1024 bps during the time period when the last full planet view was possible before the planet would exceed the field of view of the imaging photopolarimeter. The first 1024-bps data for the Australian track looked very good; however, it was characteristic of the stochastic nature of the effect the sun was having that, by the time of the arrival on the ground of that last full planet picture, the system noise temperature at DSS 43 had climbed several degrees and the deletion rate had grown to well over 10 percent. It was then decided that, for the remainder of the encounter, the overseas sites would remain at 512 bps and that 1024 bps would be used at Goldstone for zenith ±2-1/2 hours. The coup de grace to the 1024 bps at the overseas sites was a brief period of 1024 bps

on 31 August at Spain, which had a frame deletion rate of approximately 8 percent. On the day of closest approach, the 512 bps data were of very good quality, but the computed signal-to-noise ratio indicated that the margin was insufficient for 1024 bps and that the decision to remain at 512 bps had been wise. The 1024 bps at Goldstone with the arraying after closest approach was of good quality and again for the Titan picture on the day after closest approach. The total uncertainties in the look direction to Titan (the combination of trajectory uncertainty and the IPP pointing uncertainty) were sufficiently great that, if the Project had been forced to use 512 bps for the Titan picture, they would probably have elected to have gone to the lower resolution mode of the instrument. This was another time when the arraying really paid off for the mission.

The need to reduce the data rate to 512 bps at the overseas stations was a bit of a disappointment because of the tremendous manpower that was consumed at the overseas sites in trying to maximize their performance. However, if that effort had not been extended, it is quite likely that even the 512 bps would not have been achieved, and, in fact, the Project may have had to have gone to as low a data rate as 128 bps. The net result was a return of something on the order of twenty pictures better than Earth-based resolution instead of the anticipated forty pictures if 1024 bps had been achievable at all stations. However, even with the need to reduce the data rate due to solar noise, the science return was still extensive and more than anyone had anticipated before the encounter. In fact, the Pioneer Saturn Imaging Team stated that they had greater scientific return from the Pioneer 11 Saturn encounter than they had from both the Pioneer 10 and 11 Jupiter encounters. It should be noted that some of the most highly published pictures from the encounter were images received at 512 bps (full resolution, half height) at overseas stations.

One other incident of note during the encounter was degradation of the infrared image of Titan due to interference from a Soviet satellite. There had been previous communications enlisting cooperation from the Soviets with regard to two satellites which were potential interference threats, and a third satellite in this family was launched the Wednesday before closest approach. Russian cooperation was enlisted for the day of closest approach and the day after closest approach during the Titan visual imaging; however, for a variety of reasons Russian cooperation was not specifically requested for the time period of receipt of the infrared image of Titan, which occurred two days after closest approach. The Spanish station experienced interference of varing degrees of severity for several hours two days after closest approach. For an approximately 40-minute time period, no telemetry data could be recovered at all, and this encompassed the original estimate of when the Titan picture would be received on the ground. Subsequent analysis revealed that the Titan image was really 20 minutes later than first expected; however, the unintentional interference from the Soviet satellite resulted in a loss of on the order of 14 percent of the raw telemetry data which, according to the experimenter, resulted in only about 50 percent of the infrared data being usable because of the way in which the infrared data are commutated in the spacecraft telemetry.

III. Summary

Despite the sun's degradation of the telecommunications link performance, the efforts of the Deep Space Network resulted in a greater data return than thought possible just one year before encounter. Many new discoveries were made, and the science return was greater than anyone could have hoped, especially when it is remembered that an encounter of Saturn was not in the original design or definition of the Pioneer 10 and 11 missions.

References

1. Miller, R. B., "Pioneer 11 Saturn Encounter Mission Support," *Deep Space Network Progress Report 42-52*, pp. 4-7, Jet Propulsion Laboratory, Pasadena, Calif., Aug. 15, 1979.

2. Rockwell, G. M., "Pioneer 11 Saturn Encounter Support," *Deep Space Network Progress Report 42-53*, pp. 10-20, Jet Propulsion Laboratory, Pasadena, Calif., Oct. 15, 1979.

3. Miller, R. B., "Pioneer 10 and 11 Mission Support," *Deep Space Network Progress Report*, Technical Report 32-1526, Volume 16, pp. 15-21, Jet Propulsion Laboratory, Pasadena, Calif., Aug., 15, 1973.

Stability of the Multimegabit Telemetry Carrier Loop

D. W. Brown
TDA Technology Development

Basic sampled data loop stability is reviewed; the effect of an additional low-pass filter in the loop is analyzed. Resulting upper bounds on permissible loop bandwidth are established.

I. Introduction

The carrier tracking loop of the multimegabit telemetry demodulator currently under advanced systems development is of the second order sampled data type. In addition to the design point damping considerations typical of a continuous or analog loop, an additional potential instability exists for excessive gain (Ref. 1). Over and above that limitation, this intended implementation is confronted with the effects of a 10-kHz roll-off in the response of the Block IV VCO when operating in the long loop carrier reconstruction mode (Fig. 1 of Ref. 2). We will start with a simplified model (Fig. 2 of Ref. 1), add a low-pass time constant to the open loop transfer function, generalize the parameters, and develop a design guideline for this application.

II. The Model

Proceeding directly from Fig. 1, we can write the open loop transfer function in the variable z, where $z = e^{Ts}$:

$$OL(z) = \frac{\phi_o(z)}{\phi(z)} = AK_vF(z) \times Z\left\{\frac{1 - e^{-Ts}}{(1 + T_x s)s^2}\right\}$$

where $Z\{\ \}$ denotes the z-transform equivalent to the bracketed Laplace transform. This yields

$$OL(z) = AK_vF(z)\left[\frac{Tz^{-1}}{1 - z^{-1}} - \frac{T_x(1 - e^{-T/T_x})z^{-1}}{1 - e^{-T/T_x}z^{-1}}\right]$$

For shorthand, let $\tau = T_x(1 - e^{-T/T_x})$:

$$OL(z) = AK_v\left(K_L + \frac{K_I}{1 - z^{-1}}\right)\left(\frac{Tz^{-1}}{1 - z^{-1}} - \frac{\tau z^{-1}}{1 - e^{-T/T_x}z^{-1}}\right) \quad (1)$$

III. The Continuous Equivalent

In order to generalize the parameters into more familiar terms, let us digress temporarily by applying the approximation

$$1 - z^{-1} = 1 - e^{-Ts} \approx Ts$$

for sampling rate $1/T$ large compared with frequencies of interest. Similarly,

$$z^{-1} \approx 1$$

For brevity we write the sample interval as simply T; other multimegabit authors have used T_m or mT.

Then, for an ideal loop ($T_x = 0$), the open loop function reduces to

$$OL(s) \approx \frac{AK_v}{s}\left(K_L + \frac{K_I}{Ts}\right)$$

And the closed loop transfer function is

$$H(s) \approx \frac{\frac{AK_v}{s}\left(K_L + \frac{K_I}{Ts}\right)}{1 + \frac{AK_v}{s}\left(K_L + \frac{K_I}{Ts}\right)}$$

If we set

$$T_2 = T(K_L/K_I), \tag{2}$$

$$H(s) \approx \frac{1 + T_2 s}{1 + T_2 s + \frac{T}{AK_v K_I}s^2}$$

which is readily recognized as the continuous second-order loop, where

$$\omega_n^2 = \frac{AK_v K_I}{T} \text{ and } \zeta = \frac{\omega_n T_2}{2} \tag{3}$$

Hence

$$H(s) \approx \frac{1 + \frac{2\zeta}{\omega_n}s}{1 + \frac{2\zeta}{\omega_n}s + \frac{1}{\omega_n^2}s^2} \tag{4}$$

Provided the above approximation is maintained in design (expressed sometimes as $2\beta_L T << 1$), the continuous approximation and equivalences are useful in many aspects of performance analysis. But for the purposes of this study, it is preferred to retain the exact z-transform approach.

Before returning to the exact form, it should be noted that loop gain variations in A will occur due to AGC and limiter effects in the range of 10:1. Since

$$\frac{\zeta_{max}^2}{\zeta_0^2} = \frac{A_{max}}{A_0} \tag{5}$$

where subscript "0" denotes design point, and assuming $\zeta_0^2 = 1/2$,

$$\zeta_{max}^2 \approx 5$$

To allow for implementation tolerances, the following analysis will consider

$$\frac{1}{4} \leqslant \zeta^2 \leqslant 8 \tag{6}$$

IV. Stability Analysis

Returning now to the sampled data transfer function (1) and substituting equivalences (2) and (3), we obtain

$$OL(z) = \frac{4\zeta^2}{T_2^2}\left(\frac{T + T_2 - T_2 z^{-1}}{1 - z^{-1}}\right)\left(\frac{Tz^{-1}}{1 - z^{-1}} - \frac{Tz^{-1}}{1 - e^{-T/T_x}z^{-1}}\right) \tag{7}$$

Rearranging as a ratio of polynomials in z^{-1},

$$OL(z) = \frac{(T+T_2)(T-\tau)z^{-1} - \left[(T+T_2)(Te^{-T/T_x}-\tau)+T_2(T-\tau)\right]z^{-2} + T_2(Te^{-T/T_x}-\tau)z^{-3}}{\frac{T_2^2}{4\zeta^2}\left[1-(2+e^{-T/T_x})z^{-1}+(1+2e^{-T/T_x})z^{-2}-e^{-T/T_x}z^{-3}\right]}$$

From

$$H(z) = \frac{OL(z)}{1+OL(z)} = \frac{\text{NUM } OL(z)}{\text{DENOM } OL(z) + \text{NUM } OL(z)},$$

$$H(z) = \frac{(T+T_2)(T-\tau)z^{-1} - \left[(T+T_2)(Te^{-T/T_x}-\tau)+T_2(T-\tau)\right]z^{-2} + T_2(Te^{-T/T_x}-\tau)z^{-3}}{\frac{T_2^2}{4\zeta^2} + \left[\begin{matrix}(T+T_2)(T-\tau)\\ -\frac{T_2^2}{4\zeta^2}(2+e^{-T/T_x})\end{matrix}\right]z^{-1} - \left[\begin{matrix}(T+T_2)(Te^{-T/T_x}-\tau)+T_2(T-\tau)\\ -\frac{T_2^2}{4\zeta^2}(1+2e^{-T/T_x})\end{matrix}\right]z^{-2} + \left[\begin{matrix}T_2(Te^{-T/T_x}-\tau)\\ -\frac{T_2^2}{4\zeta^2}e^{-T/T_x}\end{matrix}\right]z^{-3}} \tag{8}$$

where $\tau = T_x(1 - e^{-T/T_x})$, as previously defined.

As a partial check on results, set $\tau = T_x = 0$ for the ideal case:

$$H(z) = \frac{(T+T_2)Tz^{-1} - TT_2z^{-2}}{\left[\frac{T_2^2}{4\zeta^2}\right] - \left[2\frac{T_2^2}{4\zeta^2} - (T+T_2)T\right]z^{-1} + \left[\frac{T_2^2}{4\zeta^2} - TT_2\right]z^{-2}} \tag{9}$$

It turns out that the principal stability criterion employed in Ref. 1 is equivalent to requiring that the sum of the bracketed coefficients in the denominator exceed zero, or

$$\left(\frac{T}{2}+T_2\right)T < 2\frac{T_2^2}{4\zeta^2}$$

And that the gain margin may be computed as the ratio by which it does, such that

$$GM = \frac{2\frac{T_2^2}{4\zeta^2}}{\left(\frac{T}{2}+T_2\right)T} = \frac{1}{2\zeta^2}\frac{T_2}{T}\frac{1}{\left(1+\frac{T}{2T_2}\right)} \tag{10}$$

But since $T/T_2 = K_I/K_L$, by equation (2), and K_I/K_L is to be implemented on the order of 2^{-8} (another manifestation of the $2\beta_L T \ll 1$ criterion),

$$GM \approx \frac{1}{2\zeta^2}\frac{K_L}{K_I} = \frac{2^7}{\zeta^2}$$

yielding:

$$GM\left(\zeta^2 = \frac{1}{2}\right) = 2^8 = 256 \text{ or } 48 \text{ dB at design point}$$

and

$$GM(\zeta^2 = 8) = 2^4 = 16 \text{ or } 24 \text{ dB at maximum gain}$$

Holmes' result of 35.2 dB was probably based on a $\zeta^2 = 1/4$ design point and $A_{max}/A_0 \approx 8.9$, yielding $\zeta^2_{max} \approx 2.225$ and $GM = 2^7/2.225 \approx 57.5$ or 35.2 dB.

While it is necessary to design with an adequate gain margin, it is also required in the "real world" of equation (1) to maintain the "extra" time constant T_x smaller than the reciprocal frequencies of interest. This situation can be loosely related as

$$\frac{1}{\omega_n} > T_x > T \tag{11}$$

A rule of thumb is recalled from continuous loop design:

$$\omega_n T_x < 0.05 \qquad (12)$$

But this is too empirical; we need to calibrate the effect of T_x on loop margins or transient performance in order to specify the design relationships with more rigor. And although it might be possible to apply numerical stability criteria to equation (8) as we did above for the ideal case, the approach taken is to perform the inversion of the z-transform pulse response function into the time domain and parametrically evaluate the overshoot of the response to a step input. And, rather than attempt a formal inversion, an alternate technique is employed (Ref. 3, p. 57). If the desired pulse response function is expanded into a power series in z^{-n} by the process of long division, then the coefficients represent the magnitudes of the time response at times $t = nT$. The mechanics are handled as follows:

(1) For each parametric set of variables, T, T_2 T_x, and ζ^2, compute the coefficients for equation (8).

(2) Multiply $H(z)$ by $\phi_i(z) = 1/(1 - z^{-1})$ to obtain $\phi_o(z)$ for a step input and regroup the denominator in z^{-n} series.

(3) Enter the coefficients of $\phi_o(z)$ numerator and denominator in a desk calculator programmed to compute the first 38 coefficients of the power series.

(4) Plot these coefficients versus $t = nT$ to obtain a sampled version of $\phi_o(t)$.

Returning to the problem at hand, it is likely that for a given sample rate T, all parameters of Fig. 1 would remain fixed with the exception of A, which will vary with input signal SNR as noted above. Intuitively, then, a given constraining value of T_x is most likely to have the greatest impact for the widest bandwidth, i.e., strong signal. Take, then, as a starting point $\zeta^2 = 8$. Arbitrarily, set $T_2 = 16$ as a convenient scaling within the $38T$-second window offered by the calculator program.

As an initial value for T_x use (12):

$$\omega_n T_x = 2\zeta \frac{T_x}{T_2} < 0.05$$

or

$$T_x < 0.025 \frac{T_2}{\zeta} = \frac{\sqrt{2}}{10} \approx \frac{1}{8}$$

What, then, in our scale model loop, should we use for T? A true scaling would set

$$T = T_2 \frac{K_I}{K_L} = 16 \times 2^{-8} = \frac{1}{16}$$

This would provide us only with $t = nT = 38/16$-second visibility due to the limited range of the program. Let us reduce the gain margin of our scale model slightly and let $T = 1/10$, providing $t = 38/10 \approx 4$ seconds.

Taking, now, as a baseline $T_2 = 16$, $\zeta^2 = 8$, $T = 1/10$, and $T_x = 0$, we obtain

$$\phi_o(z) = \frac{1.61z^{-1} - 1.60z^{-2}}{8 - 22.39z^{-1} + 20.79z^{-2} - 6.40z^{-3}}$$

and for $T_x = 1/8$,

$$\phi_o(z) = \frac{0.5018z^{-1} - 11.39z^{-2} - 0.3824z^{-3}}{8 - 27.0926z^{-1} + 34.1683z^{-2} - 19.0525z^{-3} + 3.9768z^{-4}}$$

The resulting time series are plotted in Fig. 2. We note that the "rule of thumb" value of $\omega_n T_x$ results in a discernable, but inconsequential, change in transient response. Recalling that the overshoot of the ideal loop with $\zeta^2 = 1/2$ design point damping is approximately 20 percent, let us keep increasing T_x parametrically until some arbitrary upper bound is reached. A value of 40 percent is taken as a likely upper limit of desirable response. Values of $T_x = 1/4, 1/2, 1$ are seen in Fig. 2 to cover this range.

In order to evaluate the sensitivity of the arbitrary reduction in gain margin for this scale model, we can plot peak overshoot (evaluated as above) versus T.

From Fig. 3 we can conclude that for $T = 1/10$ or even $1/8$, the model closely approximates the actual design at a gain margin of 24 dB.*

*Strictly speaking, gain margin as defined in (10) is not applicable in the presence of T_x; however, it remains a useful, well-defined characteristic.

Now that a tentative worse case $T_x/T_2 = 1/16$ has been established, it would be useful to vary ζ^2 as a parameter, thus validating $\zeta^2 = 8$ as the maximum overshoot condition. Figure 4 presents the full range of ζ^2 in octave steps for both $T_x/T_2 = 1/16$ and $T_x = 0$. In order to fit the region of interest in $t = nT$ as ζ^2 is varied, several different values of T were employed, always keeping the modelled gain margin of 18 dB or better (see Fig. 3), thus maintaining reasonable accuracy.

V. Conclusions

We have seen that the multimegabit sampled data loop may be closely approximated as a continuous loop and that the gain margin may be readily computed as

$$GM = \frac{1}{2\zeta^2}\frac{T_2}{T} = \frac{1}{2\zeta^2}\frac{K_L}{K_I}$$

whatever the detailed design may be. Additionally, Figs. 2 and 4 offer a basis for specifying maximum tolerable extra time constant or, conversely, the maximum tolerable nominal bandwidth for a given T_x.

For example, from the figures, one could specify that for $8 \geqslant \zeta^2 \geqslant 1/2$, and overshoot comparable to the ideal at $\zeta^2 = 1/2$:

$$\frac{T_x}{T_2} \leqslant \frac{1}{32} \quad \text{or} \quad T_x \leqslant \frac{T}{32}\frac{K_L}{K_I}$$

or

$$2\beta_{L_0} T_x \leqslant \frac{3}{64} \text{ at } \zeta_0^2 = \frac{1}{2}$$

Alternatively, for $8 \geqslant \zeta^2 \geqslant 1/4$, and overshoot less than 40 percent,

$$\frac{T_x}{T_2} \leqslant \frac{1}{16}$$

for a $2\beta_{L_0} T_x$ product $\leqslant 3/32$ at $\zeta_0^2 = 1/2$. In any case, this approach offers a relatively exact analysis and perspective on the compound effects of gain margin and extra time constant.

References

1. Holmes, J. K., "Stability Analysis of the Multimegabit Telemetry Demodulator/ Detector Design," *DSN Progress Report 42-51*, pp. 31-38, Jet Propulsion Laboratory, Pasadena, Calif., June 15, 1979.
2. Woo, K. T., "Effects of Asymmetric Passband Filtering on the Phase of the Costas Loop's Reconstructed Carrier," *DSN Progress Report 42-51*, pp. 105-112, Jet Propulsion Laboratory, Pasadena, Calif., June 15, 1979.
3. Ragazzini, J. R., and Franklin, G. F., "Sampled-Data Control Systems," McGraw-Hill, New York, 1958.

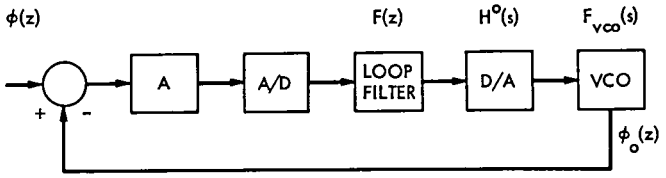

$$F(z) = K_L + \frac{K_I}{1-z^{-1}}$$ DIGITAL FILTER

$$H^\circ(s) = \frac{1-e^{-Ts}}{s}$$ ZERO-ORDER SAMPLE AND HOLD

$$F_{vco}(s) = \frac{K_v}{(1+T_x s)s}$$ VCO WITH INPUT ROLL-OFF

Fig. 1. Simplified loop model with VCO roll-off

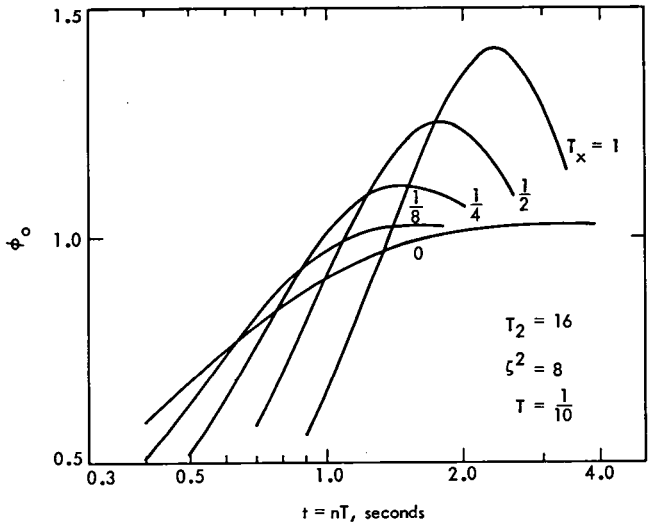

Fig. 2. Transient response vs extra time constant

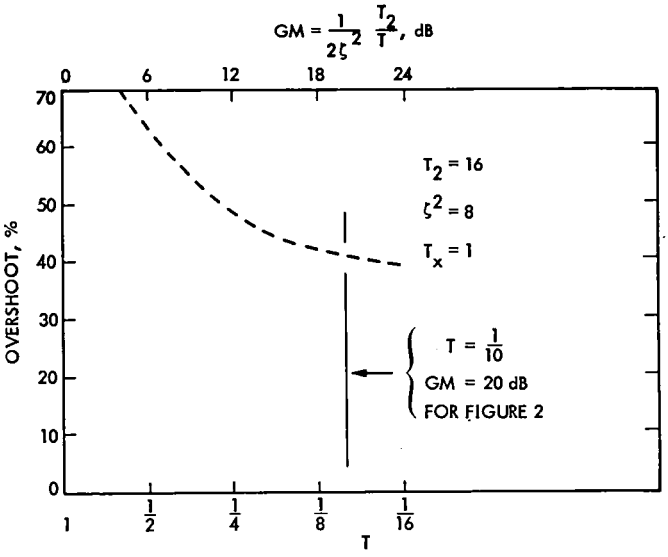

Fig. 3. Sensitivity of overshoot to gain margin

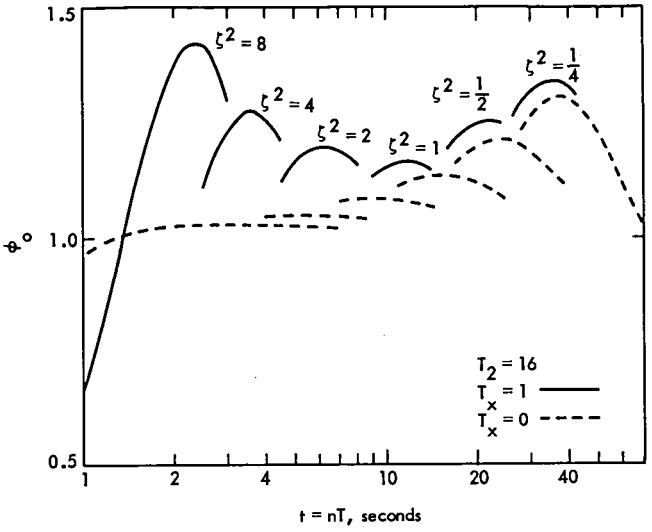

Fig. 4. Transient response vs damping

An Examination of Ancillary Equipment for a Proposed 34.3 GHz High Power Gyrotron TWT Amplifier

A. Kupiszewski
Radio Frequency and Microwave Subsystems Section

A short review of gyrotron developments and applications is given with attention to both theory and experiments. Parameters for a point design for a gyrotron TWT amplifier described in a previous article are listed again, and a detailed examination of ancillary equipment is made with emphasis on the availability of high voltage and handling facilities at Goldstone. A safety-interlock tree for insuring longer tube life under operating conditions is proposed, and a sequence for turn on/off of the proposed tube is given. In addition, reasoning for the expectation of multimode output is presented.

I. Introduction

Cyclotron Resonance Masers or gyrotrons are microwave amplifier tubes which show great promise for becoming the final amplifier stage for planetary radar transmitters and millimeter wave spacecraft uplinks. Impetus for their development is provided by current crowding at S-and X-band frequencies, the greater radar ranging and resolution available at higher frequencies with a given aperture antenna, particle accelerator technology augmentation, and fusion plasma heating applications. While high power (>10 kW CW) klystrons, twystrons, and TWTs perform excellently in the 1 to 18 GHz range, these conventional microwave tubes cannot be scaled to the 28 to 235 GHz range and maintain their high efficiency, high power parameters because of heat transfer problems in the relatively small electron interaction volume. Gyrotrons, on the other hand, can utilize overmoded cavities or waveguides and minimize the aforementioned, traditional high frequency scaling problems. In fact, the usual $P \propto 1/f^2$ (Ref. 1) scaling condition can be ignored and experimental research in the field has produced some exciting millimeter wave results: for example, 22 kW at $\lambda = 2$ mm and 1.5 kW at $\lambda = 0.92$ mm (Ref. 2), 10 kW at 8.9 mm (Ref. 3), and a pulsed oscillator which is 37 percent efficient at 28 GHz with a power output of 250 kW (Ref. 4).

The interaction mechanism responsible for microwave amplification in gyrotrons is azimuthal phase bunching due to the dependence of the electron cyclotron frequency on the relativistic electron mass. A hollow beam formed by a magnetron-injection gun (Ref. 5) is guided by a strong dc magnetic field into a cavity or waveguide close to cutoff and magnetic coupling to the RF fields therein produces amplification. It is the spinning or gyrating electron motion (Larmor orbital motion) caused by the guiding magnetic field from which the gyrotron derives its name. Like conventional tubes utilizing longitudinal electron bunching mechanisms, gyrotrons, which operate by azimuthal-phase bunching, can be divided into categories dependent upon the cavity or waveguide configurations used, for example, gyroklystrons which use cavities or gyroTWTs which use waveguides in the interaction volume. The mathematical analysis for the former is based upon solving the power emission integral while utilizing a

relativistic correction to the cyclotron frequency and substituting for the perturbed electron distribution function via Vlasov theory arguments (Refs. 6, 7); the mathematical analysis for the latter is based upon solving for the dispersion relationship obtained from the determinant of the coupled electro-magnetic field wave equation matrix, after appropriate substitution for the electron and current densities via Vlasov theory arguments (Refs. 8, 9, 10).

In a previous article (Ref. 8), a point design for a gyrotron traveling wave tube amplifier was presented and ancillary equipment features (magnetic field, beam voltage and current, power dissipated in the collector, etc.) were listed. Since none of the power supply specifications exceeded the ratings of units already available at DSS 13 at Goldstone, it was proposed that, should a prototype be built by JPL or for JPL by a contractor, high power testing could be carried out and integration difficulties with existing systems examined at the test bed site without recourse to completely new support technology development or major high voltage equipment purchase. It was therefore suggested that a more detailed examination of required support apparatus be made with an eye to equipment protection systems and overall safety procedures. The following sections address not only these questions, as related to the previously presented point design, but also the output mode structure to be expected.

II. Support Equipment

The gyroTWT point design previously presented had the following important calculated characteristics: an output frequency of 34.3 GHz, a wave power of 354.36 kW CW, a beam voltage of 70.80 kV, a beam current of 9.50 A, a magnetic field strength of 13.07 kG, an interaction length of 34.90 cm for a total gain of 40 dB, a -3 dB bandwidth of 384 MHz, a drive power requirement of 35.44 W, and an electronic conversion efficiency in the lab frame of 52.7 percent. At DSS 13 (Venus Station), there is a 1 MW CW power supply capable of delivering the required amount of voltage to the magnetron-injection gun. This latter structure is composed of a thermionic emitting surface, a control electrode, and an anode. The relative potential differences are 30 kV between cathode and control electrode and 70 kV between cathode and anode (Refs. 5, 11). Beam current is controlled by the cathode temperature and, consequently, by the heater current. The heater supply should be a 100 W unit with low voltage, high current output. For purposes of cathode cooling and voltage holdoff, the cathode assembly (including some of the focusing magnets) should be immersed in an oil bucket with a small submersible pump for oil circulation.

General cooling requirements for body and collector will be similar to that of the 400 kW CW S-band klystrons presently used. The collector will have to dissipate 354 kW and either a depressed collector design or PPM defocusing using either Samarium Cobalt or perhaps bulkier, but less expensive materials, may be required. Local space charge effects can accelerate the "spent" hollow electron beam (Ref. 8) to about 140 keV. Impact of such energetic electrons on the copper collector surface results in X-ray generation beyond the safe-level attenuation capabilities of the collector tube. Hence, a lead shield about 0.3175 cm (1/8 in.) thick must surround the device.

As with other high power tubes, the interaction volume and the cathode region must be under fairly high vacuum (better than 1.333×10^{-4} N/m^2 (10^{-6} torr)). This is a condition imposed by the Vlasov theory which does not include a collision term in the "continuity" equation satisfied by the electron distribution function (Ref. 12). Also, the high vacuum inhibits breakdown or arcing between cathode and anode. At present, it is thought that Vac-ion® pumps are sufficient to obtain the desired vacuum. These units also have the added advantage of being useful as vacuum integrity diagnostics. Should vacuum integrity be lost, for any reason, the tube would have to be immediately shut down to prevent cathode surface poisoning.

Yet another area of crucial interest is the guiding magnet. This device is a solenoid which surrounds the interaction volume and keeps the electron beam focused in the tube length before the collector. A control of better than 1 percent over the magnet current must be exercised to maintain high efficiency (Refs. 8,9) and, typically, a range of 600-700 A at 30-60 V would be required to maintain the 13.07 kG field if a water-cooled copper solenoid were to be used. In addition, the magnet can be utilized as a "leaky" mirror to transfer longitudinal streaming energy into perpendicular Larmor orbital motion, thereby increasing the total energy available for conversion to microwaves. Hence, design constraints on the magnetron-injection gun, which would otherwise have to provide the required energy distribution from the start, would be eased.

At present, there is some debate whether the solenoid should be a conventional magnet composed of copper conductor with a hollow water channel for cooling or a superconducting magnet composed of Nb_3Sn embedded in a copper matrix. Since power dissipation will be the important parameter, if the superconducting solenoid does not give a factor of 1000 to 1 lower power dissipation than that achievable at room temperature, its advantage over a conventional copper magnet is doubtful. Another factor to be considered is that, for every watt of heat transfer in the

cooled superconducting structure about 400 watts of power must be supplied at the refrigeration system input (Ref. 13).

The overall weight and dimensions of the gyroTWT are difficult to estimate without some experimentation. Considering magnets, cooling assemblies, lead shielding, and collector tube, the weight would probably not exceed 680.39 kg (1500 lb). This can be compared to the Varian tentative specification for the VGA-8000, a 28 GHz, 200 kW CW cyclotron resonance interaction oscillator. The latter's dimensions are 254 cm (100 in.) in length, 106.68 cm (42 in.) maximum diameter, and a total weight of 498.95 kg (1100 lb) (Ref. 11). The cranes and other weight handling fixtures at Goldstone should be sufficient for moving and positioning a tube of that size.

III. Special Considerations

To minimize power loss due to reflection at the output window (which is on beam axis), careful consideration must be given to the VSWR at that ceramic surface. Ideally, a VSWR of 1.1:1 or 1.2:1 should be used. Not only is this parameter important to power output, but the backwards wave amplification should be inhibited as much as possible so that additional backwards heating at the cathode assembly and at the drive window(s) does not occur. The extra cathode heating could be crucial in terms of beam current control since this latter is proportional to emitting surface temperature. It would not be desirable to attempt control of the beam current by increasing or decreasing the heater current and then discover that the cathode temperature remained essentially constant due to backwards heating as a result of a poor VSWR at the output window. Cathode cooling might then also become a problem. A reflected power monitor would be a useful device for measuring the VSWR.

Another difficulty commonly encountered in high power transmitter tubes is destructive arcing. The output waveguide, which leads to filters and the output horn antenna, is usually filled with nitrogen at one atmosphere pressure. Due to the high microwave power levels involved, arcing in this output waveguide can occur. Once the arc is formed, it generally propagates backwards toward the generator and hangs at the output window. Thermal gradients across the window lead to its shattering and the tube fails catastrophically (Ref. 14). Such failure results in cathode poisoning and other damage. The tube is then generally considered unsalvageable. However, a protection scheme using fiber optics and photodiodes to sense the propagating arc can be employed to shutdown the tube by taking the accelerating voltage off line. Signals from the optoelectronics trigger an SCR-controlled pulse forming network which turns on a Hg-plasma ignitron tube, thus shorting the accelerating potential. "Crowbar" systems of this type presently in use respond in less than 45 microseconds and terminate tube operation. Hence, the propagating arc never reaches the output window. It is clear that such a protection system will have to be employed in conjunction with other safety-interlocks in the 34.3 GHz gyroTWT system because of the high power output levels.

In fact, an entire safety-interlock tree (see Fig. 1) must be designed so that tube operation can be scrammed at the least sign of trouble. Overvoltage, undervoltage, magnet current, magnet coolant flow, oil flow, body and collector coolant flow, body current, collector current, forward and reverse power, water load temperature, arc detection, and drive power sensors must all be included so that failure of any one item will cause shutdown.

It is necessary to have a great deal of control over most of the above listed parameters, and deviation can potentially cause not only poor tube operation and unacceptable output results but also extensive failure leading to extremely costly repairs or actual scrapping of the tube. For example, the magnetic field strength is a highly important feature which must be strictly controlled to insure high power output and high efficiency (Refs. 8,9). Wandering of the magnet current cannot be tolerated since, not only will the previously mentioned two factors suffer greatly, but the electron beam itself may impact or graze a tube surface, causing local heating and/or melting. (Both effects of power loss and local heating have been observed by the author in a low power S-band gyromonotron experiment at the California Institute of Technology.) As backup features to a magnet current sensor, body and collector overcurrent sensors are required. Similarly, a loss of coolant or an interruption in its flow is insupportable because of physical damage to the tube resulting from overheating. Coolant flow sensors on both tube and magnet are required for that reason. Drive power monitors are also essential so that potential spot melting in the collector does not occur due to lack of beam modulation, which aids in electron spreading effects. This latter is a requirement for most conventional highpower microwave tubes. Forward and reverse power sensing is important for arc detection as well as monitoring of backwards cathode heating (Ref. 14). The reverse power detection, coupled with the light sensing diodes, makes it fairly certain that as soon as an arc is formed, it is detected either by direct visual confirmation or by a rapid rise in reflected power. By the same token, a power supply runaway condition resulting in overvoltage cannot be permitted because of potential cathode-anode arcing leading to destruction of the emitting surface. For these reasons, an interlock tree with all of these links is essential to insuring safe system operation and system longevity.

Some apparent redundancy is necessary to failsafe scramming if any one particular branch of the safety-interlock tree were to become non-functional during normal operation. In fact, the entire amplifier system (see Fig. 2) is highly interdependent and the nature of the interlock suggests a turn on/turn off procedure (see Fig. 3) that is similar to that used for other high power microwave tubes.

IV. Collector Output Mode Structure

The collector tube, through which the output power is emitted, must be radially larger than the interaction waveguide for reasons of high current intercept and greater heat dissipation (Ref. 8). Power densities due to the impacting electron beam may be on the order of 0.62 kW/cm^2 (4 kW/in.^{2}) which, by comparison, is considered a desirable level for the X-3075, a 500 kW CW S-band amplifier (Ref. 15). The high power millimeter wave output also mandates a waveguide radially larger than the interaction volume, so that breakdown or arcing is inhibited if not eliminated. However, use of the larger collector results in multimode output due to the lower cutoff frequencies of the principal modes of energy propagation. Circular polarization of the output is to be expected due to the cyclotron motion of the hollow electron beam and polarity will be dependent on the direction of the guiding magnetic field.

Experimental determination of the percentage of energy in a particular mode will be required. For purposes of comparison, the Varian VGA-8000 28 GHz 200 kW CW oscillator radiates its output in a 6.35 cm (2.5 in.) ID pipe principally in the TE_{01}, TE_{02}, TE_{03} modes (Ref. 11), but an examination of cutoff frequencies shows that energy will propagate in many other modes as well. Hence, measurable amounts of energy will be transmitted in modes other than the three already mentioned, and proper phasing and/or filtering in the antenna section will be required to achieve a particular signal for final ex-atmosphere transmission.

V. Conclusion

Most of the support equipment required for highpower microwave tubes is directly applicable to gyrotron devices. Differences between gyrotrons and conventional klystrons are generally internal, for example, the guiding magnetic field is of a higher order of magnitude, the output power can be taken directly off the beam axis, and a hollow beam from a magnetron injection gun is used to increase efficiency. Should a prototype tube at 34.3 GHz be built, testing at Goldstone appears to be feasible, since the main power supplies and handling facilities would be adequate for dealing with the demands of the gyrotron tube. Standard safety procedures could be used and the only development required appears to be perfection of techniques for accurately measuring multimode highpower output at Ka-band frequencies.

References

1. King, D. D. P., "Millimeter-Wave Prospectus," *Microwave Journal*, Vol. 10, November 1967, p. 24.

2. Flyagin, V. A., Gaponov, A. V., Petelin, M. I., and Yulpatov, V. K., "The Gyrotron," *IEEE Trans. Microwave Theor. Technol.*, No. 6, June 1977, p. 514.

3. Kisel', Korablev, Navel'Yev, Petelin, and Tsimring, "An Experimental Study of a Gyrotron Operating at the Second Harmonic of the Cyclotron Frequency, With Optimized Distribution of the High-Frequency Field," *Radio Engineering Electron. Phys.*, Vol. 19, April 1974, p. 95.

4. Jory, H., Hegji, S., Shively, J., and Symons, R., "Gyrotron Developments," *Microwave Journal*, Vol. 21, August 1978, p. 30.

5. Chu, K. R., Drobot, A. T., and Seftor, J. L., "An Investigation of a Magnetron-Injection Gun Suitable for Use in Cyclotron Resonance Masers," Naval Res. Lab Memo Report No. 3697.

6. A. Kupiszewski, "The Gyrotron--A High Frequency Microwave Amplifier," *The Deep Space Network Progress Report 42-52*, August 15, 1979, p. 8.

7. Hirshfield, Bernstein, & Wachtel, "Cyclotron Resonance Interaction of Microwaves with Energetic Electrons," *IEEE Journal QE-1*, September 1965, p. 237.

8. A. Kupiszewski, "A Point Design for a Gyrotron Traveling Wave Tube Amplifier," *The Deep Space Network Progress Report PR 42-53*, October 15, 1979, p. 33.

9. Chu, K. R., Drobot, A. T., Granatstein, V. L., and Seftor, J. L., "Characteristics and Optimum Operating Parameters of a Gyrotron Traveling Wave Amplifier," IEEE Trans. *Microwave Theor. Technol.*, February 1979, p. 178.

10. Ott, E., and Manheimer, W. M., "Theory of Microwave Emission by Velocity-Space Instabilities of an Intense Relativistic Electron Beam," *IEEE Trans. PS-3*, 1975, p.1.

11. Berry, "Tentative Specification Type VGA-8000 Cyclotron Maser," July 30, 1979, private communication.

12. Krall & Trivelpiece, *Principles of Plasma Physics*, McGraw-Hill, 1973, pp. 78-82.

13. Cohen, M. H., *Superconductivity in Science and Technology*, Univ. of Chicago Press, 1968, p. 103.

14. Yen, H. C., "A Preliminary Model for High-Power Waveguide Arcing and Arc Protection," *The Deep Space Network Progress Report 42-48*, December 15, 1978, p. 118.

15. Goldfinger, A., *Study Program for Design Improvements of the X-3060 and X-3075, Phase I: Study Definition, Final Report*, JPL Contract No. 954782, Varian Associates, Inc., Palo Alto, California, January 1978, pp. 24-25.

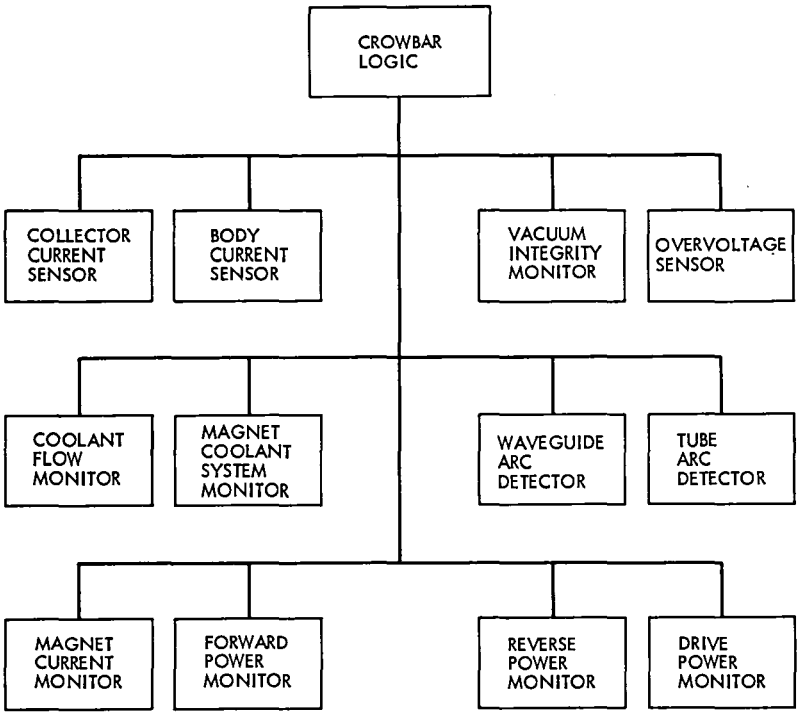

Fig. 1. Safety-interlock tree

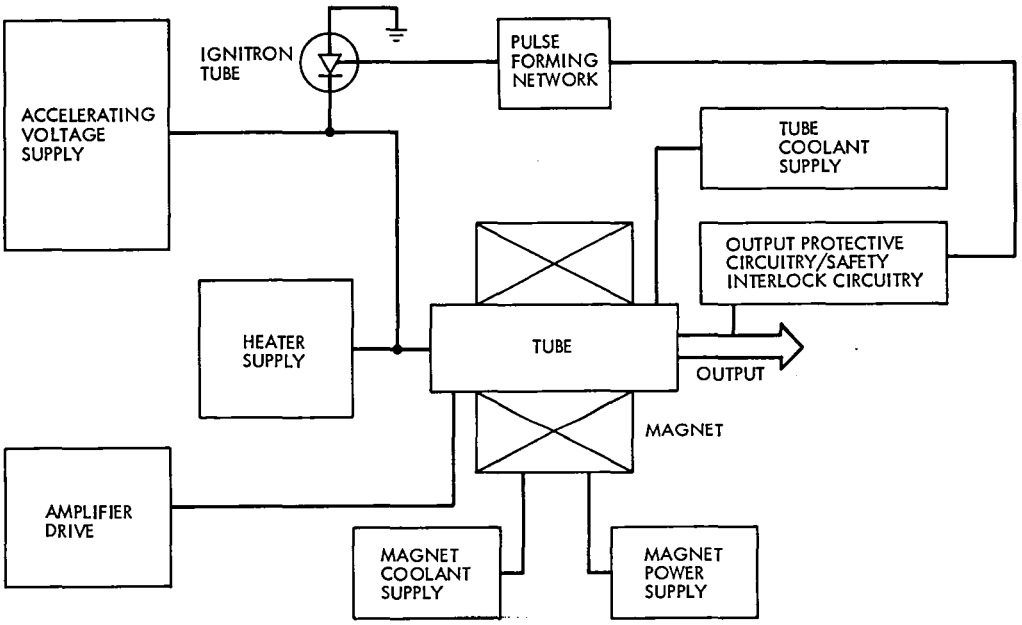

Fig. 2. System diagram: 34.3 GHz gyrotron TWT amplifier

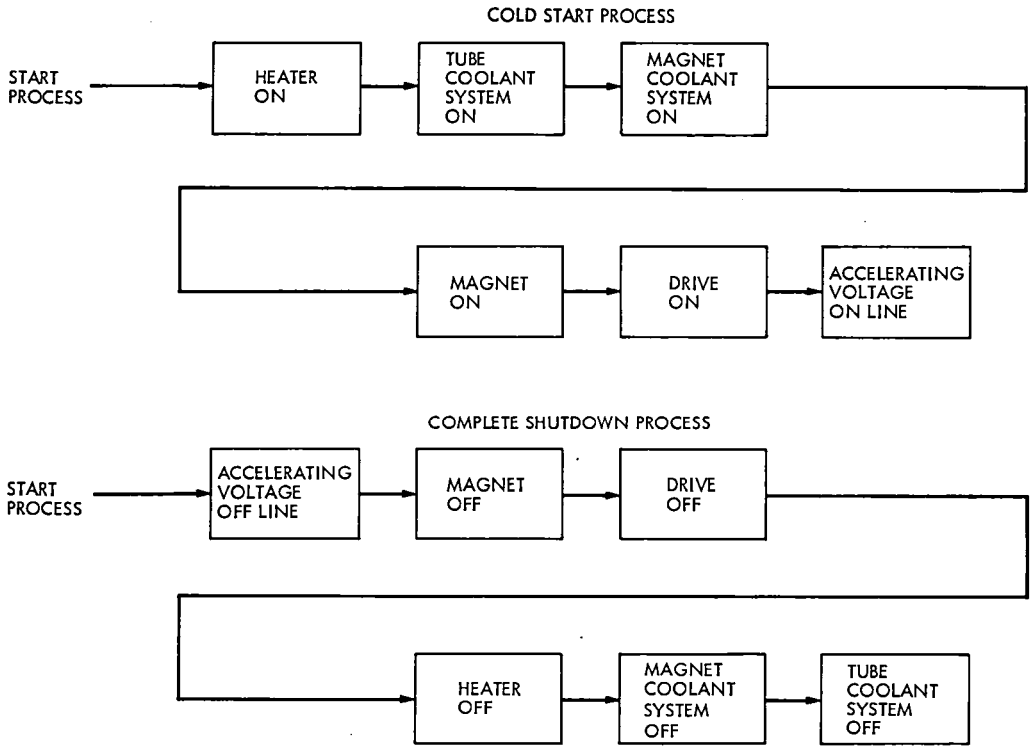

Fig. 3. Turn on/off sequences

Evaluation of the VA-876P Klystron for the 20-kW X-Band Uplink Transmitter

R. B. Kolbly
Radio Frequency and Microwave Subsystems Section

Initial evaluation test results of the proposed 20-kW X-band uplink klystron are presented. Operating parameters are compared with the existing DSN 20-kW S-band klystrons. Measured differential RF phase sensitivities vs operating parameter changes are exhibited.

I. Introduction

A future requirement exists for a 20-kW X-band (7145-7235 MHz) uplink transmitter for utilization in the Deep Space Network (DSN). Efficient spectrum utilization, improved charged particle calibration, and precision doppler experiments for relativity investigation are the key drivers. A developmental model is being designed and built for installation at DSS 13. It will be evaluated in this test bed for possible application in the DSN. A key element of this new transmitter is a phase-stable, reliable, and long life klystron amplifier. A survey of available klystron amplifiers indicated that Varian Associates Model VA-876 is the only commercially available klystron meeting the potential requirements for the transmitter. This article discusses work to date on the evaluation of this klystron as a suitable power amplifier for future DSN transmitters.

II. General

A comparison of the operating parameters of the VA-876P klystron with the 5K70SG klystron currently used in the DSN 20-kW S-band (2110-2120 MHz) transmitters (Table 1) indicated that it would be practical to install an X-band klystron in one of the two transmitter test beds located at the Microwave Test Facility (MTF) at Goldstone. By utilizing the MTF, experience could be obtained with this klystron without impacting DSS 13 or an operational DSN station.

The major modification required to the MTF transmitter for installation of an X-band klystron is the addition of a crowbar circuit to protect the klystron body structure in the event of a klystron beam intercept. Crowbar protection is not provided on the 20-kW S-band transmitters because the body structure is relatively massive and not as susceptible to damage from electron beam interception. Since crowbar technology has been developed for the high-power transmitters (Ref. 1), the design from DSS 13 was incorporated in the power supply at MTF. As the beam voltage for the 20-kW transmitter is considerably lower (20 kV as opposed to 70 kV), only one deck of the quad ignitron crowbar assembly was installed at MTF. Also, it was not necessary to use the corona shields at the lower voltage. Figures 1 and 2 show the crowbar installation in the 20-kV power supply.

The RF circuitry for both drive and output had to be completely replaced to be compatible with the higher output frequency. Figures 3ab and 4 show the klystron installation in the MTF test transmitter. Figure 5 is a simplified block diagram of the test configuration.

Testing the VA-876P klystron at the Microwave Test Facility has two purposes:

(1) Gain operating experience with the klystron and obtain reliability information.

(2) Measure the phase stability of the klystron as a function of various parameters (beam voltage, drive, temperature, etc.).

Other users of the VA-876 klystron have been contacted to determine if any reliability problems had been encountered. Two users (Hughes Aircraft and the British Post Office Department) were informally contacted and their history of the use of this klystron discussed. Both organizations are using them as satellite ground station transmitters at nominal outputs of 3-5 kW, continuous duty. Occasionally, power output was boosted at 10 kW for short periods of time. Neither user could furnish complete documentation; they felt the klystron gave approximately 8500 hours of service.

Since August 13, 1979, when the Varian VA-876P klystron (S/N 344) was placed in service, it has acquired approximately 200 beam operating hours, with 65 on-off cycles. The klystron has been operated under a variety of conditions, from low-power swept output to 20 kW CW output for as long as 8 hours at a time. Each day, prior to operation of the klystron, the crowbar and arc detector are tested.

Although there have been system faults, none have been related to the klystron. In particular, the high-voltage rectifier has failed, and there have been component failures in the crowbar logic. These faults have presented no danger to the klystron.

III. Phase Measurements

A Hewlett-Packard Model 8410A/8411A Network Analyzer was connected to two electric-field probes placed directly on the output and input waveguide of the VA-876 klystron. The probes were connected to the Network Analyzer by equal-length semirigid cables, and the output of the Network Analyzer was connected to a chart recorder. Phase variation as a function of the following parameters was recorded:

(1) Beam voltage.

(2) Drive power (AM/PM conversion).

(3) Magnet (focus) current.

(4) Inlet coolant temperature.

(5) Heater voltage.

Figures 6 through 10 show the measurement actual phase variations, and the results are summarized in Table 2.

Future reports will discuss transmitter centralized control overall design, control algorithms (saturation procedures, etc.), and further tests on phase stability. In addition, a report on X-band exciter design will be included.

Reference

1. Finnegan, E. J., "A New Dual Ignitron High Voltage Crowbar," Technical Report 32-1526, Vol. XVII, Jet Propulsion Laboratory, Pasadena, Calif., Oct. 15, 1973.

Table 1. Comparison of 5K70SG and VA-876P klystrons

Parameter	5K70SG	VA-876P
Tuning range	2100 - 2140 MHz	7145 - 7235 MHz
Bandwidth (– 1 dB)	14 MHz	45 MHz
Power output	20 kW	20 kW
Beam voltage	20 kV	19 kV
Beam current	2.3 A	2.6 A
Heater voltage	7.5 V	8.0 V
Heater current	12 A	8.0 A
Drive (20 kW saturated)	0.1 W	0.12 W
Coolant flows		
Collector	22 GPM	13 GPM
Body	1.5 GPM	2.0 GPM
Magnet	2.3 GPM	0.6 GPM

Table 2. Phase sensitivity of VA-876P klystron (S/N 344) (19-kV beam, 20-kW saturated output, 7190 Mhz)

Parameter	Sensitivity
Beam voltage	0.04 deg/v
Drive power	2.2 deg/dB
Focus current	–1.0 deg/A
Inlet coolant temperature	–1.3 deg/°C
Heater voltage[a]	4 deg/V

[a]Preliminary.

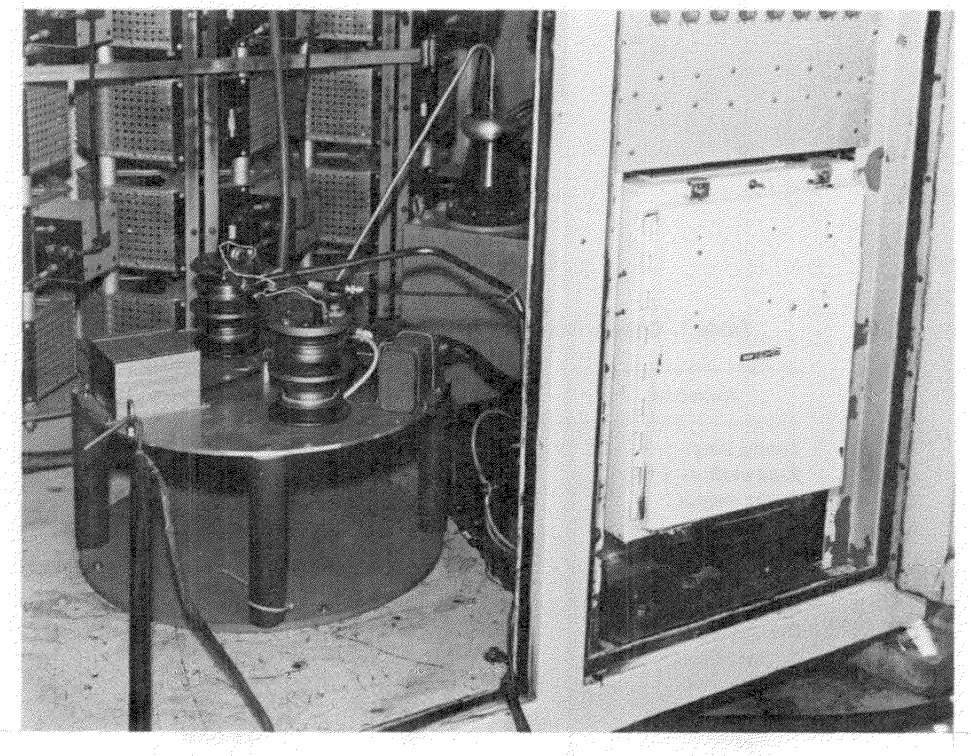

Fig. 1. Crowbar in high voltage power supply

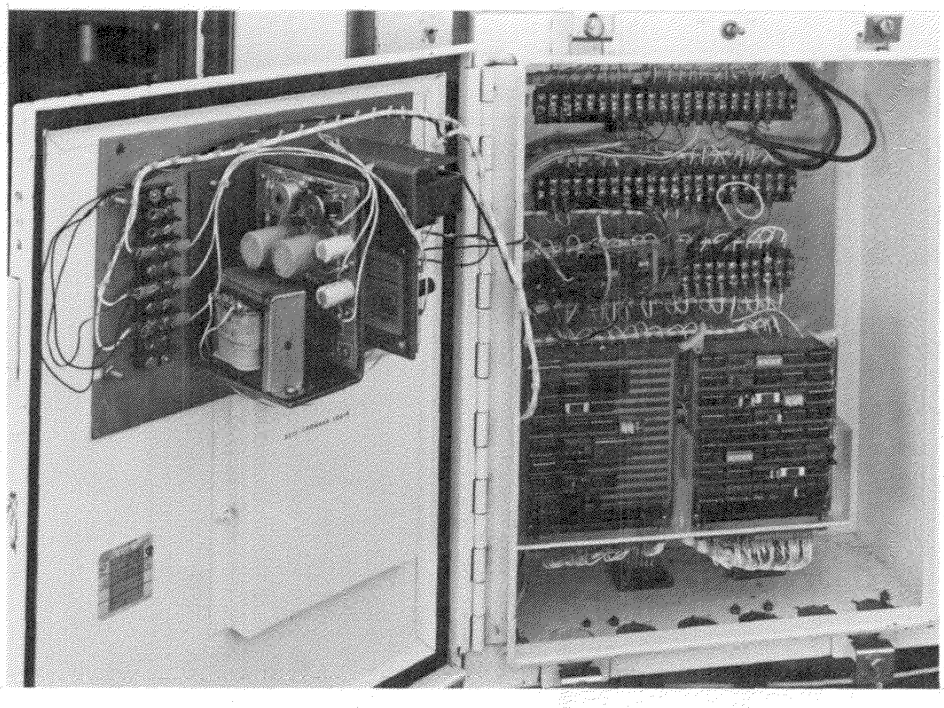

Fig. 2. Crowbar control logic

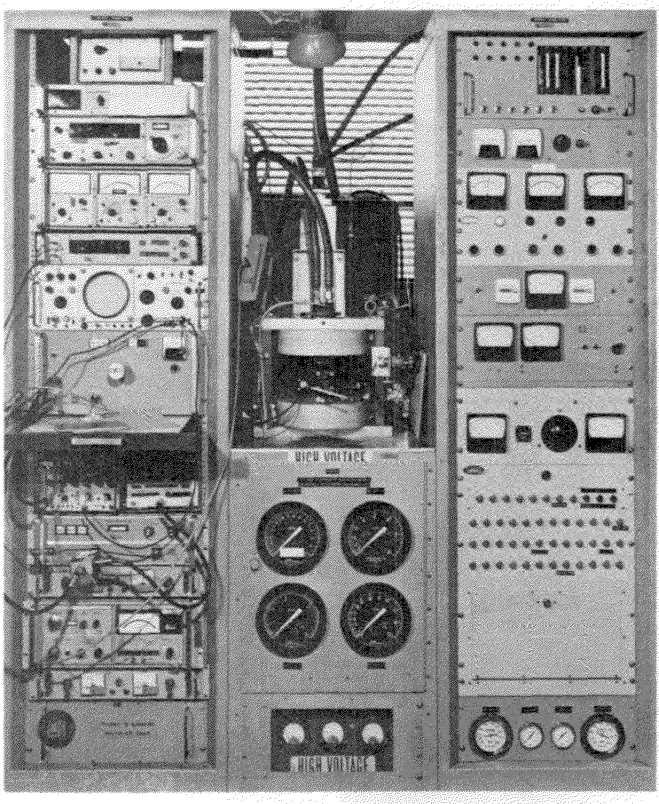

Fig. 3a. VA-876P in MTF klystron test stand

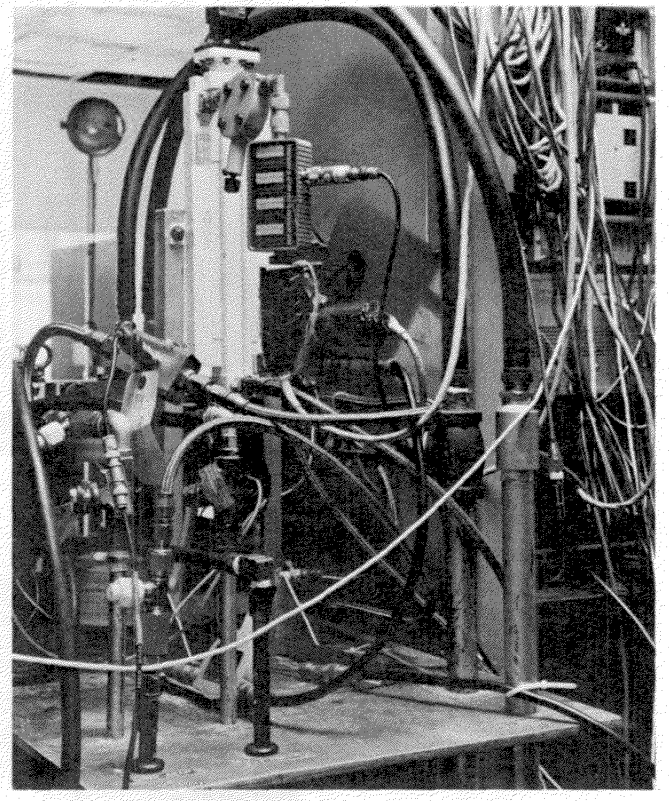

Fig. 3b. Rear view – VA-876P in klystron test stand

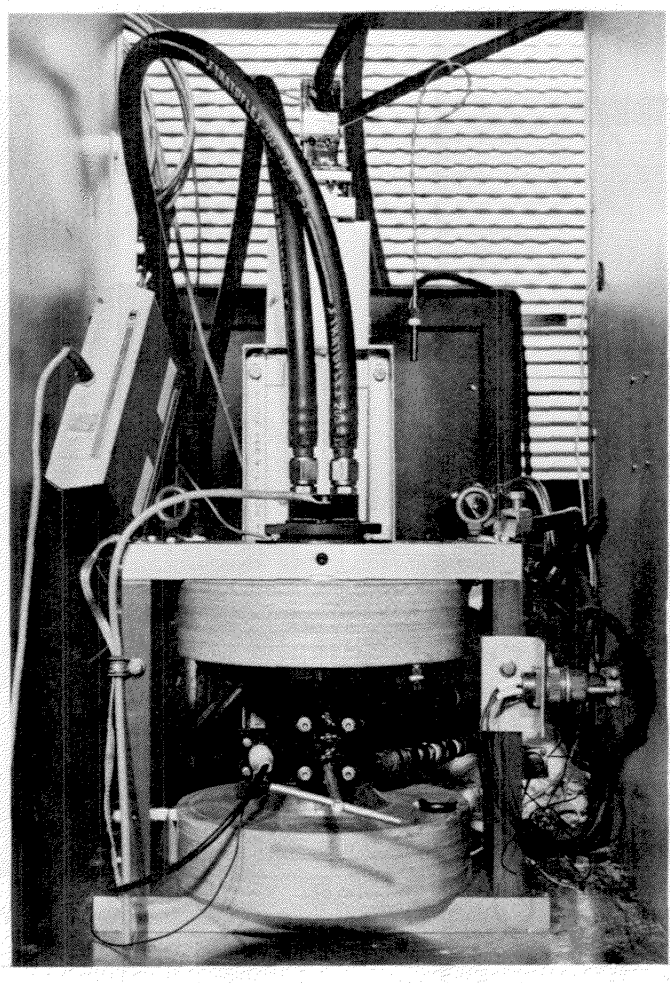

Fig. 4. VA-876P klystron and magnet

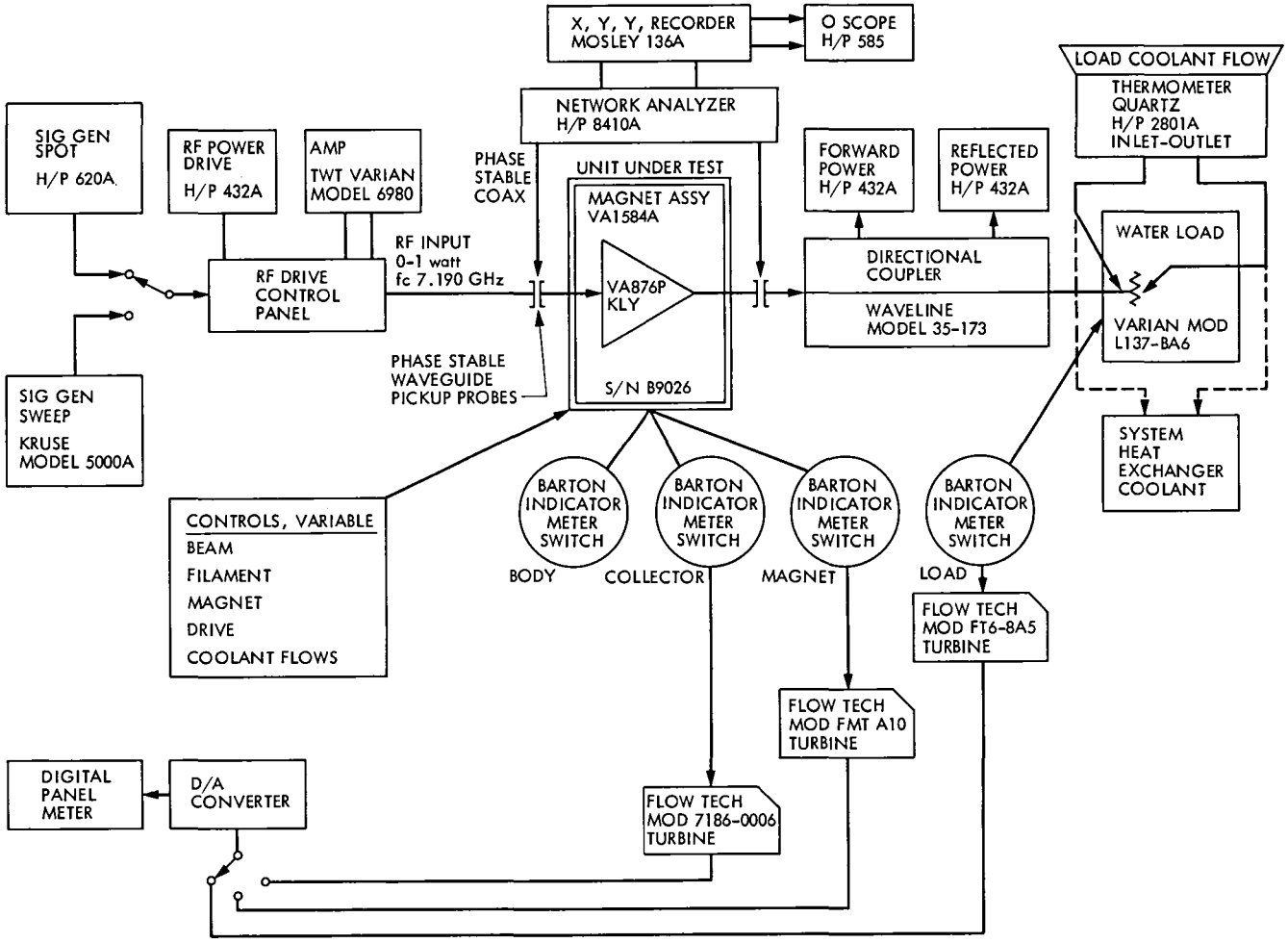

Fig. 5. System test configuration

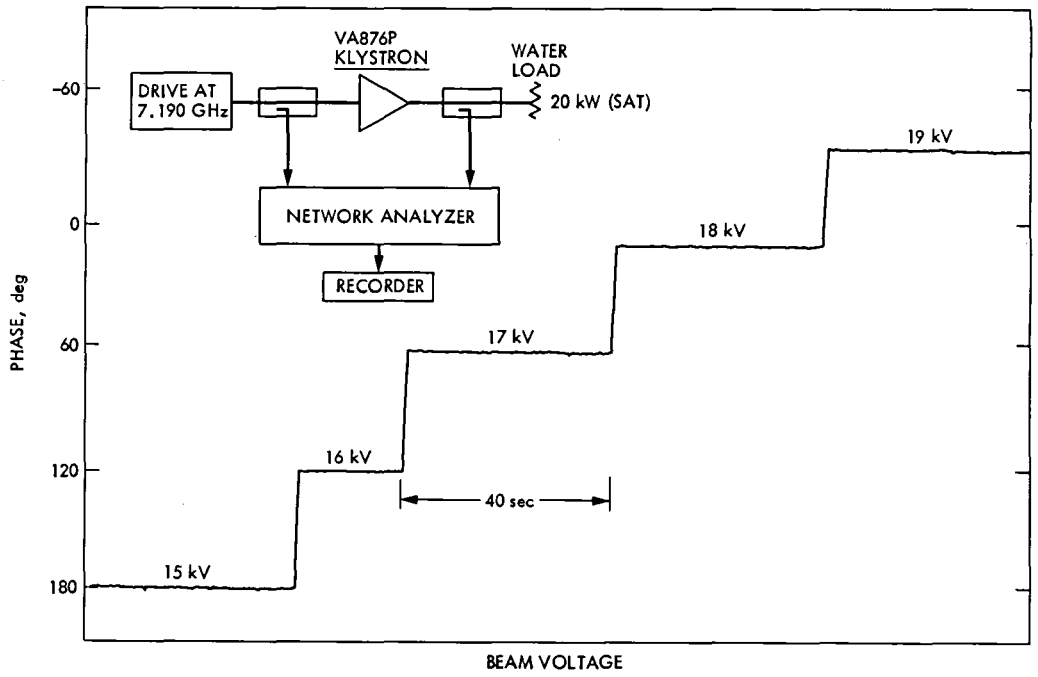

Fig. 6. Phase difference as a function of beam voltage changes

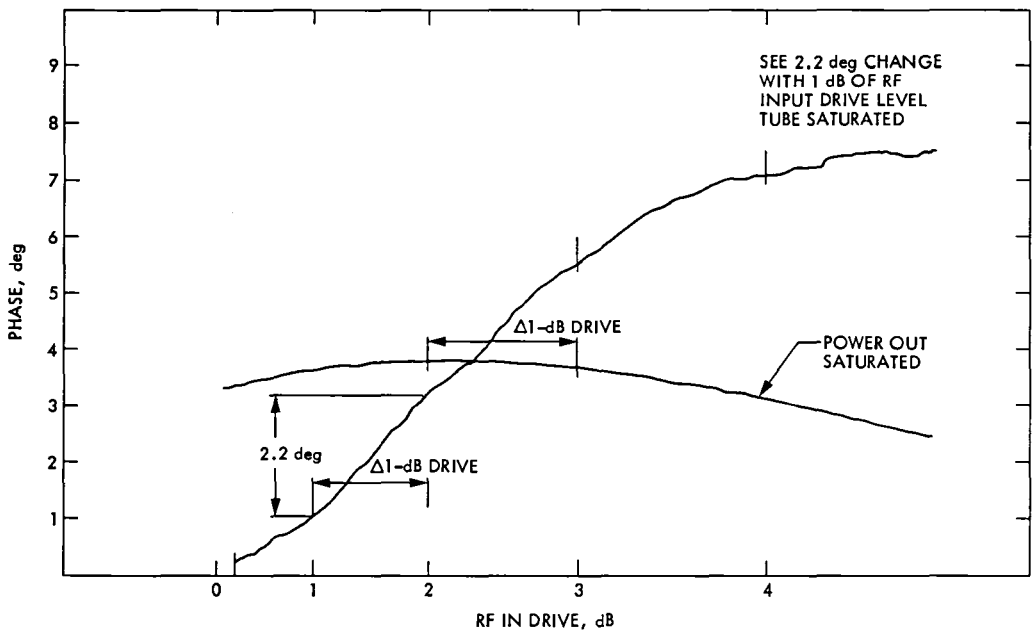

Fig. 7. Varian VA-876P X-band klystron phase change at saturation with 1 dB of input drive change

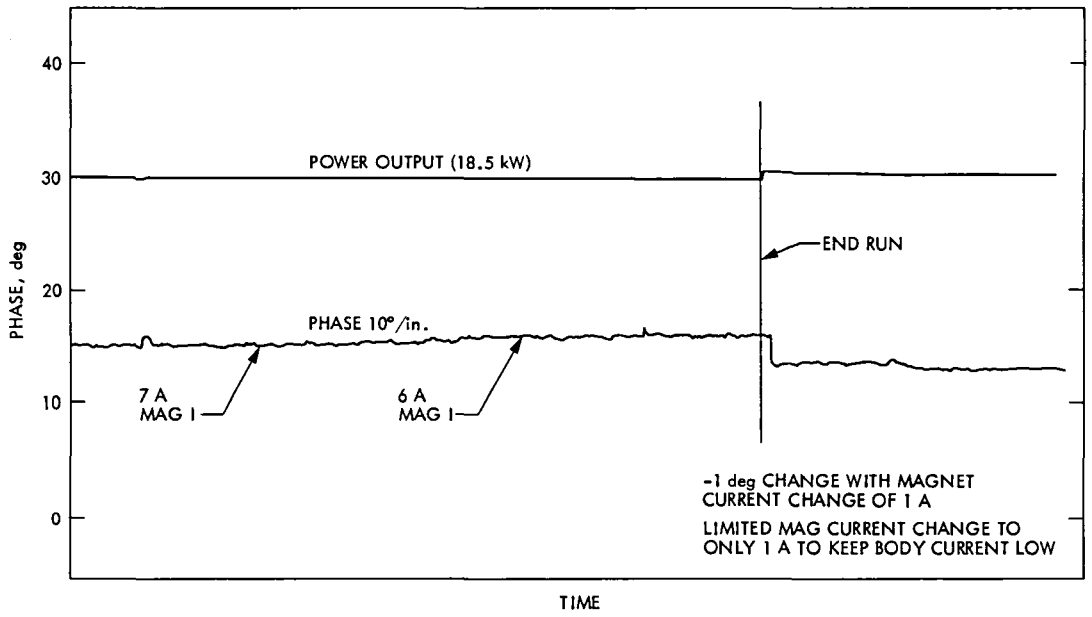

Fig. 8. Phase change vs magnet current, Varian VA-876P klystron S/N 334

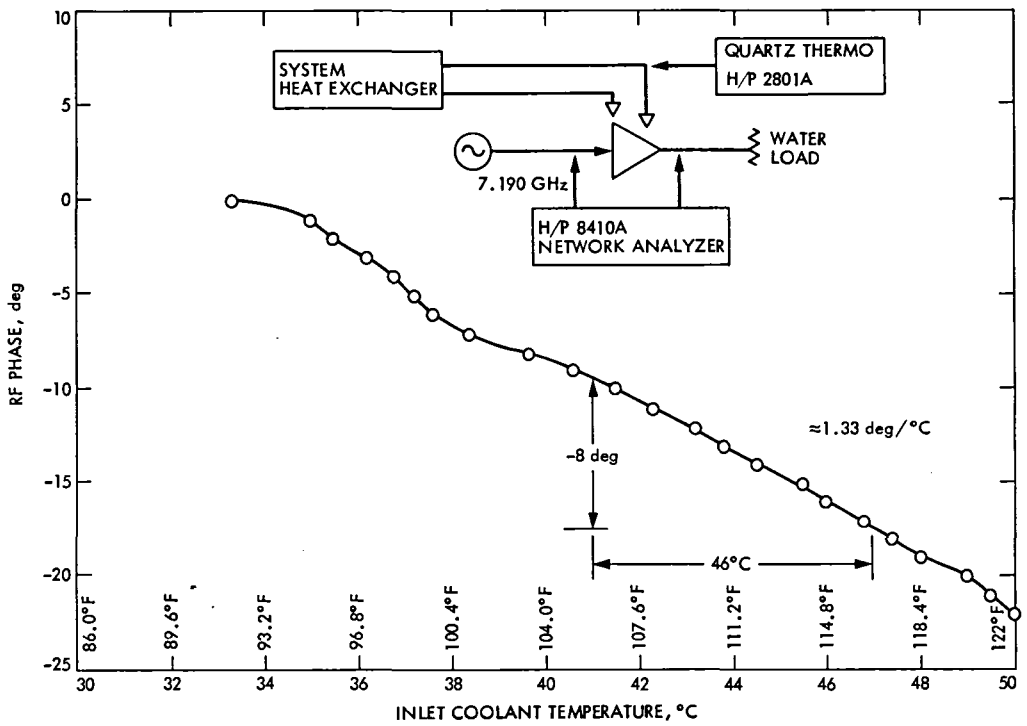

Fig. 9. RF phase change vs inlet coolant temperature

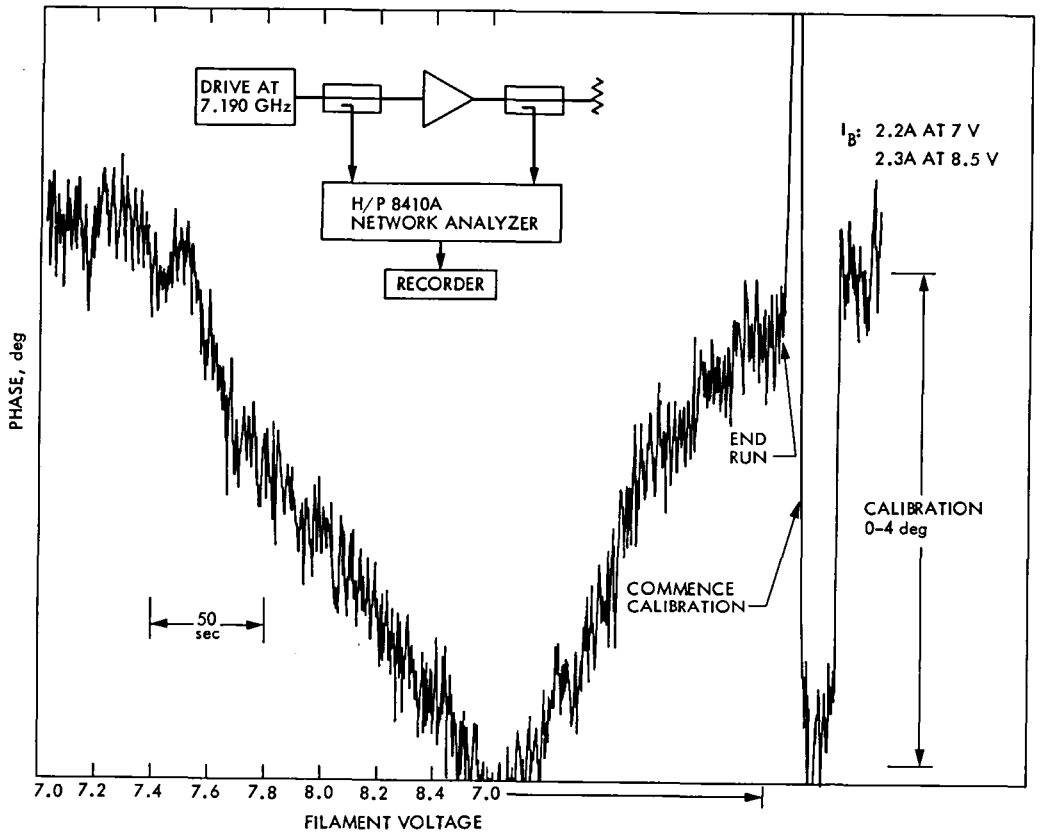

Fig. 10. Phase change vs filament voltage

A Computer-Aided Design System for Custom Large-Scale Integrated Circuits

M. W. Sievers
Communications Systems Research Section

This paper describes a computer-aided design system for custom large-scale integrated circuits. The system is composed of a high-level descriptive language and a SIMULA based language interpreter. The interpreter is running on the Caltech DEC SYSTEM 20 computer. It has been used to design a 16-bit self-checking comparator of medium-scale integration proportions.

I. Introduction

A general logic structure (GLS) for the design of custom integrated circuits has been discussed previously (Ref. 1). This is a matrixlike structure into which logic and wiring can be mapped. The simple and regular nature of the structure leads to a straightforward descriptive language and interpreter.

The descriptive language is based on the concept of a cell. A cell is a bounded region that may contain other cells, gates, and networks. This basis is amenable with structured, hierarchical design.

The function of the interpreter is to examine the design description and construct the cell "object" structures. Presently, it is possible to request cells to draw themselves either in a high-level notation consistent with the descriptive language or in the low-level detail required for mask making consistent with Caltech's NMOS design rules (Ref. 2).

Certain functions such as memory, pad drivers, and input protection diodes are best not constructed within the GLS structure. The facility for using such cells is not yet part of the design language. What is needed is to define cells whose input, output, and power wires are compatible with the GLS structure. Future versions of the language and interpreter will make use of these cells.

Several other modifications and additions are planned to increase the power of the design system. These will be mentioned in a later section. The design system is in its infancy at this time and is expected to grow in its capabilities.

The choice of SIMULA for the implementation of the interpreter will ease the work of making program changes. SIMULA is similar to many other block structured languages but has at least one significant dissimilarity. SIMULA is an object oriented language rather than data oriented language.

In SIMULA an object, called a CLASS, is defined that has various attributes associated with it. These attributes might be constants, variables, arrays, and procedures. Making interpreter changes requires the addition, deletion, or replacement of various CLASS attributes. Generally, these changes can be made within one CLASS without affecting other CLASSes. This is because each CLASS can be a totally self-contained object with little or no need for interaction with other CLASSes.

As already mentioned, SIMULA is an object oriented language. Section III will very briefly examine some of its more salient characteristics. Since data per se is not defined in SIMULA it is more meaningful to discuss object structures than data structures. The object structure created by the interpreter is specified in Section IV. Section V presents the descriptive language constructs and constraints. Section VI illustrates a typical design using the descriptive language. The next section introduces the high level GLS description upon which the design system is based.

II. High-Level GLS Notation

The GLS can be represented as a collection of unit gates interleaved with signal wires as indicated in Fig. 1. Each unit gate is represented by a rectangle. Signal wires are drawn as vertical lines.

A unit gate has two functions. It may be used either to create a NOR gate or as a wiring channel. The basic gate is a four port device in which any port may be programmed for either input or output. The ports are arranged two on each side of the gate. Unit gates may be coalesced into larger gates or wires. Only integral numbers of gates are defined, however. No problem occurs if gates cross power wires.

The unit gate defines the basic vertical unit of measure. For example, power wires are located on unit gate boundaries and pull-up resistors needed in the NMOS implementation are one unit gate long. Additionally, ground wires are assumed to be present at each unit gate boundary, unless certain conditions exist which are mentioned in Section V.

Signal wires adjacent to each unit gate column may be used to carry either power or signals vertically through the structure. These wires may be cut into arbitrary sizes as suit the design implementation. Signal wires exist for carrying signals horizontally but are omitted in Fig. 1 to reduce the clutter.

Figure 2 shows a static gated D flip-flop constructed in the high level notation. Flip-flop inputs and outputs are carried on horizontal wires. Arrows pointing into gates are input terms. Gates outputs are indicated by dots inside the gate. Dots at the intersection of vertical and horizontal wires indicate connection. Wide horizontal lines indicate a power bus and thinner vertical lines running from gates to a power bus represent a combination of pull-up and power connection.

Ground wires are not explicitly shown in Fig. 2 for reasons already mentioned. However, it may become necessary to periodically tie ground wires to a ground bus in larger designs. A facility exists for doing this (see Table 6 in section V).

Two constraints on designing with the GLS occur that may not be obvious from Fig. 2. The first is that all gates must start on odd numbered columns although wires may be placed in any column. This restriction is due to the GLS low level implementation and is made to enforce consistent column usage throughout a design. The second constraint requires that no gate input be made in the same row on the right side of a gate in column i - 1 or on the left side of a gate in column i + 1 as a contact made in column i. This again is due to the GLS implementation. Violating this rule would result in the creation of gates that probably would not be capable of successfully driving their fanout.

III. A Brief Look at SIMULA

SIMULA is a block structured language most similar to ALGOL. It is unique in that it is oriented toward objects, called CLASSes, rather than toward data. A CLASS is an instance prototype that consists of three major parts:

(1) Head.

(2) CLASS definition body.

(3) Initialization body.

The head part names the CLASS, defines parameters needed to create instances of it, and establishes it within a hierarchical CLASS structure. The CLASS definition body is the set of constants, variables, and procedures that make up the CLASS. Procedures are not executed unless called. The initialization body is a special procedure that is executed upon the creation of each CLASS instance.

CLASS instances are created by the construct

```
NEW classname (parms);
```

where classname is the name of an existing CLASS and parms are the parameters required by that CLASS. Reference variables may be declared which are used as pointers to CLASS instances. Thus if a and b are declared as reference pointers to CLASS c then after execution of the segment

```
a: – New c (parms);
b: – New c (parms);
```

two instances of CLASS c exist with a pointing to one and b the other. Instances remain accessible until all of their reference pointers have been destroyed. If

```
a: – b: – New c (parms);
```

the single instance of object c created remains until both a and b no longer point to it.

Each instance created effectively has a full copy of all attributes defined by the associated CLASS. Thus procedures within several instances of the same CLASS may be executed in parallel without the usual concerns of program sharing. In reality of course, only a single copy of each CLASS exists and SIMULA maintains the required data structures for segment sharing.

CLASSes may be made subsets of other CLASSes by prefixing the CLASS head with the name of another CLASS. So

```
a CLASS b;
a CLASS c;
b CLASS d;
```

establishes the following CLASS hierarchy.

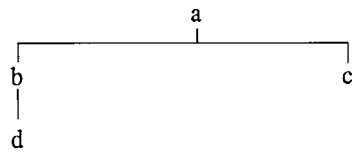

Each sub CLASS has all of the attributes of each of its super CLASSes. A super CLASS, however, has none of the attributes defined within its sub CLASSes. Further, each creation of a sub CLASS object results also in the creation of instances of all of its super CLASSes.

Attributes of instances are always visible from within the instance and can be visible externally unless otherwise protected. It is also possible to define virtual attributes. For example a super CLASS s can declare a VIRTUAL PROCEDURE p. Sub CLASSes of s each define a PROCEDURE p. A reference made to the virtual PROCEDURE p in s will cause the actual procedure to be executed in the sub CLASS. For example, if

```
CLASS s;
VIRTUAL: PROCEDURE p;

s CLASS b;
BEGIN
PROCEDURE p;
END;

s CLASS c;
Begin
PROCEDURE p;
END;
```

then if d, and e are made CLASS s references and are assigned instances by

```
d: – NEW b;
e: – NEW c;
```

a reference to p in the s object d will pass control to p in object c. Similarly, a reference to p in s object e will pass control to p in object c. The advantage of this is that it is possible to declare a CLASS as a super CLASS for many objects and to refer to any instance of these many objects by the single super CLASS. A reference to any virtual attribute of the super CLASS will result in a reference to the actual attribute in the sub CLASS that qualifies the super CLASS. The alternative to this capability is to test each super CLASS reference to determine which of its sub CLASSes qualify it and then access the attribute of the sub CLASS directly. Testing is slower and considerably less elegant than the VIRTUAL declaration approach.

IV. Interpreter Object Structure

The high-level language interpreter is based on the object hierarchy shown in Fig. 3. CLASS thing is an object that basically has no attributes. It is defined within CLASS things on top of which the interpreter is written; i.e., things is external to it. Object thing is defined to be a super CLASS for all objects. CLASSes celldef, network, nodes, gaterep, and pwrwire are all thing sub CLASSes.

Object celldef is the cell definition prototype. Its attributes and their meaning are listed in Table 1. The network object is defined by two nodes objects. Table 2 lists its attributes. CLASS nodes is composed of virtual attributes only. It is defined to be the super CLASS for all node objects. Therefore, for example, requests generated in CLASS network procedures to produce high- or low-level descriptions of its defining nodes can be directed toward nodes CLASS objects. CLASS network need not test to determine what type of node is actually present. Virtual attributes of nodes are indicated in Table 3.

Nodes subclasses transistor, contact, gndcontact, pin, and powercontact each contain the actual procedure definitions declared VIRTUAL in CLASS nodes. Transistor has an additional local attribute that flags which side of the gate it is on. This attribute is not visible at the nodes level.

The gaterep object is the gate prototype. Its attributes are found in Table 4. Object pwrwire is the power wire definition. Table 5 lists its attributes.

V. Design Language

The design language has the syntax of SIMULA and contains constructs for creating cells, making instances of cells, and preparing output files of cell descriptions. In addition to these constructs, any legal SIMULA code may be included in a chip description.

A chip is described as a collection of cell definition blocks. The start of each such block is indicated by

```
create (cellname);
```

where cellname is a text string. Each time a create is executed, the interpreter makes a new instance of celldef. Every cell definition block is terminated by an endcreate statement. This statement takes the cell just defined and enters it into a cell dictionary for future reference.

The body of a cell definition block contains the constructs that define elements within the cell. At present, a cell definition block cannot contain a create statement. This restriction is arbitrary and could be eliminated. Table 6 lists the body constructs.

After a cell has been defined, it may be translated into an output file in either its high- or low-level form. High-level output is requested by hllplot (cellname) and low-level output by goryplot (cellname). An output file may be displayed or translated into a mask set. It is necessary, however, to request a goryplot for actual mask making.

Two language precautions arise due to the interpreter implementation. These are:

(1) When cells overlap and any of these has a power wire contained within the overlapped region, then all cells must declare a power wire within that region. This is necessary because each cell is responsible for drawing its own ground wires. Ground wires are drawn across a cell on unit gate vertical boundaries unless a power wire or subcell is found in its path. If one declares a power wire, that wire is not visible outside of that cell definition. A cell sharing a common region with that cell will insert a ground wire under the power wire declared in the first cell since its existence is unknown. The result could be a short from power to ground at a pull-up resistor.

(2) All cells in which a gate is declared must have a suitably located power wire declared. Again, power wires declared outside of a cell definition are unknown within the cell. Gates must have clear access to power wires to which they can be connected.

In addition to these precautions, there are a few limitations due to interpreter implementation:

(1) Nested cell definitions are not permitted.

(2) Cells may be stretched only once.

(3) No provision has been made to include cells defined outside of the design language.

(4) Only NMOS devices can be created.

These precautions and limitations are fairly minor and do not hinder the specification of a complete chip. Modifications to the interpreter are planned to remove most of them.

VI. A Typical Design

The static register cell in Fig. 2 is implemented in the design language. Figure 4 shows the language description of the register. Figure 5 shows a black and white copy of a color plot of the high level description produced by the code in Fig. 4. Figure 6 shows a black and white copy of a color plot representing the mask level details of Fig. 5.

As a final example, Fig. 7 illustrates a black and white version of a color plot showing a 16-bit self-checking comparator (Ref. 3) designed by the system. The pads and drivers were added by merging a file containing their description with the file produced by the interpreter. This chip is part of one of the Caltech class chip projects and will be fabricated by November 1979.

VII. Conclusions

A descriptive design language and interpreter are now available for defining the logic "core" of an integrated circuit. Additions are planned to increase the design system capabilities to include cells not created in the GLS. Further additions might also include logical and electrical simulation of the devices created.

References

1. Sievers, M. W., "A General Logic Structure for Custom LSI," in *The Deep Space Network Progress Report 42-50*, Jet Propulsion Laboratory, Pasadena, Calif., April 15, 1979, pp. 97–105.

2. Mead, C., and Conway, L., Introduction to *VLSI Systems*, 1978, ch. 2., text in preparation.

3. Carter, W. C., Wadia, A. B., and Jessup, D. C., "Implementation of Checkable Acyclic Automata by Morphic Boolean Functions," Symposium of Computers and Automata, Polytechnic Inst. of Brooklyn, April 1971, pp. 465-482.

Table 1. celldef attributes

Attribute	Comment
x, y	Unit gate location of lower left corner
networklist	List of networks
subcellist	List of subcells
pwrlist	List of power wires
gatelist	List of gates
mybox	A rectangle defining the bounding box
boundingcell	The next highest celldef in a hierarchical design.
stretched	Boolean variable indicating whether or not the cell has been stretched
PROCEDURE vertstretch	Produces a vertically stretched copy of the cell; stretching is nonlinear in that only objects above a given row number are moved up
PROCEDURE horizstretch	Produces a horizontally copy of the cell; the nonlinear comment above applies here to column number
PROCEDURE squoosh	Produces a cell both horizontally and vertically stretched.
PROCEDURE makegore	Does a recursive descent through cell hierarchy to make detailed mask description
PROCEDURE makehll	Makes a high level description of the cell; subcells are represented by their bounding box
PROCEDURE bbox	Computes the bounding box.

Table 2. network attributes

Attribute	Comment
node1, node2	Nodes objects defining the network endpoints
PROCEDURE morenodes	Adds additional nodes to network defined by node1, node2
PROCEDURE makehll	Requests nodes objects to make their high level description, draws in a connecting wire
PROCEDURE makegore	Requests nodes objects to make detailed description, connects nodes objects with a wire and inserts crossunders as required.

Table 3. nodes attributes

Attribute	Comment
VIRTUAL PROCEDURE hllx	Returns high-level x location from nodes sub CLASS
VIRTUAL PROCEDURE hlly	Returns high-level y location from nodes sub CLASS
VIRTUAL PROCEDURE gorx	Returns low-level x location from nodes sub CLASS
VIRTUAL PROCEDURE gory	Returns low-level y location from nodes sub CLASS
VIRTUAL PROCEDURE myy	Returns unit gate row number from nodes sub CLASS
VIRTUAL PROCEDURE myx	Returns column number from nodes sub CLASS
VIRTUAL PROCEDURE makehll	Requests nodes sub CLASS to make its high-level description
VIRTUAL PROCEDURE makegore	Requests nodes sub CLASS to make its low-level description
VIRTUAL PROCEDURE xgets	Replaces nodes sub CLASS column number with passed parameter
VIRTUAL PROCEDURE ygets	Replaces nodes sub CLASS unit gate row number with passed value
VIRTUAL PROCEDURE copynode	Creates a copy of the nodes sub CLASS

Table 4. gaterep attributes

Attribute	Comment
x, y	Location of bottom-most unit gate
size	Length in unit gates
side	Side, top or bottom, to which power will be connected
PROCEDURE hllx PROCEDURE hlly PROCEDURE goryx PROCEDURE gory	Same function as listed in Table 3 as applied to gates
PROCEDURE makegore	Makes low level details if gate, cross-unders are inserted as necessary, connects gate to pull-up and power
PROCEDURE makehll	Makes high level gate description, connects gate to power.

Table 5. pwrwire attributes

Attribute	Comment
x, y	Row and column location of left-most point
length	Length in columns
PROCEDURE hllx PROCEDURE hlly PROCEDURE gorx PROCEDURE gory PROCEDURE makehll PROCEDURE makegore	Same as Table 3 as applied to power wires

Table 6. Interpreter constructs

Construct	Comment
plop (cellname, location);	Creates an instance of cell named cellname and places it at position location; location is the row and column of the lower left corner of the cell
vertput (cellname, location, row, howmuch);	Creates an instance of cell cellname at location; all elements above row are moved up by howmuch
horizput (cellname, location, col, howmuch);	Creates instance of cell cellname at location; all elements to the right of col are moved 2 * howmuch columns.
vhput (cellname, location, row, howmuchr, col, howmuchc);	Does both vertical and horizontal stretches
gate (loc, size, side);	Creates an instance of gaterep at location loc, size unit gates long, with power connected to side ("top" or "bottom")
power (loc, length);	Creates an instance of a power wire starting at loc, length columns long
connect (node1, node2) < • morenodes (node) > ;	Creates a network between nodes objects node1 and node2; additional nodes are added via morenodes
input (loc, row, side);	A gate input nodes object for connect, creates a transistor instance at gate defined at loc, at row ports from the bottom of the gate, on side ("left" or "right")
output (loc, row);	Gate output from gate defined at loc at row ports from the gate bottom; a contact instance is created
con (loc, row);	Vertical to horizontal wire contact, loc, row same as above
pwrcon (loc);	Connection to a power bus
gndcon (loc);	Connection to ground bus
io (name, loc, row);	Cell input-output node, creates a pin instance labeled name

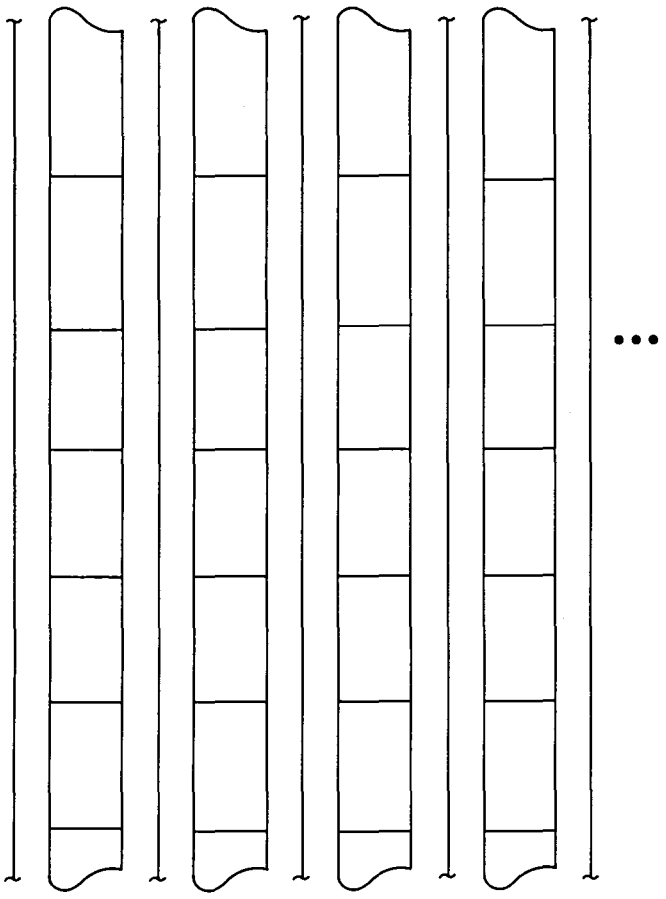

Fig. 1. High-level representation of GLS matrix

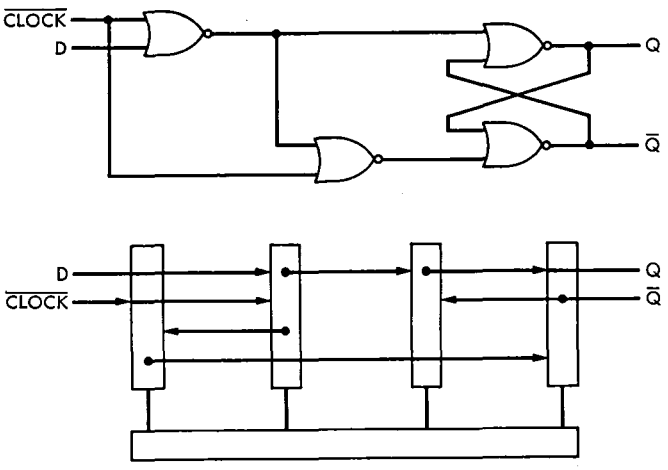

Fig. 2. Static gated D flip-flop

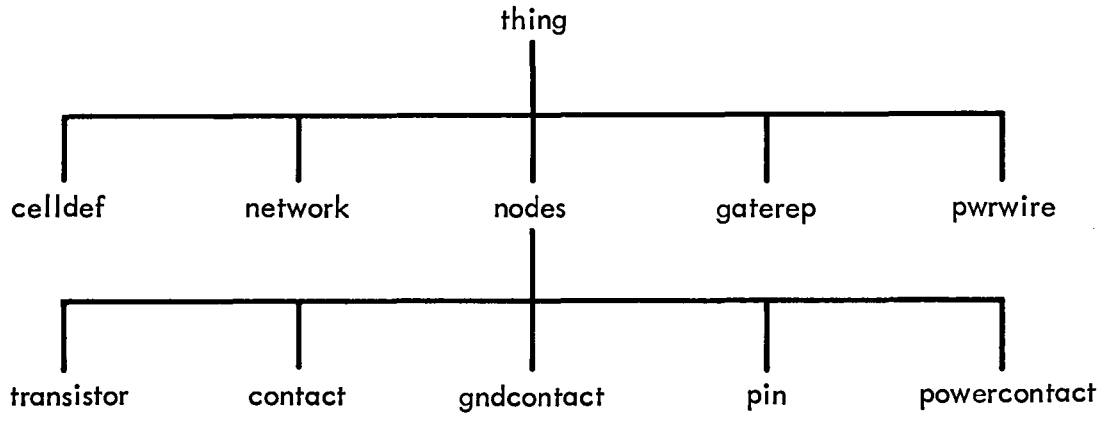

Fig. 3. Interpreter object hierarchy

```
create ("flipflop");
power (0, 0, 7);
gate (1, 1, 2, "bottom");
gate (3, 1, 2, "bottom");
gate (5, 1, 2, "bottom");
gate (7, 1, 2, "bottom");
connect (io ("D", 0, 1, 4), input (3, 1, 4, "left"));
connect (output (3, 1, 4), input (5, 1, 4, "left"));
connect (output (5, 1, 4), input (7, 1, 4, "left"))
    . morenodes (io ("Q", 8, 1, 4));
connect (io ("CK", 0, 1, 3), input (1, 1, 3 "left"))
    . morenodes (input (3, 1, 3, "left"));
connect (io ("NQ", 8, 1, 3), output (7, 1, 3))
    . morenodes (input (5, 1, 3, "right"));
connect (output (3, 1, 2), input (1, 1, 2, "right"));
connect (output (1, 1, 1), input (7, 1, 1, "left");
endcreate;
```

Fig. 4. Program for describing static D flip flop

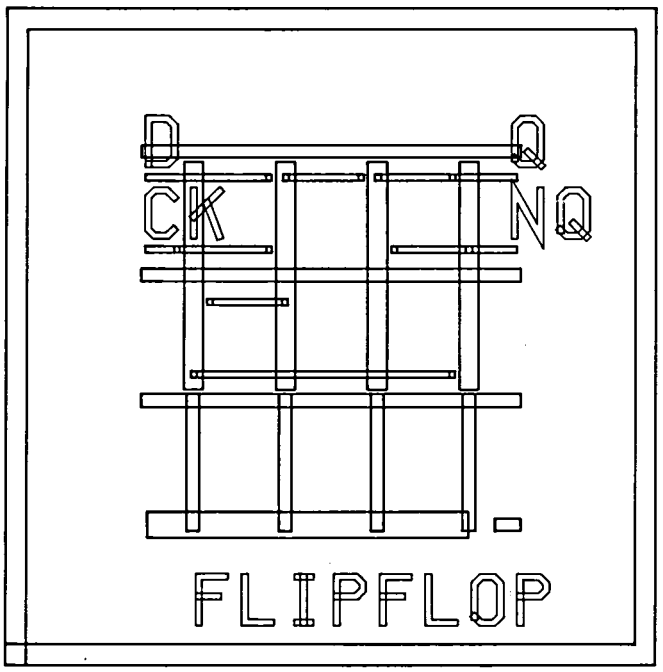

Fig. 5. High-level flip-flop description

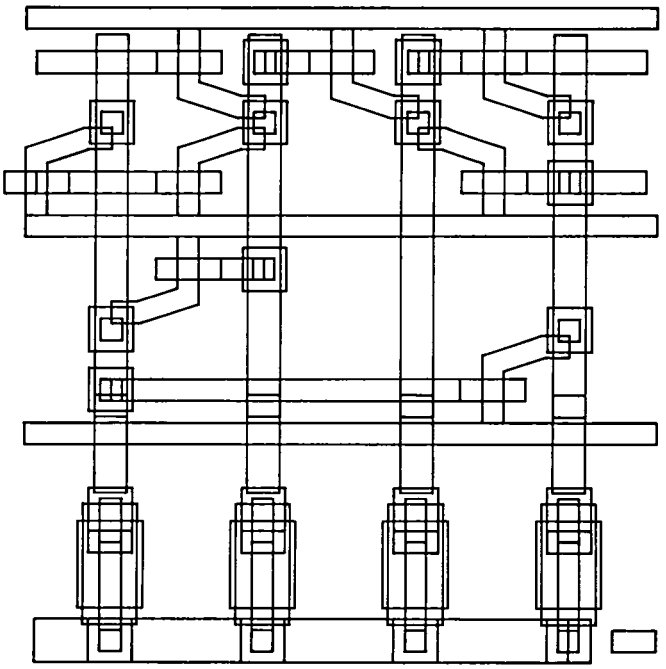

Fig. 6. Mask level flip-flop description

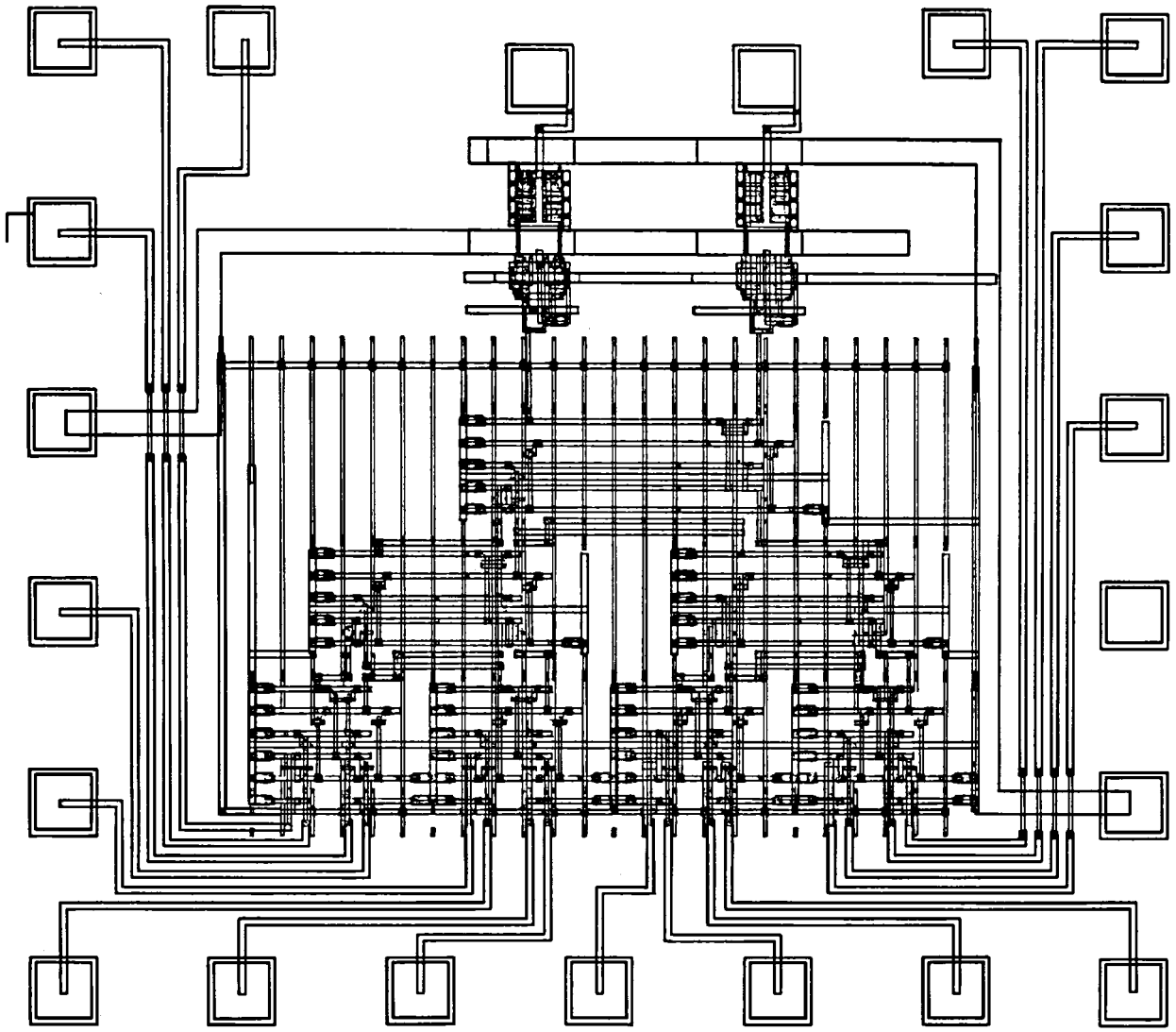

Fig. 7. 16-bit self-checking comparator

A Study of the Influence of Oil Saturation on the 64-Meter Antenna Hydrostatic Bearing Grout

H. P. Phillips and A. A. Riewe
DSN Engineering Section

M. Polivka and P. K. Mehta
University of California, Berkeley

Deterioration of the grout supporting the hydrostatic bearing runners in the DSN 64-m antennas has been a continuing maintenance problem. This paper describes an investigation, carried out at the University of California at Berkeley, into the effect of oil saturation on the grout. It is concluded that oil saturation as such did not significantly affect the strength of the concrete in either static or cyclic loading. The possibility is raised that the presence of oil as the concrete is placed may inhibit the development of the full strength of the material.

I. Introduction

Deterioration of the grout under the hydrostatic bearing runner of the 64-m antennas has caused a continuing maintenance problem to assure adequate flatness of the runner. Oil leaking from the reservoir formed by the runner and the side walls has been considered the prime factor in this deterioration. Two mechanisms of failure have been considered: decreased compressive stress of the grout material due to oil saturation, and erosion of the grout by hydraulic action under cyclic loading. Tests of these two mechanisms have been carried out by JPL at a local laboratory and by Professors M. Polivka and P. K. Mehta of the University of California at Berkeley under contract from JPL. Neither failure mode could be demonstrated in laboratory tests. However, a third failure mode was proposed wherein the presence of oil on the under surface of the runner sole plates at the time the grout is placed chemically inhibits setting up the cement in the grout after placement. This mechanism has not yet been tested.

II. Description of the Hydrostatic Bearing

The hydrostatic bearing consists of three pads, supporting the corners of the alidade, running on a steel runner 22 m (72 feet) in diameter (Fig. 1). Oil forced through recesses in the pads forms a thin pressurized film between the pad and the runner providing a very stiff and low friction bearing. Walls are mounted on the inner and outer edges of the runner to form a reservoir into which the oil is discharged and from which it is drawn for recirculation through the pumping system. The runner is made up of 11 segments fastened together with moment- and shear-carrying joints to form a continuous ring. While all of the joints are carefully sealed, oil leakage may occur at the runner joints and between the reservoir walls and the runner edges. The runner sits on sole plates which in turn are supported on a dry-packed grout. The grout is placed after the runner has been leveled, with the sole plates brought up hard against the bottom of the runner. The sole plates are

keyed into the grout, while the runner can move across them if required by thermal expansion and contraction.

III. Grout Material

The "dry-pack" grout is composed of a mixture of 1 part Type II portland cement to 1.5 parts (by weight) washed concrete sand. Sufficient water is added and mixed in so that the material upon placement and packing under the sole plate will hold together and retain its dimensions and density. The water-cement ratio (by weight) is approximately 0.23 for the materials used at Goldstone. The grout material characteristically has a compressive strength of 6.9-8.3 MPa (10,000-12,000 psi).

The dry-pack grout mixture is definitely dry – so dry that even engineers experienced in concrete construction may consider it unfit for use. Actually, usual plastic concrete mixes contain almost twice as much water as is required for the full hydration of the cement, the extra water being necessary to make the concrete workable and placeable.

IV. Tests on Oil Saturated Grout Material

A. Test Description

The first series of tests were made for compressive strength and modulus of elasticity of dry-pack mortars and concretes, with and without oil-saturation. Also determined were the drying shrinkage characteristics of the untreated (no oil) mortars and concretes. In the first phase (Phase I) of this test program, the aggregates used were laboratory selected materials, and in Phase II the aggregates were of the same type and from the same sources as those used for the dry-pack mortar currently being employed in the grout replacement program of the antenna at DSS 14. In addition to Type II portland cement, a mixture using ChemComp cement was also included in Phase II of the test program in order to evaluate its potential in reducing the shrinkage and oil absorption characteristics of the dry-pack mortars and concretes. The mix proportions of 1:1.5 (cement:aggregate) used for the mortars and concretes of this investigation are the same as those used for the actual antenna grout at DSS 14. The aggregate in the mortar mixes was only washed concrete sand, whereas for the concrete the aggregate was about a 50:50 blend of washed concrete sand and 3/8-inch pea gravel.

The dry-pack mortar and concrete specimens were cast in steel molds, being compacted in layers by the use of a pneumatic sand tamper. The oil used for saturation of the mortars and concretes was ARCO-DURO 700 hydrostatic bearing oil, which is the same type of oil used in the bearings of the antennas. More detailed information on the materials used, preparation of specimens, and test procedures is given in Appendix A.

B. Test Results

Results obtained in the two phases of the test program are summarized in Tables 1 and 2. These results show that oil saturation of the dry-pack mortars and concretes has no significant influence on their compressive strength or compressive modulus of elasticity. Averaging all of the test results obtained on both the dry-pack mortars and concretes, oil saturation reduced their average compressive strength from 8.0 to 7.66 MPa (11,160 to 11,110 psi) and the modulus of elasticity from 4.23 to 4.20. These very small differences in the average values seem to indicate that oil saturation has no effect (8.0 to 7.66 MPa) on strength or modulus of elasticity, and that any differences observed for a given group of dry-pack mortar or concrete specimens are probably due to experiment variations during preparation of specimens, oil saturation and testing. Results also show that the use of ChemComp cement instead of the Type II cement (Table 2) did not have any significant influence on compressive strength or modulus of elasticity of the dry-pack mortar or concrete.

The average oil absorption of the mortars and concretes was about 3.5 percent (oven-dry basis), which is about the same as that determined in earlier tests made by the Smith-Emery Company, as shown in their report dated December 15, 1975. As is to be expected, the oil absorptions are slightly lower for the concretes than for the corresponding mortars. The same is true for the drying shrinkage. The use of the ChemComp cement, although reducing the net drying shrinkage, did not reduce the oil absorption of the dry-pack materials.

C. Conclusions

Based on the results of the first series of tests, it may be concluded that oil saturation of short duration, as used in this test program, has no significant effect on the compressive strength or modulus of elasticity of the dry-pack mortars or concretes. The materials and mix proportions currently being employed for the runner grout at the Goldstone Antenna produce a dry-pack material of high strength and low shrinkage characteristics.

V. Tests of Cyclic Loading of Oil Saturated Grout

A. Test Description

The second and final series of tests were carried out to determine the influence of oil saturation of laboratory prepared mortar samples subjected to cyclic and long-term static

loading (creep tests). Also determined was the influence of degree of oil saturation of field samples on compressive strength.

B. Tests on Laboratory Prepared Mortars

In this investigation laboratory prepared dry-pack mortars were evaluated under cyclic and long-term static load conditions (creep), with and without oil saturation. The sand and the Type II cement used in the preparation of the laboratory mortars were of the same type and from the same sources as those being employed in the grout replacement program of the Goldstone Antenna. Also, the mix proportions of 1:1.5 (cement/sand) and the water-cement ratio of 0.22 used for the mortars are similar to those used in the field.

As in the tests on oil saturated grout material, the dry-pack mortar specimens were cast in steel molds and compacted in 3.8 cm (1-1/2-in.) layers using a pneumatic sand tamper. The oil used for saturation was ARCO-DURO hydrostatic bearing oil, which is the same type of oil used in the bearings of the antennas. More detailed information on the materials, mix proportions, mixing and casting procedures and oil-saturation of the specimens is given in Appendix A.

C. Effect of Cyclic Loading

The influence of cyclic loading on oil saturated mortar was determined by applying a cyclic compressive load on the top surface of a mortar specimen, which simulates the interface between the mortar and the steel plate at the Goldstone Antenna. The specimen used was 5.24 cm (6 in.) in diameter and 5.08 cm (2 in.) thick and was immersed in an oil bath during the cyclic loading to ensure that a film of oil is present between the top surface of the mortar and the steel plate transmitting the cyclic load, as is the case in field application. The specimen was subjected to a total of 21,000 cycles in compression, of which the first 13,500 were from 34 KPa to 724 KPa (50 to 1050 psi).

The cyclic load test was performed in a MTS cyclic testing machine. Each cycle, which lasted 60 s, had the load maintained for 27.5 s, a rest period of 27.5 s, with the loading and unloading being done in 2.5 s. Every few hundred cycles a stress-strain curve was obtained on an X-Y recorder and any change in the modulus of elasticity was determined by scaling the X-Y stress-strain plots. The results obtained (Fig. 2) indicate that there was no deterioration of the mortar during the cyclic loading, as judged from the fact that the modulus of elasticity remained practically constant throughout the tests. The 21,000 cycles used represent almost 10 years of load application in the field, assuming that the antenna rotates on the average of six times per day.

D. Long-Term Static Load Tests

Both the oil saturated and untreated (no oil) control specimens were tested for creep characteristics by subjecting them to a sustained compressive stress of 2.8 MPa (4000 psi) (about 40 percent of ultimate strength) for a period of 7 months (210 days). The results obtained on the 7.62 by 15.24 cm (3 by 6 in.) cylindrical specimens are shown in Fig. 3. The data show that oil saturation of the dry-pack mortar has no significant influence on the elastic or creep deformation.

E. Strength of Samples Taken from the Goldstone Antenna

Although all of the results obtained on laboratory prepared samples have indicated that oil-saturation has no significant effect on compressive strength, a visual inspection of the samples removed from the Goldstone antenna clearly indicated some deterioration of the oil soaked mortar, especially near the top of the 7.6 cm (3 in.) thick layer where it is in contact with the steel plate of the hydrostatic bearing runner. Many of these surfaces were relatively soft and had a sandy appearance. This damage to the top layer of the mortar may have been caused by the oil permeating the top layer of the dry-pack mortar at an early age, or by improper tamping when placed.

To evaluate the influence of oil-saturation on the degree of damage to the mortar, compressive strength was determined on a number of samples taken from the Goldstone antenna which had varying degrees of oil saturation. These samples, all representing the top layer of the mortar, were cut into small prismatic specimens having an area of about 0.27 cm^2 (1.7 sq. in.) and a height of about 4.4 cm (1-3/4 in.). The results obtained are summarized in Table 3, and a plot of the compressive strength against degree of saturation is given in Fig. 4. The degree of saturation was determined only by visual inspection by determining the proportion of the sample containing oil. As shown by the data in Fig. 4 the degree of oil saturation has a significant influence on the strength of the mortar. For mortar containing no oil, the strength is about 6.3 – 8.3 MPa (10,000 – 12,000 psi), whereas for the fully oil saturated samples the compressive strength is in the range of only 4.1 – 5.5 MPa (6000 – 8000 psi).

F. Conclusions

Based on the results obtained, it appears that oil saturation of the laboratory prepared specimens does not fully represent the oil-saturated samples obtained from the Goldstone antenna. As was shown in the first series of tests, oil saturation of laboratory prepared specimens had no significant effect on compressive strength or modulus of elasticity. Also, as

shown in this report, oil saturation does not affect the properties of mortars when subjected to cyclic or long-term loads. However, a limited number of compressive strength tests made on samples of the top layer of mortar taken from the Goldstone antenna show a significant loss of strength with increasing degree of oil saturation. This deterioration of the quality of the grout may have been caused by the oil getting into the top layer of the grout at an early age, either during the dry-pack operation or prior to the mortar being sufficiently cured.

Table 1. Properties of dry-pack mortars and concretes containing U.C. laboratory aggregates

Mojave Type II cement; sand, F.M. 2.90; 1/2-in. max. size coarse aggregate
Mix proportion: mortar 1:1.5 (cement:sand), concrete 1:0.8:0.7 (cement:sand:coarse aggregate)

	Non-oil-soaked specimens								Oil-soaked specimens[c]		
Mix	W/C	Compressive[a] strength (28 days)	E[a], psi (28 days)	Drying shrinkage, %[b], days					Compressive[a] strength (28 days)	E, (28 days)	Oil absorption, % by weight
Mortar	0.21	69.6 MPa (10,100 psi)	4.0×10^6	0.012	0.022	0.031	0.038	0.051	77.9 MPa (11,300 psi)	27 GPa (3.9×10^6 psi)	3.2
Gravel concrete	0.22	76.5 MPa (11,100 psi)	4.4×10^6	0.007	0.013	0.017	0.022	0.032	75.1 MPa (10,900 psi)	30 GPa (4.3×10^6 psi)	2.5
Crushed limestone concrete	0.23	80 MPa (11,600)	4.0×10^6	0.005	0.009	0.014	0.019	0.030	77.2 MPa (11,200 psi)	30 GPa (4.3×10^6 psi)	2.8

[a]Average of three 76 X 150 mm (3 by 6-in.) cylinders sealed in plastic to age of test (28 days).

[b]Average of three 3 by 76 X 254 mm (3 by 10-in.) prisms sealed in plastic for 14 days and then exposed to drying at 50 percent relative humidity.

[c]Same size specimens as non-oil-soaked. Specimens sealed for 7 days, then oven-dried and vacuum saturated with ARCO-DURO 700 hydrostatic bearing oil; 1 day vacuum, 5-days oil at 690 kPa (100 psi).

Table 2. Properties of dry-pack mortars and concretes containing Conrock Co. aggregates (San Bernardino)

Washed concrete sand; F.M. 2.82, 3/8-in. max. size gravel
Mix proportions: mortar 1:1.5 (cement:sand), concrete 1:0.75:0.75 (cement:sand:coarse aggregate)

Mix	W/C	Compressive[a] strength (28 days)	E x 10^6,[a] psi (28 days)	1	3	7	14	28	56	Compressive strength (28 days)	E (28 days)	Oil absorption, % by weight
Mojave Type II Portland cement	Mortar 0.20	84.1 MPa (12,200 psi)	4.6	0.007	0.011	0.018	0.024	0.031	0.040	82.0 MPa (11,900 psi)	30 GPa (4.4 x 10^6 psi)	3.8
	Concrete 0.19	72.4 MPa (10,500 psi)	4.3	0.004	0.009	0.015	0.021	0.028	0.036	76.5 MPa (11,100 psi)	28 GPa (4.1 x 10^6 psi)	3.4
Chem-Comp cement	Mortar 0.20	85.5 MPa (12,400 psi)	4.4[c]	+0.011	+0.011	+0.007	+0.002	0.018	0.027	78.6 MPa (11,400 psi)	30 GPa	4.6
			4.4[d]	0.006	0.011	0.019	0.028	0.032	0.041		4.3 x 10^6 psi)	
	Concrete 0.19	70.3 MPa (10,200 psi)	3.9[c]	+0.004	0.000	0.006	0.014	0.024	0.033	68.9 MPa (10,000 psi)	28 GPa (4.1 x 10^6 psi)	4.4
			3.9[d]	0.004	0.009	0.016	0.025	0.030	0.040			

[a]Average of three 76 x 150 mm (3 by 6-in.) cylinders sealed in plastic to age of test (28 days).

[b]Average of three 76 x 254 mm (3 by 10-in.) prisms; average of three 76 x 254 r wall (3 x 10 in.) prisms; sealed in plastic for 14 days and then exposed to drying at 50 percent relative humidity.

[c]Shrinkage values include early age expansion (+ values are expansion).

[d]Values are for drying shrinkage only, not including early age expansion.

[e]Same size specimens as non-oil-soaked. Specimens sealed for 7 days in plastic.

Table 3. Influence of degree of oil saturation on compressive strength of mortar[a] removed from Goldstone antenna

Mortar sample	Specimen No.	Degree of saturation, %	Compressive strength, MPa (psi)
A	1	0	72.4 (10,500)
	2	0	82.0 (11,900)
	3	100	44.1 (6400)
	4	100	54.5 (7900)
B	1	5	105.5 (15,300)
	2	30	78.6 (11,400)
C	1	3	66.2 (9600)
	2	15	64.8 (9400)
D	1	0	90.3 (13,100)
	2	5	88.9 (12,900)
E	1	100	53.1 (7700)
	2	100	51.7 (7500)
	3	100	51.0 (7400)
	4	100	46.2 (6700)
F	1	100	40.7 (5900)
	2	100	34.5 (5000)
G	1	3	72.41 (10,500)
	2	10	71.0 (10,300)
	3	30	68.9 (10,000)
	4	100	44.1 (6400)
	5	100	44.8 (6500)
	6	100	49.6 (6200)
H	1	5	49.0 (7100)
	2	95	36.5 (5300)
I	1	0	76.5 (11,100)
	2	50	63.4 (9200)
J	1	0	62.1 (9000)
	2	30	60.0 (8700)
	3	40	50.3 (7300)
	4	55	54.5 (7900)

[a]Specimens cut from mortar samples. Average area of sample 1100 mm^2 (1.7 $in.^2$) and a height of 34 mm (1-3/4 in.).

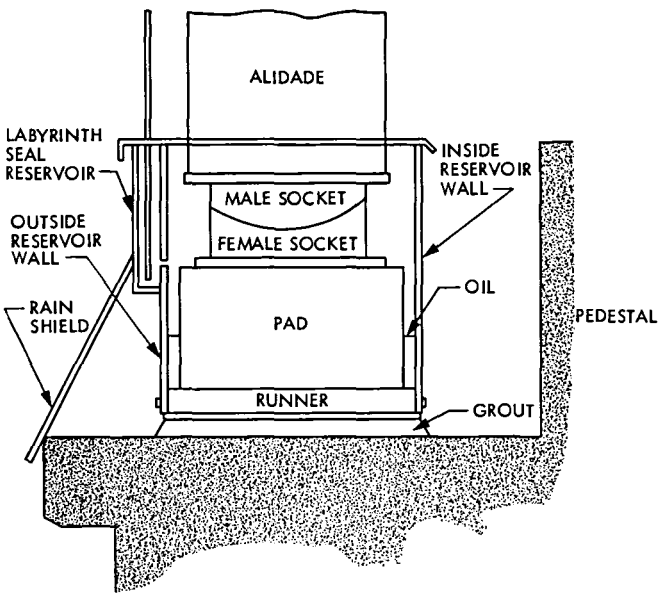

Fig. 1. Cross section of hydrostatic bearing runner and pad

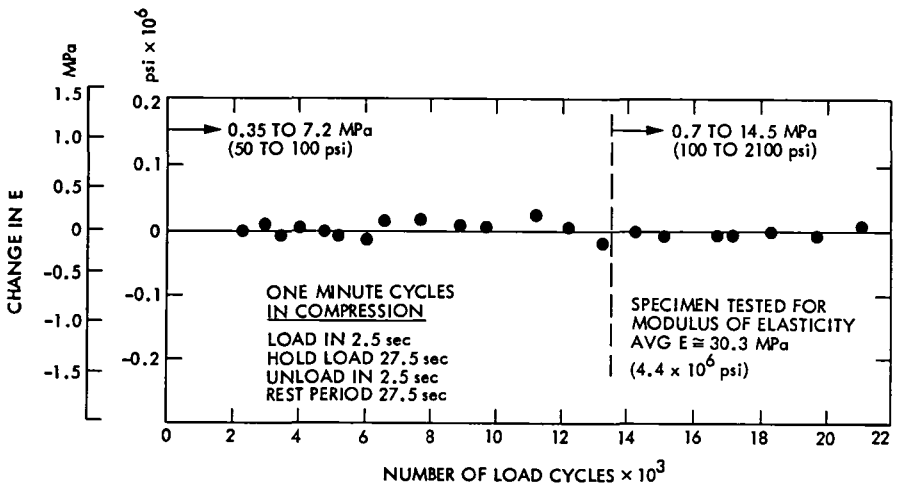

Fig. 2. Effect of cyclic loading of oil-saturated mortar on modulus of elasticity

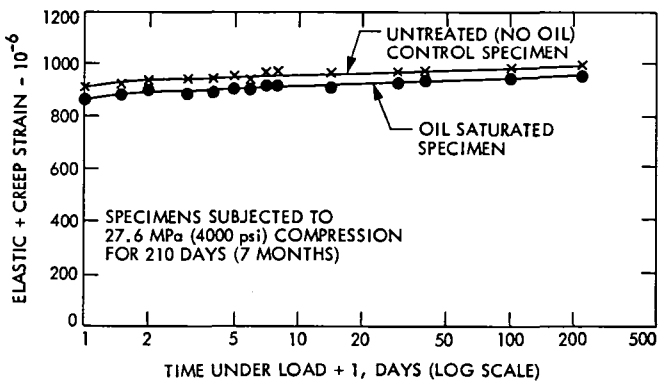

Fig. 3. Effect of long-term static load on creep of oil-saturated and control (no oil) mortars

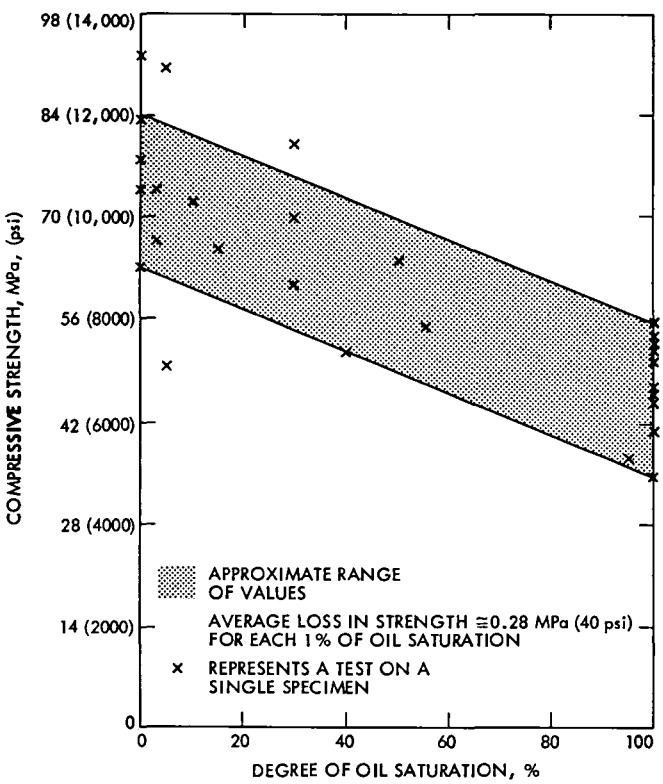

Fig. 4. Influence of oil saturation on compressive strength of mortar removed from the Goldstone antenna

Appendix A

Dry-Pack Mortars and Concretes: Materials and Test Procedures

Given in this Appendix is information on materials, mix proportions, mixing, casting, curing and testing of plain and oil-saturated dry-pack mortars and concretes.

I. Materials and Mix Proportions

The materials and proportions used for the dry-pack mortars and concretes of this test program are summarized in the following tabulations:

Phase I – Mixes Containing Laboratory Aggregates

Mix proportions –

Mortar:	1:1.5 (cement:sand); W/C = 0.21
Concrete:	1:0.8:0.7 (cement:sand:coarse aggregate)
	W/C = 0.22 for gravel mix; 0.23 for limestone mix
Cement –	Type II Portland cement, Mojave brand, California Portland Cement Co.
Sand –	Pleasanton top sand; F.M. 2.90, sp. gravity 2.67, absorption 1.3 percent
Coarse aggregate –	1/2-in. river gravel, Fair Oaks, California; sp. gravity 2.82, absorption 1.1 percent 13 mm crushed limestone, Kaiser sand and gravel Co.; sp. gravity 2.70, absorption 1.1 percent

Phase II – Mixes Containing Conrock Aggregates, San Bernardino, California

Mix proportions –

Mortar:	1:1.5 (cement:sand); W/C = 0.20
Concrete:	1.0.75:0.75 (cement:sand:coarse aggregate) W/C = 0.19
Cements –	Type II Portland Cement, Mojave brand, California Portland Cement Co.; and Chemcomp Cement, Southwestern Cement Co.
Sand –	Conrock Co., washed concrete sand; F.M. 2.87, sp. gravity 2.66, absorption 1.2 percent
Coarse aggregate –	3/8-in. gravel, Conrock Co., San Bernardino, California; sp. gravity 2.66, absorption 1.3 percent
Water –	Chilled with ice chips to 2.7 ± 1.7°C (37 ± 3°F)

The water/cement ratios used were selected to produce mortars or concretes suitable for a dry-pack application as judged during the manufacture of the specimens. A rubbery behavior during dry packing indicated an excessive amount of water and a tendency to crumble an insufficient amount of water.

II. Mixing and Casting Procedures

The mixing of the Phase I mortars and concretes was done in a pan-type mixer of 14 dm^3 (1/2-cu ft) capacity. Any lumps formed during the mixing operation were broken up by passing the freshly mixed dry-pack materials through a screen having an opening one size greater than the minimum size aggregate. The mixing of the Phase II mortars and concretes was done in a laboratory-size Hobart bowl type mixer (ASTM C 305). The use of this type mixer prevented the formation of lumps.

The casting of the specimen 7.6 X 150 mm (3 by 6 in.) cylinders and 7.6 X 25 mm (3 by 10 in.) prisms was done in 38 mm (1.5 in.) layers, each layer being compacted with a laboratory-size pneumatic sand tamper equipped with a 38 mm (1.5 in.) diameter tamping head. The tamper was operated at an air pressure of 345 kPa (50 psi). The duration of compaction of each 40 mm (1.5 in.) layer was 30 s for the cylinders and 120 s for the prisms. To ensure uniformity of compaction of the test samples, all specimens were cast with an extra 40 mm (1.5 in.) layer on top (using mold extension) which was cut off immediately after completion of casting.

III. Curing, Oil Saturation, and Testing Strength of Specimens

The curing conditions and test schedule for the non-oil-soaked (control) and oil-soaked 76 X 150 mm (3 X 6 in.) specimens used to determine compressive strength and modulus of elasticity are summarized in the following tabulations:

Non-oil-soaked specimens (control)	Total time, days
7 days in mold; sealed with plastic to prevent moisture loss; demolded at age 7-days	0-7
7 days sealed in plastic	7-14
1 day drying in 230°F oven	14-15
6 days storage at 50% relative humidity	15-21
Test at age 21 days for compressive strength and modulus of elasticity	21
Oil soaked specimens	
Same as for non-oil-soaked controls	0-15
Same as for non-oil-soaked controls	0-15
Same as for non-oil-soaked controls	0-15
Vacuum saturation with oil, 6-days	15-21
Test at age 21 days for compressive strength and modulus of elasticity	21

The oil used for saturation of the mortar or concrete specimens was ARCO-DURO 700 hydrostatic oil, which is the same type of oil used for the antenna bearings. The procedure used in vacuum-saturating the dry-pack mortar or concrete specimens with oil consisted of subjecting them first to a vacuum of 710 mm (28 in.) mercury for 24 hours; then while maintaining this vacuum the saturation chamber was filled with oil, and after shutting off the vacuum a pressure was applied to the oil and maintained for 5 days. The oil pressure used for the Phase I specimens was 690 kPa (100 psi) and for the Phase II specimens 896 kPa (130 psi). The amount of oil absorbed by the test samples was determined from the weight of the specimens before and after oil saturation and expressed as a percentage of the oven-dry weight.

The compressive strength tests on all of the 76 X 150 mm (3 by 6 in.) mortar and concrete specimens were performed in accordance with ASTM C 39 method of test, "Compressive Strength of Cylindrical Concrete Specimens." The procedure used for determining the modulus of elasticity was based on ASTM C 469, "Static Modulus of Elasticity and Poisson's Ratio of Concrete in Compression." The longitudinal deformations of the test specimens during the compression strength test were measured by two linear variable differential transformers (LVDT's).

IV. Curing and Testing of Drying Shrinkage Specimens

The 76 X 254 mm (3 by 10 in.) drying shrinkage prisms remained in their molds and were sealed in plastic for 7 days; then after demolding they were resealed in plastic to prevent moisture loss and remained sealed for an additional 7 days. At age 14 days the seal was removed and the specimens exposed to air maintained at 50 percent relative humidity. Measurements of drying shrinkage were made using a vertical dial gage comparator after 1, 3, 7, 14, and 28 days exposure to the dry 50 percent relative humidity. The drying shrinkage was expressed as a percentage length change.

Voyager 1979: Update to the Radial and Solar Cycle Variations in the Solar Wind Phase Fluctuation Spectral Index

A. L. Berman and A. D. Conteas
TDA Engineering Office

Of current interest is the value of, and possible variations in, the solar wind phase fluctuation spectral index. This article presents columnar spectral index information that has been extracted from a sizable volume of Voyager 1979 solar conjunction Doppler phase fluctuation data. The Voyager 1979 results, when compared to similar information derived from the 1976 Helios and Viking and 1978 Voyager solar conjunctions, lead to the following inferences: (1) there has been a significant change in the spectral index from 1976 to 1978/1979; (2) there is continuing evidence that favors a slight (positive) correlation between the spectral index and the solar (sunspot) cycle; (3) there is little or no evidence in support of a radial variation of the spectral index. Recently, it has been hypothesized that a flattening of the phase fluctuation spectrum occurs near the sun ($\lesssim 20r_{\odot}$); these data are at a variance with such a hypothesis.

I. Introduction

Of current interest are the possible variations in the solar wind phase fluctuation spectral index ($=K_0$, where the columnar phase spectral density variation with fluctuation frequency ν is ν^{-K_0}) with parameters such as radial distance, solar cycle, and fluctuation frequency regime. In a previous report (Ref. 1), the authors analyzed the parametric dependencies of the solar wind phase fluctuation spectral index as extracted from the solar conjunction Doppler data of the Helios (1976), Viking (1976), and Voyager (1978) spacecraft. Reference 1 found no evidence of a spectral index radial variation, and only inconclusive evidence pointing to a possible slight variation with solar cycle.

This article augments the previous spectral index data base with new information obtained from Voyager 1 Doppler data generated during the 1979 solar conjunction. These new data tend to confirm the results of Ref. 1. In addition, a hypothesized flattening of the phase fluctuation spectrum at close solar distances ($\lesssim 20r_{\odot}$, where $r_{\odot}$ = solar radius), currently in favor as, for instance, in Woo and Armstrong (Ref. 2) and Esposito et al. (Ref. 3), is not observed in these data.

II. Helios and Viking Spectral Index Data During 1976

Berman (Refs. 4 and 5) has analyzed a large volume of Doppler phase fluctuation data generated by the Deep Space Network (DSN) during the 1976 solar conjunctions of Helios and Viking. Analysis of the spectral index information derived from the Helios and Viking data yielded (Ref. 5) a mean value

of 2.42 for the columnar (two-dimensional) spectral index and provided no indication of a spectral index radial dependence.

Figure 1 (from Ref. 5) presents the columnar spectral index, as computed from Viking Doppler phase fluctuation data, versus Sun-Earth-probe (SEP) angle. The absence of any significant spectral index radial dependence is obvious from inspection of Fig. 1.

III. Voyager Spectral Index Data During 1978

Doppler phase fluctuation data generated by the DSN during the 1978 Voyager solar conjunction were analyzed by the authors in Ref. 1. These data yielded a mean value of 2.67 for the columnar spectral index and provided little or no indication of a spectral index radial dependence.

Figure 2 (from Ref. 1) presents the spectral index, as computed from Voyager Doppler phase fluctuation data, versus Sun-Earth-probe (SEP) angle. Again, the absence of any significant spectral index radial dependence is obvious from inspection of Fig. 2.

IV. Voyager Spectral Index Data During 1979

In 1977, the DSN implemented a new capability to allow the convenient extraction of spectral index information from Doppler phase fluctuation data; this capability is described in detail in Refs. 5 and 6. Using this new capability, columnar spectral index information has been computed from the 1979 Voyager 1 Doppler phase fluctuation data. Very briefly, the spectral index extraction process is predicated on the following relationships (Ref. 6):

$$\phi^2(\nu) \propto \nu^{-K_0+1}$$

$$\nu \propto \tau_a^{-1}$$

$$\phi(\tau_a) \propto \tau_a \cdot \sigma_f(\tau_a)$$

where

ϕ = RMS Doppler phase fluctuation

τ_a = Doppler averaging time (sample interval)

σ_f = RMS Doppler frequency fluctuation

ν = fluctuation frequency

K_0 = columnar spectral index

The Voyager 1 two-way S-band Doppler phase fluctuation data were analyzed during the period July 24, 1979 to September 22, 1979. During this period, the SEP varied between 1.3 degrees and 22.2 degrees. The approximate fluctuation frequency (ν) range for which the columnar spectral index was computed for the Voyager 1 data was:

$$2.8 \times 10^{-4}\ \text{Hz} < \nu < 2.8 \times 10^{-3}\ \text{Hz}$$

The spectral index information determined from the Voyager 1 Doppler phase fluctuation data is presented in Figs. 3 and 4. Figure 3 presents the spectral index vs day of year (DOY), while Fig. 4 presents the spectral index vs SEP.

The mean value of the spectral index as computed from the Voyager 1 1979 Doppler data is $K_0 = 2.60$. Again, inspection of Fig. 4 indicates no significant spectral index radial dependence. In Fig. 5, all Viking 1976, Voyager 1978, and Voyager 1979 data have been plotted as a function of signal path closest approach distance. Although a casual look at Fig. 5 might leave the impression of a spectral index radial dependence, what is really in evidence is a significant steepening of the spectral index between solar cycle minimum data (1976) and solar cycle maximum data (1978-1979), in combination with different spans of data closest approach distance.

V. Spectral Index Variations With Solar Cycle

Reference 1 inferred a possible slight variation of the spectral index with solar cycle. What trends exist point to a positive correlation with solar cycle; i.e., the fluctuation spectrum appears to be *steeper* during solar cycle (sunspot) maximum. In this regard, the Voyager 1979 data are consistent with earlier results presented in Ref. 1.

Table 1 presents the results of ten experimental determinations of the spectral index during Solar Cycles 20 and 21. The mean value of the ten experiments listed in Table 1 is $K_0 = 2.50$ and the standard deviation is $1\sigma = 0.13$. It is, therefore, suggested that a mean model for the solar wind phase fluctuation spectrum (P_ϕ) be adopted as follows:

$$P_\phi(\nu) \propto \nu^{-2.5 \pm 0.2}$$

where the spectrum is more likely to be *flatter* during solar cycle minimum and *steeper* during solar cycle maximum.

In Fig. 6, the various spectral index determinations have been plotted as a function of solar cycle. As already noted, there appears to be a slight steepening of the spectral index

with solar cycle maximum; however, it is clear that a much greater volume of data will be required before any solar cycle dependence can be claimed with certainty.

VI. Radial Variations in the Spectral Index

Many investigators have claimed a radial variation in the spectral index; examples are Woo and Armstrong (Ref. 2), Esposito et al. (Ref. 3), and Coles et al. (Ref. 7). In particular, Woo and Armstrong claim that at approximately $20r_{\odot}$, the phase fluctuation columnar spectral index changes from approximately 2.65 ($\gtrsim 20r_{\odot}$) to approximately 2.1 ($\lesssim 20r_{\odot}$). Review of the data in Figs. 1, 2, and 4 does not provide any evidence of such a flattening of the near-Sun phase fluctuation spectrum.

Of course, the results derived from closed-loop Doppler data presented here are very low frequency (2.8×10^{-4} Hz $< \nu <$ 2.8×10^{-2} Hz) and it is conceivable that such a flattening exists in a different fluctuation frequency regime; nonetheless, the claims of near-Sun spectrum flattening can be considered as speculative at this time.

VII. Summary and Discussion

A new DSN capability has been utilized to obtain a sizeable volume of spectral index information during the Voyager 1979 solar conjunction. Major conclusions derived from a comparative study of these data with similar data obtained during 1976 solar conjunctions of Helios and Viking and the 1978 solar conjunction of Voyager are:

(1) There has been a significant change in the spectral index from solar cycle minimum (1976; $K_0 = 2.42$) to (near) solar cycle maximum (1978/1979; $K_0 = 2.64$).

(2) There continues to be evidence for a slight (positive) correlation between spectral index and solar (sunspot) cycle.

(3) There continues to be little or no evidence for a significant variation of spectral index with radial distance. In particular, there is no evidence to support a currently hypothesized near-Sun phase fluctuation spectrum flattening.

The exercise of this new DSN capability is expected to be continued in future years to derive columnar spectral index information from Voyager solar conjunction Doppler phase fluctuation data, and hence to allow the continued monitoring of spectral index variations during the remainder of Solar Cycle 21.

References

1. Berman, A. L., and Conteas, A. D., "Radial and Solar Cycle Variations in the Solar Wind Phase Fluctuation Spectral Index as Determined From Voyager 1978 Solar Conjunction Data," in *The Deep Space Network Progress Report 42-48*, Jet Propulsion Laboratory, Pasadena, Calif., Dec. 15, 1978.

2. Woo, R., and Armstrong, J. W., "Spacecraft Radio Scattering Observations of the Power Spectrum of Electron Density Fluctuations in the Solar Wind," *Journal of Geophysical Research* (in press).

3. Esposito, P. B., et al., "Helios Data Analysis Results," EM 315-90, Aug. 22, 1979 (JPL Internal Document).

4. Berman, A. L., "A Comprehensive Two-Way Doppler Noise Model for Near-Real-Time Validation of Doppler Data," in *The Deep Space Network Progress Report 42-37*, Jet Propulsion Laboratory, Pasadena, Calif., Feb. 15, 1977.

5. Berman, A. L., "Phase Fluctuation Spectra: New Radio Science Information to Become Available in the DSN Tracking System Mark III-77," in *The Deep Space Network Progress Report 42-40*, Jet Propulsion Laboratory, Pasadena, Calif., Aug. 15, 1977.

6. Berman, A. L., and Conteas, A. D., "A Solar Wind Turbulence Event During the Voyager 1978 Solar Conjunction Profiled via a New DSN Radio Science Capability," in *The Deep Space Network Progress Report 42-48*, Jet Propulsion Laboratory, Pasadena, Calif., Dec. 15, 1978.

7. Coles, W. A., Rickett, B. J., and Scott, S. L., "Scintillation Observations Near the Sun," in *A Close-up of the Sun*, edited by Neugebauer, M., and Davies, R. W., JPL Publication 78-70, Jet Propulsion Laboratory, Pasadena, Calif., Sept. 1, 1978.

8. Chang, H., *Analysis of Dual-Frequency Observations of Interplanetary Scintillations Taken by the Pioneer 9 Spacecraft*, Doctoral Dissertation, Department of Electrical Engineering, Stanford University, May 1976.

9. Woo, R., Yang, F., Yip, W. K., and Kendall, W. B., "Measurements of Large Scale Density Fluctuations in the Solar Wind Using Dual Frequency Phase Scintillations," *The Astrophysical Journal*, Vol. 210, No. 2, Part 1, Dec. 1, 1976.

10. Unti, T. W. J., Neugebauer, M., and Goldstein, B. E., "Direct Measurements of Solar Wind Fluctuations Between 0.0048 and 13.3 Hz," *The Astrophysical Journal*, Vol. 180, March 1, 1973.

11. Goldstein, B., and Sisco, G. L., "Spectra and Cross Spectra of Solar Wind Parameters from Mariner 5," in *Solar Wind*, edited by Sonett, C. P., Coleman, P. J., Jr., and Wilcox, J. M., National Aeronautics and Space Administration, Washington, D. C., 1972.

12. Intriligator, D. S., and Wolfe, J. H., "Preliminary Power Spectra of the Interplanetary Plasma," *The Astrophysical Journal, Letters*, Vol. 162, Dec. 1970.

Table 1. Solar wind columnar phase fluctuation spectral index measurements

Source	Year	K_0	Type of measurement	Reference
Berman	1979	2.60	Voyager Doppler Phase Fluctuation	
Berman	1978	2.67	Voyager Doppler Phase Fluctuation	1
Woo	1976/ 1977	2.65	Viking Doppler Spectra	2
Berman	1976	2.41	Viking Doppler Phase Fluctuation	4
Berman	1976	2.43	Helios Doppler Phase Fluctuation	4
Chang	1972/ 1975	2.5	Pioneer 9 Intensity Scintillation	8
Woo	1974	2.55	Mariner Venus Mercury Dual-Frequency Doppler	9
Unti	1968	2.55	OGO 5 in-situ	10
Goldstein	1967	2.3	Mariner Mars in-situ	11
Intriligator	1965	2.3	Pioneer in-situ	12

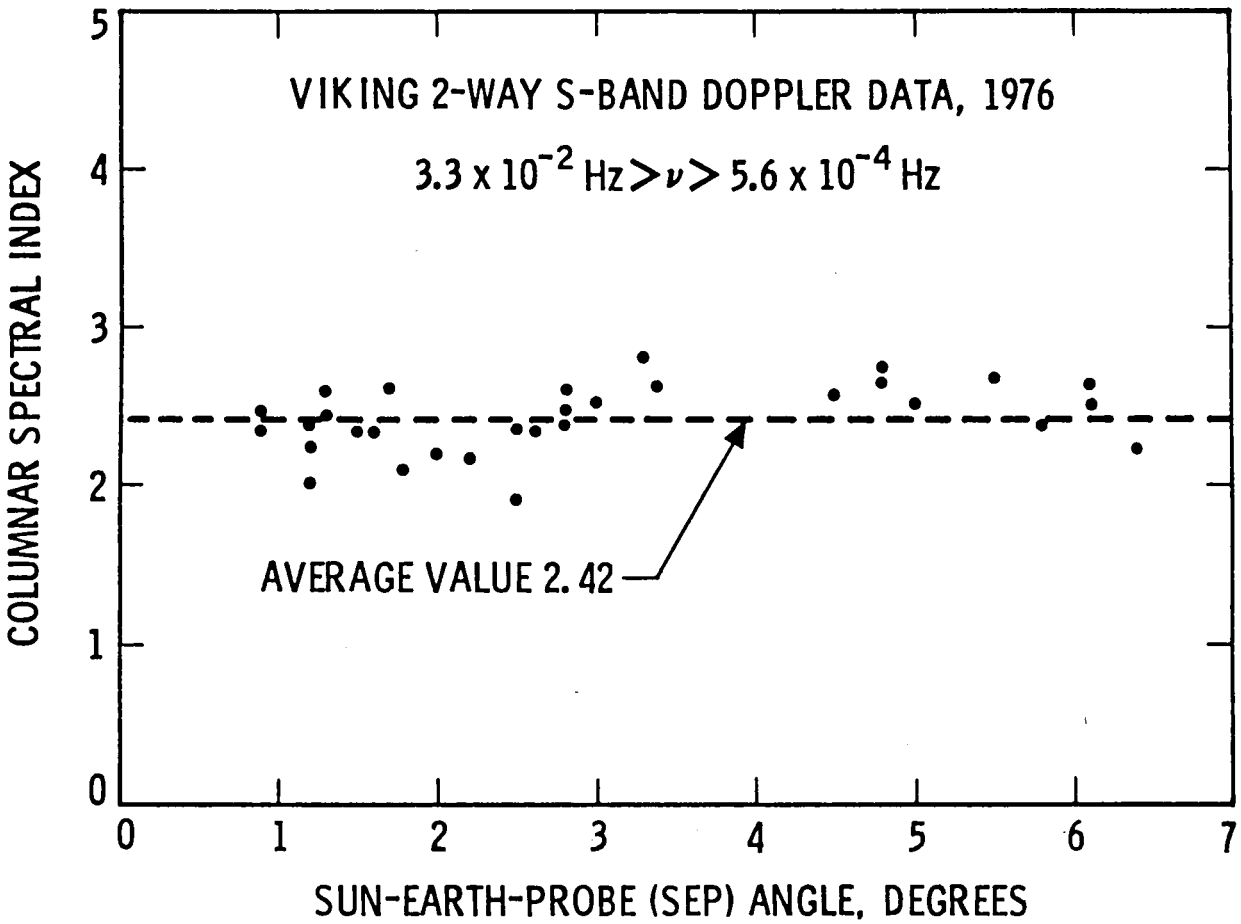

Fig. 1. Columnar solar wind phase fluctuation spectral index versus Sun-Earth-probe angle, 1976

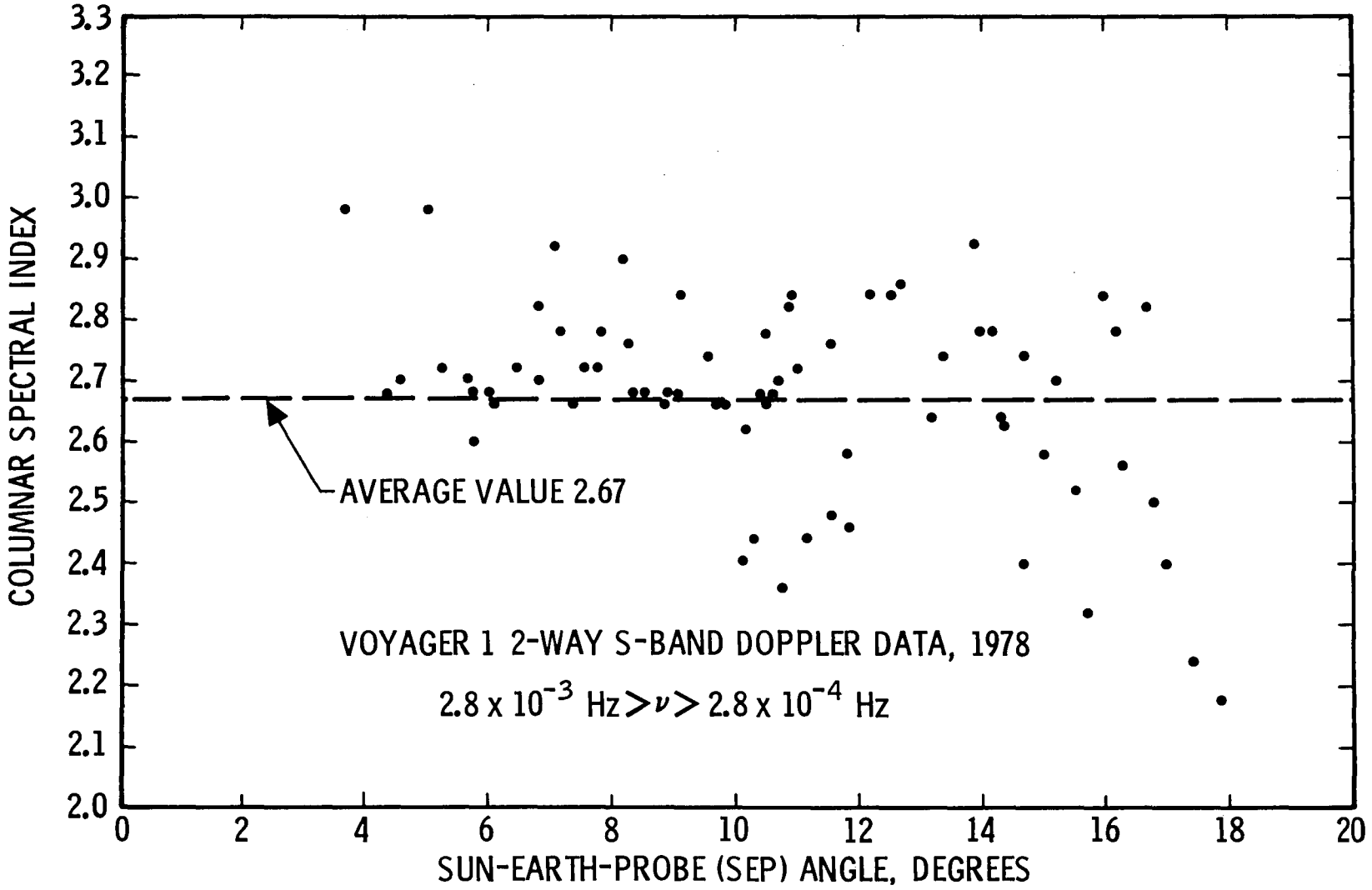

Fig. 2. Columnar solar wind phase fluctuation spectral index versus Sun-Earth-probe angle, 1978

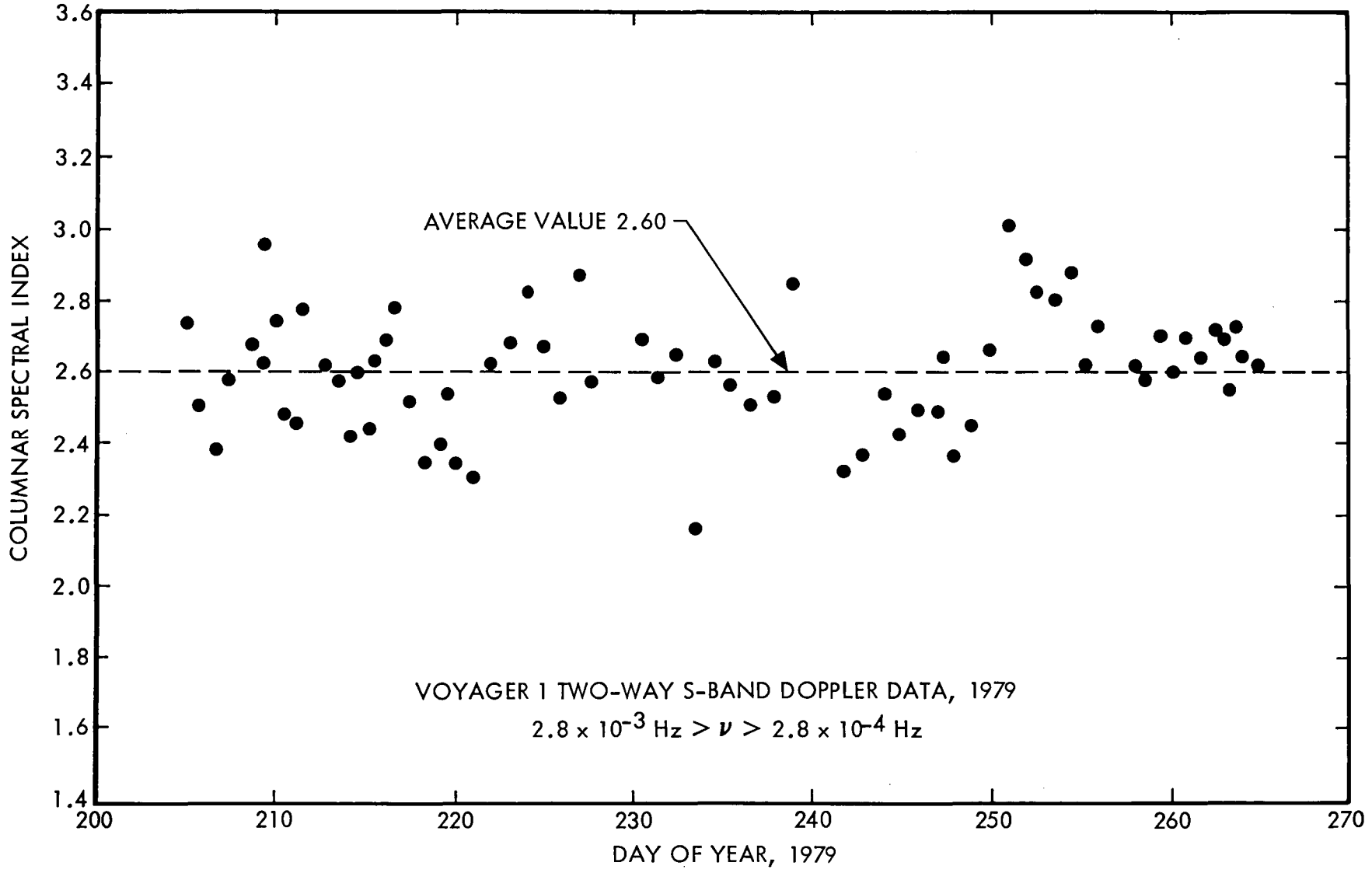

Fig. 3. Columnar solar wind phase fluctuation spectral index versus day of year, 1979

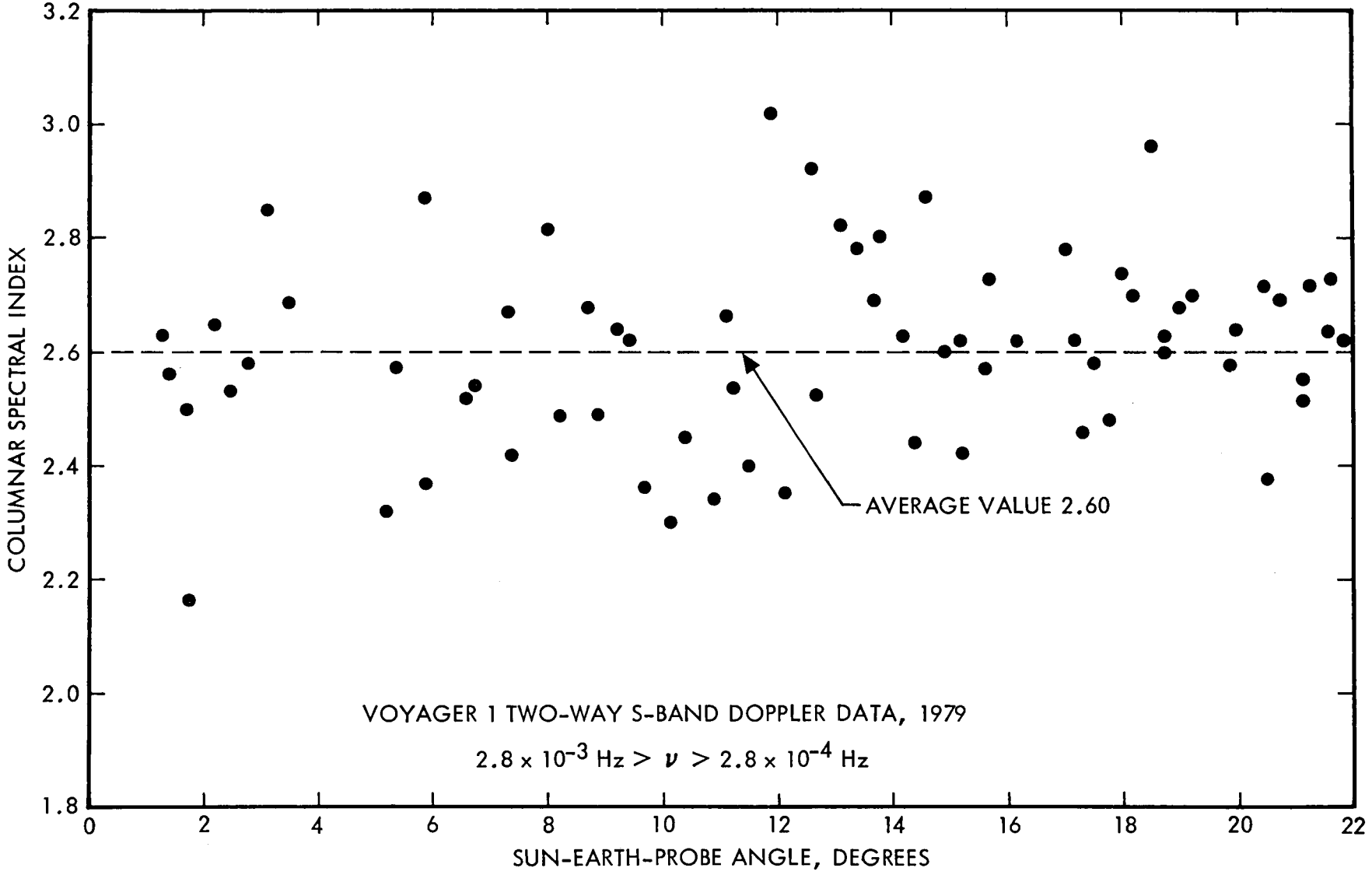

Fig. 4. Columnar solar wind phase fluctuation spectral index versus Sun-Earth-probe angle, 1979

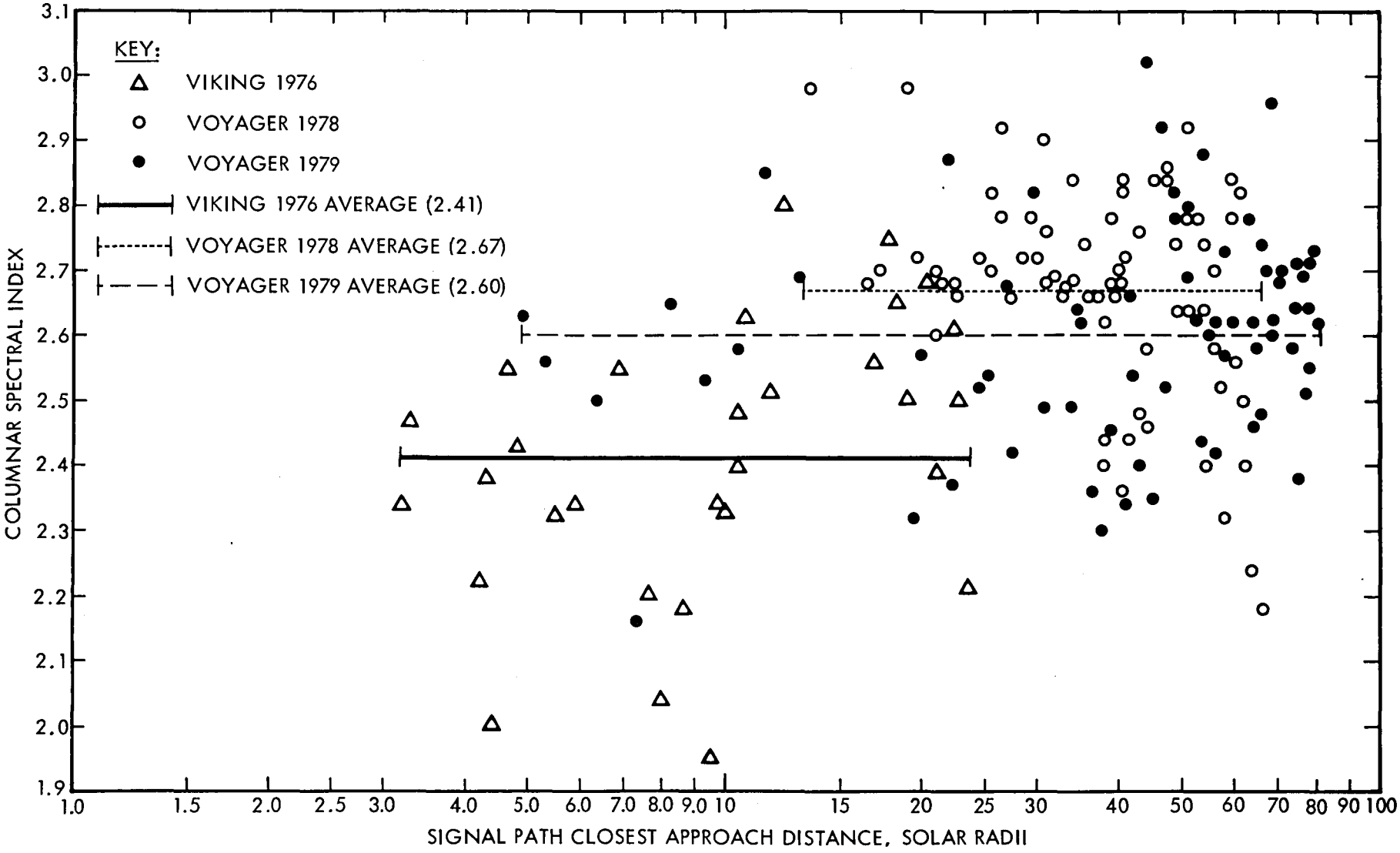

Fig. 5. Columnar solar wind phase fluctuation spectral index versus signal path closest approach distance

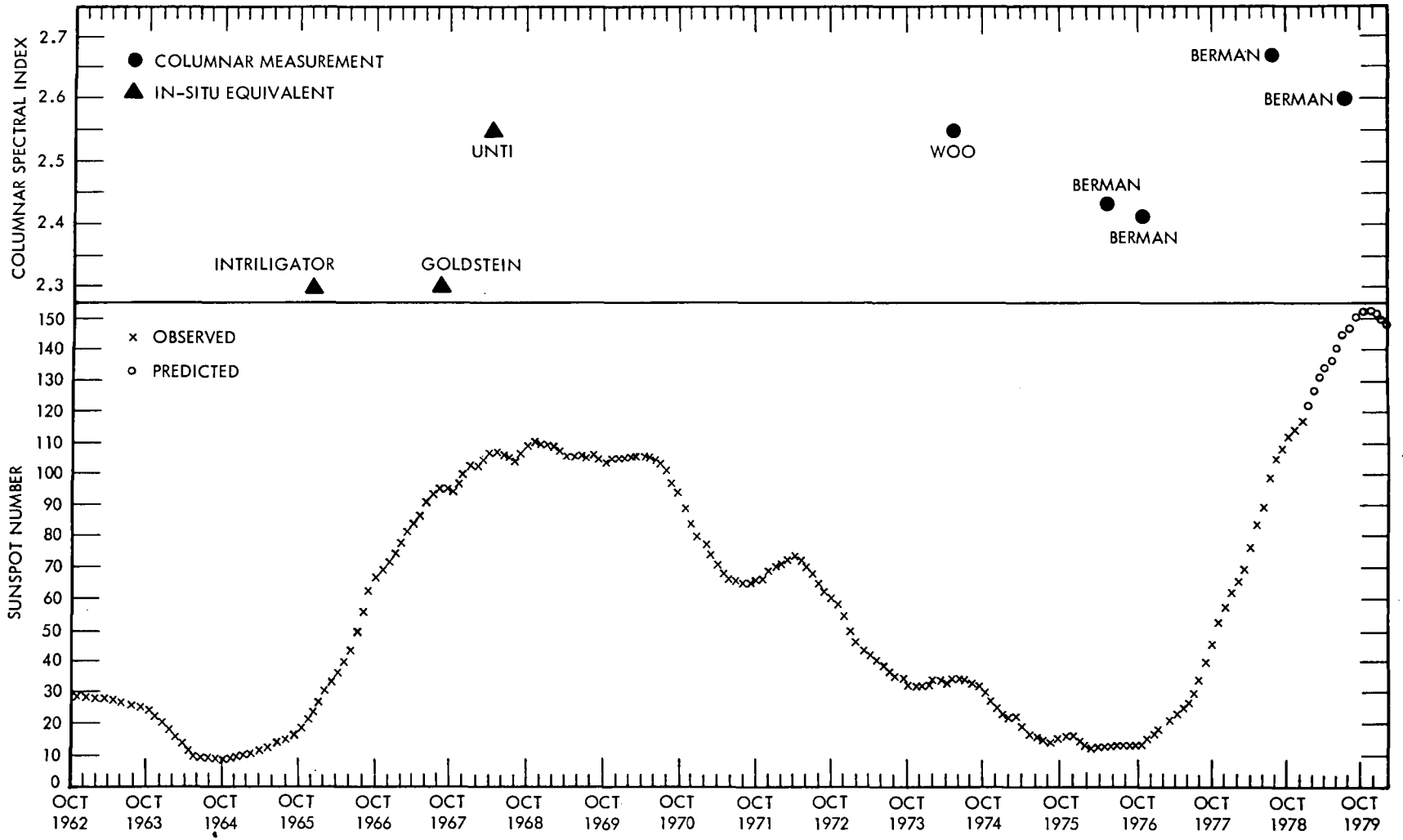

Fig. 6. Columnar solar wind phase fluctuation spectral index versus solar (sunspot) cycle

An Efficient Program for Decoding the (255,223) Reed-Solomon Code Over *GF* (2^8) With Both Errors and Erasures, Using Transform Decoding

R. L. Miller and T. K. Truong
Communications Systems Research Section

I. S. Reed
University of Southern California

To decode a (255,223) Reed-Solomon code over GF(2^8), a fast Fourier-like transform over GF(2^8) has been developed to compute the syndromes and the error-erasure vectors of the transmitted code words. This new simplified transform decoder is implemented in a program on a digital computer. The (255,223) Reed-Solomon code over GF(2^8) is a NASA standard for concatenation with a convolutional code. In a simulation, random code words were corrupted by random error and erasure patterns, and decoded whenever theoretically possible. A matrix of execution times for this new transform decoder under varying sets of errors and erasure patterns is included in the paper. This matrix demonstrates that the speed of the new decoder is between 3 and 7 times faster than the standard R-S decoder, developed previously by NASA.

I. Introduction

Recently the authors developed (Ref. 2) a simplified algorithm for correcting erasures and errors of Reed-Solomon (R-S) codes over the finite field $GF(p^m)$, where p is a prime and m is an integer. For a space communication application it was shown (Ref. 3) that a 16-error-correcting R-S code of 255 eight-bit symbols, concatenated with a $k = 7$, rate = 1/2 or 1/3, Viterbi decoded convolutional code, can be used to reduce the signal-to-noise ratio required to meet a specified bit-error rate. Such a concatenated code is being considered for the Galileo project and the NASA End-to-End Data System.

In a concatenated code, the inner convolutional decoder is sometimes able to find only two or more equally probable symbols. For such a case, the best policy is to declare an erasure of the symbol. If the outer R-S code is able to utilize the additional information that certain erasures have occurred, then clearly the system performance will be enhanced.

The algorithm given in Ref. 2 is used here to correct patterns of t errors and s erasures of the words of the (255,223) R-S code, where $2t + s < 33$ and where the symbols belong to the finite field $GF(2^8)$. Define the following five vectors:

$(c_0, c_1, \ldots, c_{254})$ = **c**, code vector

$(r_0, r_1, \ldots, r_{254})$ = **r**, received vector

$(\mu_0, \mu_1, \ldots, \mu_{254})$ = μ, erasure vector

$(e_0, e_1, \ldots, e_{254})$ = **e**, error vector

$(\mu_0, \mu_1, \ldots, \mu_{254})$ = $\tilde{\mu}$, new erasure vector

These vectors are related by $\mathbf{r} = \mathbf{c} + \mu + \mathbf{e}$ and $\tilde{\mu} = \mathbf{e} + \mu$.

Suppose that t errors and s erasures occur in the received vector $\mathbf{r}$ of 255 symbols, and assume $2t + s < 33$. Then, following the algorithm in Ref. 2, the decoding procedure consists of these five steps:

(1) Compute the syndromes $S_k (1 \leqslant k \leqslant 32)$ of the received 255-tuple $(r_0, r_1, \ldots, r_{254})$, i.e.,

$$S_k = \sum_{i=0}^{254} r_i \alpha^{ik} \text{ for } k = 1, 2, \ldots, 32 \qquad (1)$$

where α is an element of order 255 in $GF(2^8)$. If $S_k = 0$ for $1 \leqslant k \leqslant 32$, then $\mathbf{r}$ is a code word and no further decoding is necessary. Otherwise,

(2) Compute τ_j for $j = 0,1,2, \ldots, s$ from the erasure locator polynomial

$$\tau(x) = \prod_{j=1}^{s} (x - Z_j) = \sum_{j=1}^{s} (-1)^j \tau_j x^{s-j} \qquad (2)$$

where s is the number of erasures in the received vector, and $Z_j (1 \leqslant j \leqslant s)$ are the known erasure locations. Next compute the Forney syndromes T_i for $1 \leqslant i \leqslant 32 - s$ from the equation

$$T_i = \sum_{j=0}^{s} (-1)^j \tau_j S_{i+s-j} \text{ for } 1 \leqslant i \leqslant 32 - s \qquad (3)$$

where $\tau_j (1 \leqslant j \leqslant s)$ and $S_j (1 \leqslant j \leqslant 32)$ are known.

(3) If $0 \leqslant s < 32$, then use continued fractions (see Ref. 4) to determine the error locator polynomial $\sigma(x)$ from the known T_i's $(1 \leqslant i < 32 - s)$. For the special case $s = 32$, it was shown (Refs. 4, 5) that it is impossible for any decoder to tell whether there are zero or more additional errors. Thus, for $s = 32$, the best policy is not to decode the message at all.

(4) Compute the combined erasure and error locator polynomial from the equation

$$\tilde{\tau}(x) = \sigma(x)\tau(x) = \sum_{k=0}^{s+t} (-1)^k \tilde{\tau}_k x^{s+t-k} \qquad (4)$$

where $\sigma(x)$ and $\tau(x)$ are now known. Then compute the rest of the transform of the erasure and error vector from the equation

$$S_l = \sum_{k=1}^{s+t} (-1)^k \tilde{\tau}_k S_{l-k} \text{ for } l > 32.$$

Note that $S_{255} = S_0$.

(5) Compute the inverse transform of the syndrome vector $(S_0, S_1, \ldots, S_{254})$ to obtain the error-erasure vector. That is, calculate

$$\tilde{\mu}_i = e_i + \mu_i = \sum_{k=0}^{254} S_k \alpha^{-ik} \text{ for } i = 0, 1, 2, \ldots, 254 \qquad (5)$$

Finally, subtract the error-erasure vector $\tilde{\mu}$ from the received vector to correct it.

Previously the authors (Ref. 1) implemented the above decoding procedure on the UNIVAC 1108 computer. The disadvantage of this decoding program was that the syndromes in Step 1 were computed directly instead of using FFT-like techniques. Also, the slower Chien-type search was used to find the roots of the error polynomial instead of Steps (4) and (5), above. Finally, another direct inverse transform of the syndrome vector points was used to obtain the error and erasure magnitudes.

It was shown (Ref. 6) that a combination of the Chinese remainder theorem and Winograd's algorithm (Refs. 7 and 8) could be used to develop a fast algorithm for computing the syndromes needed for decoding an R-S or BCH code. Such a method requires only a small fraction of the number of multiplications and additions that are required in a direct computation. More generally, it was shown also in Ref. 9 that a modification of Winograd's method could be used to compute $(2^m - 1)$-point transforms over $GF(2^m)$, where $m = 4,5,6,8$.

In this article, the methods developed in Refs. 6 and 9 are applied to compute the syndromes in Step 1 and the error-erasure vector discussed in Step 5. An important advantage of this new transform decoder over the previous methods (Refs. 1 and 10) is that the complexity of the syndrome calculation is substantially reduced. Furthermore, the Chien-type search (Ref. 8) for the roots of the error locator polynomial is completely eliminated. These are replaced by the computation of a 255-point transform using FTT-like techniques. The result is a simpler and faster decoder than can be obtained by conventional means.

The simplified transform decoder was written in FORTRAN V and was implemented on the UNIVAC 1108 computer. The matrix of decoding times for correcting errors and erasures of the (255,223) in this simplified decoder is given in

Table 1. Also, the matrix of decoding times of the conventional algorithm, described in Ref. 1, is provided in Table 2. A comparison of Tables 1 and 2 shows that the new algorithm is faster by a factor of from 3 to 7.

II. A Fast Technique for Computing the Error and Erasure Magnitudes

The computation of the error-erasure vector in Step 5 of the transform decoder is based on the methods in Refs. 8 and 9. The key idea is the use of FFT-like techniques over the the finite field $GF(2^8)$. These concepts are used to compute efficiently the expression

$$A_j = \sum_{i=0}^{255-1} a_i \alpha^{ij} \text{ for } 0 \leqslant j \leqslant 254 \qquad (6)$$

where α is an element of order 255 in $GF(2^8)$. To begin with, since $n = 255 = 3 \times 5 \times 17$, by Refs. 7 and 8, (6) can be decomposed into the following 3 stages:

Stage 1

$$A^1_{(i_1, i_2, j_3)} = \sum_{i_3=0}^{3-1} a_{(i_1, i_2, i_3)} \alpha_3^{i_3 j_3} \text{ for } 0 \leqslant j_3 \leqslant 2$$

Stage 2

$$A^2_{(i_1, j_2, j_3)} = \sum_{i_2=0}^{5-1} A^1_{(i_1, i_2, j_3)} \alpha_2^{i_2 j_2} \text{ for } 0 \leqslant j_2 \leqslant 4$$

Stage 3

$$S_{(j_1, j_2, j_3)} = \sum_{i_1=0}^{17-1} A^2_{(i_1, j_2, j_3)} \alpha_1^{i_1 j_1} \text{ for } 0 \leqslant j_1 \leqslant 16 \qquad (7)$$

where $\alpha_3 = \alpha^{85}$, $\alpha_2 = \alpha^{51}$, and $\alpha_1 = \alpha^{120}$. In (7), Stage 1, Stage 2, and Stage 3 are 3-, 5-, and 17-point transforms, respectively. The detailed algorithms for computing the 3-, 5-, and 17-point transform over $GF(2^8)$ are reproduced in the appendix. It follows from these algorithms that the number of multiplications needed to compute a 3-, 5-, and 17-point transform is 1, 5, and 53, respectively. In similar fashion, it can be shown that the number of additions needed to compute a 3-, 5-, and 17-point transform is 5, 17, and 173, respectively. Thus, the total number of multiplications and additions needed to compute the A_j for $0 \leqslant j \leqslant 254$ is $17 \times 5 \times 1 + 17 \times 5 \times 3 + 53 \times 5 \times 3 = 1135$ and $17 \times 5 \times 5 + 17 \times 5 \times 17 + 173 \times 5 \times 3 = 4465$, respectively. In contrast, using a Chien-type search algorithm, $254(s + t)$ multiplications and $254(s + t)$ additions are required for a direct computation of the inverse transform at the $s + t$ points corresponding to the s erasure locations and the t error locations.

III. Program Design and Implementation

The decoding procedure described in the previous section was implemented on the UNIVAC 1108 computer using FORTRAN V. This program is used to correct any combination of t errors and s erasures occurring in a 255-symbol R-S code word, where $2t + s < 33$. The overall basic structure of the program is given in Fig. 1. It is divided into a main program and five major subroutines.

The Main Program. This is the main driver of the rest of the program. It initializes the decoding process and keeps track of the elapsed CPU time.

Input. This subroutine generates a random code vector (polynomial) $R(x)$ for the R-S decoder and then adds errors and erasures $E(x)$ to it.

Step 1. The first 32 syndromes of the received vectors as well as the corrected vectors are calculated in this subroutine using a combination of the Chinese remainder theorem and Winograd's algorithm as described in Ref. 5. In case the corrected received word is not an R-S code word, the subroutine will output the message, "The corrected received vector is not a codeword." This helps to confirm the correctness of the program, as well as to indicate that the number of errors and erasures have exceeded the limits allowable by the decoder.

Step 2. This subroutine computes the Forney syndrome vector **T** (Eq. 3) from the erasure vector **Z**. The erasure locator polynomial $\tau(x)$ (Eq. 2) is also calculated in this step.

Step 3. The error locator polynomial $\sigma(x)$ is calculated from the Forney syndrome vector **T** using the continued fraction algorithm. The product of the error locator polynomial $\sigma(x)$ and the erasure locator polynomial $\tau(x)$ is next computed (Eq. 4). The coefficients of this erasure and error locator polynomial are used to compute the remaining terms $S_{33}, \ldots, S_{255}$.

Step 4. This step directly computes the inverse Fourier transform of the vector $(S_1, S_2, \ldots, S_{255})$ to obtain the error and erasure vector. Finally, the received vector is corrected to provide an estimate of the transmitted code word.

IV. Simulation Results

The computation times of this new algorithm and the conventional method described in Ref. 1 for decoding code words which were corrupted by many different error and erasure patterns are given in Tables 1 and 2. These results were obtained by performing five trials for each entry in the tables and then averaging. Along any row or column, the computation times tend to increase with the row or column indices until decoding failures occur due to an excess of allowable errors and erasures. An examination of the decoding times in these two tables indicates that the new decoder operates considerably faster than the conventional decoder described in Ref. 1. If the received word is the same as the originally transmitted code word (i.e., if no errors or erasures occurred), the new decoder will be seven times faster. If the received word contains s erasures and t errors, where $2t + s < 33$, the new decoder will operate about three times faster. Finally, if $2t + s \geqslant 33$, then the new decoder will operate about twice as fast.

Table 1. Decoder execution times in seconds (new method)

Erasures \ Errors	0	1	2	3	4	5	6	7	8	9	10	11	12	13	14	15	16	17
0	0.046	0.119	0.132	0.176	0.161	0.177	0.186	0.201	0.214	0.272	0.240	0.252	0.254	0.328	0.344	0.325	0.319	0.325
1	0.121	0.129	0.144	0.189	0.170	0.185	0.196	0.210	0.223	0.270	0.252	0.261	0.273	0.355	0.360	0.366	0.105	
2	0.131	0.143	0.155	0.200	0.180	0.201	0.208	0.219	0.236	0.247	0.262	0.270	0.232	0.352	0.366	0.346	0.324	
3	0.141	0.151	0.165	0.204	0.192	0.207	0.220	0.232	0.246	0.258	0.270	0.279	0.293	0.388	0.365	0.103		
4	0.150	0.164	0.175	0.188	0.201	0.216	0.230	0.242	0.257	0.265	0.278	0.303	0.301	0.373	0.328	0.339		
5	0.158	0.174	0.186	0.198	0.211	0.228	0.240	0.250	0.260	0.287	0.290	0.298	0.322	0.384	0.097			
6	0.170	0.187	0.196	0.211	0.222	0.237	0.250	0.261	0.274	0.296	0.297	0.307	0.341	0.393	0.337			
7	0.181	0.199	0.207	0.219	0.285	0.245	0.262	0.269	0.283	0.294	0.305	0.356	0.330	0.112				
8	0.192	0.207	0.225	0.229	0.286	0.254	0.267	0.278	0.299	0.304	0.314	0.359	0.337	0.408				
9	0.207	0.215	0.227	0.246	0.278	0.265	0.279	0.289	0.305	0.315	0.325	0.334	0.113					
10	0.211	0.227	0.239	0.248	0.262	0.273	0.289	0.297	0.309	0.322	0.333	0.343	0.442					
11	0.235	0.235	0.247	0.258	0.271	0.284	0.297	0.307	0.320	0.348	0.342	0.088						
12	0.230	0.245	0.256	0.267	0.287	0.293	0.308	0.315	0.327	0.363	0.351	0.356						
13	0.239	0.254	0.265	0.279	0.290	0.302	0.316	0.327	0.338	0.350	0.084							
14	0.250	0.264	0.277	0.287	0.300	0.312	0.325	0.335	0.348	0.366	0.361							
15	0.260	0.274	0.293	0.299	0.311	0.323	0.332	0.344	0.355	0.083								
16	0.270	0.326	0.299	0.305	0.320	0.330	0.342	0.353	0.370	0.377								
17	0.278	0.361	0.334	0.315	0.331	0.340	0.351	0.362	0.081									
18	0.289	0.354	0.350	0.337	0.338	0.349	0.360	0.374	0.389									
19	0.306	0.337	0.325	0.334	0.346	0.357	0.367	0.077										
20	0.315	0.331	0.331	0.344	0.389	0.367	0.379	0.380										
21	0.324	0.342	0.342	0.352	0.417	0.376	0.075											
22	0.324	0.358	0.351	0.360	0.374	0.386	0.388											
23	0.338	0.371	0.361	0.368	0.392	0.074												
24	0.344	0.391	0.370	0.380	0.390	0.393												
25	0.356	0.391	0.401	0.387	0.072													
26	0.363	0.379	0.465	0.398	0.401													
27	0.373	0.393	0.523	0.070														
28	0.381	0.392	0.545	0.407														
29	0.390	0.401	0.092															
30	0.399	0.410	0.504															
31	0.410	0.069																

Table 2. Decoder execution times in seconds (conventional method)

Erasures \ Errors	0	1	2	3	4	5	6	7	8	9	10	11	12	13	14	15	16	17
0	0.314	0.354	0.397	0.463	0.529	0.483	0.515	0.564	0.608	0.681	0.750	0.760	0.734	0.812	0.777	0.940	0.878	0.592
1	0.342	0.375	0.466	0.472	0.483	0.495	0.549	0.584	0.625	0.661	0.709	0.771	0.746	0.792	0.887	0.867	0.414	
2	0.377	0.427	0.439	0.455	0.485	0.557	0.561	0.616	0.609	0.737	0.813	0.703	0.811	0.899	0.871	0.837	0.577	
3	0.382	0.421	0.455	0.481	0.511	0.571	0.574	0.607	0.744	0.757	0.697	0.779	0.814	0.840	0.836	0.429		
4	0.439	0.456	0.466	0.524	0.594	0.634	0.588	0.629	0.761	0.679	0.710	0.778	0.848	0.943	0.957	0.577		
5	0.437	0.471	0.483	0.582	0.583	0.596	0.609	0.638	0.763	0.759	0.782	0.810	0.868	1.054	0.409			
6	0.439	0.472	0.552	0.572	0.574	0.631	0.646	0.656	0.697	0.724	0.808	0.794	0.930	0.997	0.521			
7	0.474	0.492	0.625	0.612	0.588	0.660	0.782	0.679	0.770	0.817	0.790	0.815	0.943	0.401				
8	0.492	0.610	0.647	0.661	0.640	0.648	0.699	0.692	0.820	0.897	0.784	0.864	0.906	0.521				
9	0.583	0.595	0.665	0.626	0.625	0.664	0.720	0.741	0.781	0.840	0.812	0.918	0.432					
10	0.659	0.607	0.668	0.683	0.730	0.724	0.746	0.767	0.769	0.823	0.936	1.034	0.485					
11	0.561	0.695	0.682	0.661	0.741	0.763	0.733	0.770	0.818	0.811	0.849	0.405						
12	0.606	0.661	0.681	0.756	0.691	0.741	0.753	0.783	0.919	0.830	0.912	0.462						
13	0.656	0.638	0.687	0.737	0.708	0.740	0.800	0.816	0.901	0.858	0.356							
14	0.620	0.760	0.716	0.740	0.735	0.779	0.785	0.831	0.924	0.949	0.449							
15	0.693	0.778	0.719	0.749	0.840	0.863	0.824	0.981	0.883	0.424								
16	0.662	0.735	0.715	0.766	0.758	0.860	0.833	0.907	0.912	0.481								
17	0.802	0.744	0.712	0.800	0.789	0.852	0.841	0.864	0.402									
18	0.858	0.720	0.756	0.825	0.806	0.980	0.859	0.879	0.506									
19	0.852	0.747	0.771	0.791	0.802	0.963	0.897	0.347										
20	0.756	0.740	0.841	0.935	0.831	0.878	0.972	0.428										
21	0.758	0.763	0.954	0.911	0.918	0.899	0.386											
22	0.750	0.805	0.956	0.898	0.875	1.049	0.406											
23	0.769	0.807	0.825	0.858	0.910	0.429												
24	0.811	0.902	0.893	0.892	0.907	0.439												
25	0.829	0.857	0.906	0.945	0.342													
26	0.872	0.920	0.907	0.928	0.372													
27	0.960	0.960	0.935	0.340														
28	0.914	0.908	0.935	0.507														
29	1.028	0.930	0.374															
30	0.938	0.945	0.826															
31	0.960	0.374																

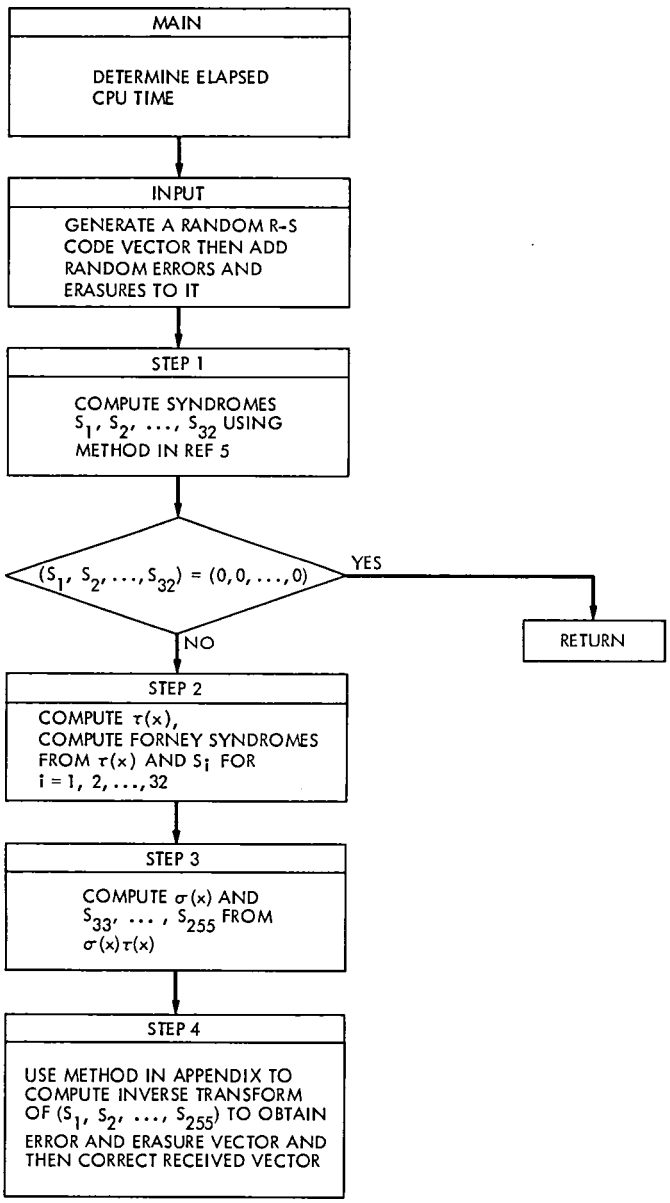

Fig. 1. Basic functional structure of R-S decoding program using transform over *GF* (2^8) and continued fractions

Appendix

This appendix contains the algorithms for computing 3-, 5- and 17-point transforms over fields of characteristic two containing the necessary roots of unity. Let α be an element of order 255 in $GF(2^8)$.

The 3-point transform is given by

$$A_k = \sum_{n=0}^{3-1} a_n \alpha_3^{nk} \quad \text{for} \quad 0 \leqslant k \leqslant 2$$

where $\alpha_3 = \alpha^{85}$ is a primitive cube root of unity.

Algorithm for 3-Point Transform

$$s_1 = a_1 + a_2, \quad A_0 = s_1 + a_0, \quad m_1 = \alpha_3 s_1, \quad s_2 = A_0 + m_1,$$
$$A_1 = s_2 + a_1, \quad A_2 = s_2 + a_2$$

Thus, the 3-point transform requires only one multiplication and five additions.

The 5-point transform is given by

$$A_k = \sum_{n=0}^{5-1} a_n \alpha_2^{nk} \quad \text{for} \quad 0 \leqslant k \leqslant 4$$

where $\alpha_2 = \alpha^{51}$ is a primitive fifth root of unity.

Algorithm for 5-Point Transform

$$s_1 = a_2 + a_3, \quad s_2 = a_1 + a_4, \quad s_3 = a_1 + a_3, \quad s_4 = a_2 + a_4,$$
$$s_5 = s_1 + s_2, \quad A_0 = s_5 + a_0, \quad m_1 = (1 + \alpha_2^3) s_5,$$
$$m_2 = (\alpha_2^3 + \alpha_2^4) s_1, \quad m_3 = (\alpha_2 + \alpha_2^3) s_2, \quad m_4 = (\alpha_2 + \alpha_2^4) s_3,$$
$$m_5 = (\alpha_2 + \alpha_2^5) s_4, \quad s_6 = A_0 + m_1, \quad s_7 = s_6 + m_2,$$
$$s_8 = s_6 + m_3, \quad s_9 = m_5 + a_2, \quad s_{10} = m_4 + a_1,$$
$$s_{11} = m_5 + a_4, \quad s_{12} = m_4 + a_3, \quad A_1 = s_8 + s_9,$$
$$A_2 = s_7 + s_{10}, \quad A_3 = s_7 + s_{11}, \quad A_4 = s_8 + s_{12}$$

Thus, the 5-point transform requires only 5 multiplications and 17 additions.

The 17-point transform is given by

$$A_k = \sum_{n=0}^{17-1} a_n \alpha_1^{nk} \text{ for } 0 \leqslant k \leqslant 16$$

where $\alpha_1 = \alpha^{120}$ is a primitive seventeenth root of unity.

Algorithm for 17-Point Transform

$$S_1 = Y_2 + Y_3, \quad S_2 = Y_1 + Y_4, \quad S_3 = Y_1 + Y_3,$$
$$S_4 = Y_2 + Y_4, \quad S_5 = S_3 + S_4, \quad N_1 = BS_5,$$
$$N_2 = (A + B) S_1, \quad N_3 = (C + B) S_2, \quad N_4 = (C + A) S_3,$$
$$N_5 = (C + A) S_4, \quad N_6 = E \cdot Y_1, \quad N_7 = E \cdot Y_3,$$
$$N_8 = E \cdot Y_4, \quad N_9 = E \cdot Y_2, \quad S_6 = N_1 + N_2,$$
$$S_7 = N_1 + N_3, \quad S_8 = S_6 + N_4, \quad S_9 = S_7 + N_4,$$
$$S_{10} = N_6 + N_5, \quad S_{11} = S_7 + N_5, \quad X_1 = S_{10} + N_9,$$
$$X_2 = S_8 + N_6, \quad X_3 = S_{10} + N_8, \quad X_4 = S_9 + N_7 \qquad \text{(A-1)}$$

where

$$A = \begin{pmatrix} \alpha_1^8 & \alpha_1^6 & \alpha_1^{13} & \alpha_1^{14} \\ \alpha_1^6 & \alpha_1^{13} & \alpha_1^{14} & \alpha_1^2 \\ \alpha_1^{13} & \alpha_1^{14} & \alpha_1^2 & \alpha_1^{10} \\ \alpha_1^{14} & \alpha_1^2 & \alpha_1^{10} & \alpha_1^{16} \end{pmatrix}$$

$$B = \begin{pmatrix} \alpha_1^2 & \alpha_1^{10} & \alpha_1^{16} & \alpha_1^{12} \\ \alpha_1^{10} & \alpha_1^{16} & \alpha_1^{12} & \alpha_1^9 \\ \alpha_1^{16} & \alpha_1^{12} & \alpha_1^9 & \alpha_1^{11} \\ \alpha_1^{12} & \alpha_1^9 & \alpha_1^{11} & \alpha_1^4 \end{pmatrix}$$

$$C = \begin{pmatrix} \alpha_1^9 & \alpha_1^{11} & \alpha_1^4 & \alpha_1^3 \\ \alpha_1^{11} & \alpha_1^4 & \alpha_1^3 & \alpha_1^{15} \\ \alpha_1^4 & \alpha_1^3 & \alpha_1^{15} & \alpha_1^7 \\ \alpha_1^3 & \alpha_1^{15} & \alpha_1^7 & \alpha_1^1 \end{pmatrix}$$

$$D = \begin{pmatrix} \alpha_1^{15} & \alpha_1^7 & \alpha_1^1 & \alpha_1^5 \\ \alpha_1^7 & \alpha_1^1 & \alpha_1^5 & \alpha_1^8 \\ \alpha_1^1 & \alpha_1^5 & \alpha_1^8 & \alpha_1^6 \\ \alpha_1^5 & \alpha_1^8 & \alpha_1^6 & \alpha_1^{13} \end{pmatrix}$$

$X_1 = [A_3, A_{15}, A_7, A_1]^T$, $X_2 = [A_5, A_8, A_6, A_{13}]^T$,

$X_3 = [A_{12}, A_9, A_{11}, A_4]^T$,

$X_4 = [A_{14}, A_2, A_{10}, A_{16}]^T$,

$E = A + B + C + D$

and Y_1 through Y_4 are obtained from the expressions for X_1 through X_4 on replacing each A_i by a_i. Note that (A-1) requires nine (4 × 4) matrix multiplications.

For convenience,

$$\sum_{i=0}^{7} a_i \alpha^i$$

will be represented as the integer

$$\sum_{i=0}^{7} a_i 2^i$$

Observe that N_1 in (A-1) can be put in the form

$$\begin{pmatrix} b_1 \\ b_2 \\ b_3 \\ b_4 \end{pmatrix} = \begin{pmatrix} 44 & 150 & 169 & 195 \\ 150 & 169 & 145 & 185 \\ 169 & 145 & 185 & 193 \\ 145 & 185 & 193 & 36 \end{pmatrix} \begin{pmatrix} c_1 \\ c_2 \\ c_3 \\ c_4 \end{pmatrix} \quad \text{(A-2)}$$

where

$c_1 = a_3 + a_5 + a_{12} + a_{14}$, $c_2 = a_{15} + a_8 + a_9 + a_2$,

$c_3 = a_7 + a_6 + a_{11} + a_{10}$, $c_4 = a_1 + a_{13} + a_4 + a_{16}$

From (B-8) in Ref. 9, one obtains the algorithm for computing (A-2). That is,

$s_1 = c_1 + c_3$, $s_2 = c_1 + c_2$, $s_3 = c_2 + c_4$, $s_4 = c_3 + c_4$,

$s_5 = s_2 + s_4$, $M_1 = 145 \times s_5$, $M_2 = 56 \times s_1$,

$M_3 = 40 \times s_3$, $M_4 = 7 \times s_2$, $M_5 = 80 \times s_4$,

$M_6 = 130 \times c_1$, $M_7 = 23 \times c_2$, $M_8 = 64 \times c_7$,

$M_9 = 205 \times c_4$, $s_6 = a_0 \times M_1$, $s_7 = s_6 + M_2$,

$s_8 = s_7 + M_4$, $s_9 = s_6 + M_3$, $s_{10} = s_9 + M_4$,

$s_{11} = s_7 + M_5$, $s_{12} = S_9 + M_5$, $b_1 = s_8 + M_6$,

$b_2 = s_{10} + M_7$, $b_3 = s_{10} + M_8$, $b_4 = s_{11} + M_9$,

$A_0 + s_5$

Thus,

$b_1 = s_8 + M_6$, $b_2 = s_{10} + M_7$, $b_3 = s_{10} + M_8$,

$b_4 = s_{11} + M_9$

Hence, the total number of Galois field multiplications and additions needed to compute N_1 is 9 and 17, respectively.

The quantities N_i for i = 2, 3, 4, 5, defined in (A-1), are computed by the same procedure as indicated in Ref. 9. The number of multiplications and additions needed to compute N_i for i = 2, 3, 4, 5 is 9 and 15, respectively.

To compute N_i for i = 6, 7, 8, 9, for example, consider $N_6 = E \cdot Y_1$, i.e.,

$$\begin{pmatrix} b_1 \\ b_2 \\ b_3 \\ b_4 \end{pmatrix} = \begin{pmatrix} \alpha^{170} & \alpha^0 & \alpha^{85} & \alpha^0 \\ \alpha^0 & \alpha^{85} & \alpha^0 & \alpha^{170} \\ \alpha^{85} & \alpha^0 & \alpha^{170} & \alpha^0 \\ \alpha^0 & \alpha^{170} & \alpha^0 & \alpha^{85} \end{pmatrix} \begin{pmatrix} a_3 \\ a_{15} \\ a_7 \\ a_1 \end{pmatrix} \quad \text{(A-3)}$$

By a procedure similar to that used to compute the matrix (B-8) in Ref. 9, one obtains the algorithm for (A-3). That is,

$$s_1 = a_3 + a_7, \quad s_2 = a_{15} + a_1, \quad s_3 = s_1 + s_2, \quad M_1 = 1 \times s_5,$$
$$M_2 = 215 \times s_1, \quad M_3 = 214 \times s_2, \quad s_4 = M_1 + M_2,$$
$$s_5 = M_1 + M_3, \quad b_1 = s_4 + a_3, \quad b_2 = s_5 + a_{15},$$
$$b_3 = s_4 + a_7, \quad b_4 = s_5 + a_1 \tag{A-4}$$

Thus, from (A-4), the number of multiplications and additions needed to compute N_6 is 2 and 9, respectively. Similarly, the matrix N_i for i = 7, 8, 9 requires 2 multiplications and 9 additions. After combining the above results, the total number of multiplications and additions needed to compute a 17-point transform in $GF(2^8)$ is 53 and 173, respectively.

References

1. Miller, R. L., Truong, T. K., Benjauthrit, B., and Reed, I. S., "A Reed-Solomon Decoding Program for Correcting Both Errors and Erasures," in *The Deep Space Network Progress Report 42-53*, pp. 102-107, Jet Propulsion Laboratory, Pasadena, Calif., Oct. 15, 1979.
2. Reed, I. S., and Truong, T. K., "A Simplified Algorithm for Correcting Both Errors and Erasures of R-S Codes," in *The Deep Space Network Progress Report 42-48*, Jet Propulsion Laboratory, Pasadena, Calif., Sept. 1978.
3. Odenwalder, J., et al., "Hybrid Coding Systems Study Final Report," Linkabit Corp., NASA CR114, 486, Sept. 1972.
4. Reed, I. S., Scholtz, R. A., Truong, T. K., and Welch, L. R., "The Fast Decoding of Reed-Solomon Codes Using Fermont Theoretic Transforms and Continued Fractions," *IEEE Trans. Inform. Theory*, Vol. IT-24, No. 1, pp. 100-106, Jan. 1978.
5. Berlekamp, E. R., and Ramsey, J. L., "Readable Erasures Improve the Performance of Reed-Solomon Codes," *IEEE Trans. Inform. Theory*, Vol. IT-24, No. 5, Sept. 1978.
6. Reed, I. S., Truong, T. K., and Miller, R. L., "A Fast Technique for Computing Syndromes of BCH and RS Codes," in *The Deep Space Network Progress Report 42-52*, pp. 67-70, Jet Propulsion Laboratory, Pasadena, Calif., Aug. 15, 1979.
7. Winograd, S., "On Computing the Discrete Fourier Transform," *Proc. Nat. Acad. Sci. USA*, Vol. 73, pp. 1005-1006, 1976.
8. Reed, I. S., and Truong, T. K., "Fast Mersenne-Prime Transforms for Digital Filtering," *Proc. IEEE*, Vol. 125, No. 5, pp. 433-440, May 1978.
9. Reed, I. S., Truong, T. K., Miller, R. L., and Benjauthrit, B., "Further Results on Fast Transforms for Decoding Reed-Solomon Codes over $GF(2^m)$, for m = 4, 5, 6, 8," in *The Deep Space Network Progress Report 42-50*, pp. 132-154, Jet Propulsion Laboratory, Pasadena, Calif., Jan. 15, 1979.
10. Berlekamp, E. R., *Algebraic Coding Theory*, McGraw Hill, New York, 1968.

The Microprocessor-Based Synthesizer Controller

H. Donnelly, M. R. Wick, R. W. Weller, G. B. Schaaf, B. Barber, and M. A. Stern
Radio Frequency and Microwave Subsystems Section

The design and implementation plan of a new microprocessor-based controller for the Dana Digiphase Synthesizer is presented. Improvements over the present controller, POCA, are discussed including greater operating capability, increased phase control accuracy and the addition of diagnostics.

I. Introduction

The need to track low level signals with high doppler rates and ranges brought about a demand for Digitally Controlled Oscillators (DCOs) with a programmable frequency capability. Recently, the limited frequency tracking range of one of the Voyager spacecraft receivers underscored the need for this capability on the up-link.

With the advent of microprocessors, significant improvements in control and monitor of the Dana Digiphase Synthesizer were possible with a decrease in the amount of hardware required. The microprocessor provides for additional monitor capability, controller interface processing and functional diagnostics. This new controller incorporates the latest advance in microcomputing technology.

The phase coherent digiphase (Ref. 1) technique of the synthesizer provides a precise frequency source from which the output phase approximates a theoretical ramp when ramping. The synthesizer output is derived from a VCO which is phase locked to a digitally synthesized reference, thus the output phase is predictable and limited only by the inaccuracies of time tagging a ramp start and stop. This Controller performs the measurement and removal of these inaccuracies (or reduces them to a tolerable range of 1 μsec).

II. Description

The Synthesizer Controller, hereafter referred to as the Controller, is designed to control and monitor the Model 7010-S-241 Frequency Synthesizer (Ref. 2) manufactured by Dana Laboratories, Inc. The Controller receives serial data commands from the computer via an industry standard RS-232 command port and outputs parallel BCD frequency commands to the synthesizer. The commands received by the Controller are in ASCII format; they cover a wide variety of Controller functions, including loading a series of frequency ramps, the start time for execution of the ramp sequence editing functions, status reporting and diagnostics.

A sequence of 100 ramps may be stored in the command table. Once loaded, the Controller is ready to execute the ramps in a continuous sequence from any point in the table. This sequence of ramps can be used to approximate a smooth frequency function over time.

A set of specifications for the controller is given in Table I.

III. Controller Development Program

In 1977, development work began under the 310 program on a microprocessor-based controller that would replace the existing Programmed Oscillator Control Assembly (POCA) (Refs. 2 and 3) as controller of the DCO. One engineering model controller was built and successfully tested.

The computing device which controlled this engineering model was a National Semiconductor 16 bit PACE microprocessor. Although the PACE microprocessor was the logical choice at the time, it subsequently was "obsoleted" by the manufacturer.

Though the operational Controller now under development uses much of the hardware and software design of the engineering model developed under the 310 program, the PACE and related circuitry has been replaced with the Intel single-board microcomputer ISBC 86/12.

At the time of this report, the Controller design has been completed, a prototype has been assembled, and functional tests initiated. Test results will be reported in the next DSN Progress Report.

IV. Phase Error Correction Schemes

The Controller development activity focused on the removal of the sources of accumulated phase errors. "Phase error" in the context of this report is defined as a deviation from the equation representing the ideal phase total of a sequence of ramps:

$$\phi(T) = \sum_{K=1}^{N_R} 1/2\, M_K\, T_K^2 + F_K T_K$$

where

$T \triangleq \sum_{K=1}^{N_R} T_K$, the sum of the series of ramp durations

$N_R \triangleq$ the total number of ramps in the sequence

$K \triangleq$ the number designating a single ramp

$M_K \triangleq$ the slope of the Kth ramp

$F_K \triangleq$ the initial frequency of the Kth ramp

There are three principal sources of phase error in the DCO.

A. Synthesizer-Delay Induced Phase Error

This source of error is caused by the time delay between the clock pulses in the Dana Digiphase Synthesizer and the Controller. Although both devices operate from the same reference frequency, the Controller is synchronized to real time and the synthesizer is not. To correct this source of error, the 1 PPS signal from the real time reference will be used to synchronize the synthesizer to real time.

B. Phase Error Due to Truncation of the Ramp Rate

This contribution to the phase error is the result of truncation in the ramp rate computation. After the Controller receives a ramp command of a frequency change (Δf) over a time interval (Δt), it computes the ramp rate. This error, due to ramp rate truncation, is reduced by using a sufficient number of digits in performing the ramping summation. The required number of significant digits in the ramp rate computation is discussed in the following.

Let M_I be the ideal ramp rate and M_T be the truncated ramp rate. The phase error due to ramp rate truncation is:

$$\phi_{RT} = 1/2\, M_I \cdot T^2 - 1/2\, M_T \cdot T^2$$

$$= 1/2\, (M_I - M_T) \cdot T^2$$

where

ϕ_{RT} is the cumulative phase error at time T due to ramp rate truncation.

The Controller with its 22 digits of precision obtains:

$$\frac{\phi_{RT}}{8\text{ hrs}} = 1/2 \cdot (10^{-21}\text{ cycles}) \cdot (2.88 \cdot 10^{9} \cdot \Delta T)/8\text{ hrs}$$

$$= \frac{1.44 \cdot 10^{-12}\text{ cycles}}{8\text{ hrs}}$$

–a figure significantly better than the controller specification requirement of 10^{-4} cycles/8 hrs.

C. Phase Error Due to the Staircase Construction of Ramps

This source of phase error is caused by the inherent delay due to the stepwise change of frequency commands to the synthesizer. The synthesizer output frequency produces a ramp that follows the staircase control input. This effect is illustrated in Fig. 1.

The cumulative phase error may be considered graphically as the area bounded in the illustration by the ideal ramp slope, the uncorrected ramp pattern, and the line representing the present moment in time.

This error may be expressed as the difference between the cumulative phase of the ideal ramp and the cumulative phase of the staircase ramp:

$$\phi_{SE} = 1/2 \cdot N_T \cdot \Delta F \cdot T - \sum_{N=1}^{N_T-1} \Delta F \cdot \Delta T \cdot N$$

where

$\phi_{SE} \triangleq$ the phase error due to the staircase effect

$N \triangleq$ the number of a single step in a ramp

$N_T \triangleq$ the total number of steps in the ramp

Taking the average value of N over the summation we have:

$$\phi_{SE} = 1/2 \cdot N_T \cdot \Delta F \cdot T - \frac{N_T}{2} \cdot (N_T - 1) \cdot \Delta F \cdot \Delta T$$

Since

$$N_T = T/\Delta T,$$

$$\phi_{SE} = 1/2 \cdot N_T \cdot \Delta F \cdot T - \frac{N_T - 1}{2} \cdot \Delta F \cdot T$$

$$= 1/2 \cdot N_T \cdot \Delta F \cdot T - \frac{N_T \cdot F \cdot T}{2} + \frac{\Delta F \cdot T}{2}$$

$$\phi_{SE} = +\frac{\Delta F \cdot T}{2}$$

1 Hz/10 μsec is the maximum slope that the Dana Synthesizer can ramp. This results in a staircase ramp phase error of:

$$\phi_{SE} = +\frac{\Delta F \cdot T}{2} = \frac{(1\text{ Hz})\,(10\ \mu\text{sec})}{2} = +0.5\text{ cycles/sec}$$

The uncorrected staircase ramp has a clearly unacceptable amount of phase error. Two a priori corrections are used to reduce this source of phase error to less than 10^{-4} cycles/8 hrs.

First, a gross correction is accomplished by adding one-half the increment step value to the command frequency prior to the start of a ramp. By this technique, the deviations from the desired theoretical phase value will cancel out and at the completion of a ramp, this half frequency step is subtracted out. Second, the discrete nature of the command frequency prevents the phase deviations from balancing out perfectly; therefore, a fine adjustment is required. This fine adjustment is implemented in hardware and consists of a special register which accumulates the phase error due to the command frequency truncation. When the error reaches a sufficient amount, the least significant digit of the command frequency (10^{-6} Hz) is incremented for one additional cycle (10 μsec). Figure 2 illustrates this phase correction process.

V. Hardware Implementation

Implementation of the Controller logic requires three printed circuit boards: The Intel ISBC 86/12 micro-computer, the "Timing and Interface Logic" (Board No. 1), and the "Frequency Command Logic" (Board No. 2). The functions performed by each board are described in the following sections; a block diagram of the hardware functional elements is shown in Fig. 3.

A. Intel ISBC 86/12 Microcomputer

The ISBC 86/12 Single Board Computer is a complete computer system on a single printed-circuit assembly. The ISBC 86/12 includes a 16-bit central processing unit (CPU), 32K bytes of dynamic RAM, 16K bytes of read only memory, a serial communications interface, three programmable parallel I/O ports, programmable timers, priority interrupt control, Multibus control logic, and bus expansion drivers for interface

with other Multibus-compatible expansion boards. For further information on the microcomputer, refer to the Intel ISBC 86/12 reference manuals.

B. Timing and Interface Logic

1. **Microcomputer interface.** Board No. 1, containing the timing and interface logic, provides the basic interface between the microprocessor, and Boards No. 1 and No. 2. It provides computer bus termination, TTL Gates for address buffering and transceiver elements for bidirectional signal buffering of the microcomputer data lines.

2. **Address decode logic.** The address decode logic receives the register address from the microcomputer and decodes it into the various enabling signals that force data to be input and output from the internal system registers.

3. **Data Port.** The Data Port operates in a way similar to the Command Port resident on the microcomputer board. It utilizes the Intel 8251A Programmable Communication Interface IC and receives its clock signals from the programmable counter residing on the Microcomputer Board.

4. **Real Time Clock Logic.** The Real Time Clock receives a 100 kHz reference frequency from the Dana Synthesizer along with a 1 pulse per second (1 PPS) signal from the external station Frequency and Timing Subsystem (FTS). The 1 PPS signal is synchronized with the 100 kHz reference clock and the reference clock drives the time counters which can be preset to the correct time of day and year.

The Real Time Clock can be preset as follows. One method is to connect the FTS time source and parallel load all digits at once. The second method is to load the time counters in four word transfers from the microcomputer. The internal time clock has a resolution of 10 μsec and a range of 999 days. The source of the actual time used for sequence operations is selectable; it may be either internal or external. If the internal clock is selected, the external FTS will be disregarded and the internal time counter outputs will be presented to the system. If the external FTS signals are lost while the system is in the external time mode, the internal time clock will take over without a significant time delay. The internal clock continuously monitors the external FTS time prior to the changeover, so it is set to station time.

5. **Time Tag Logic.** A Time Tag has the same resolution and range as the Real Time Clock. It is stored in the Time Tag register along with a frequency control function. The Time Tag is continuously compared to the Real Time Clock and when the time matches, the frequency control ramping function is executed. In this way frequency control operations can be set up at the normal computer transfer rates while being executed with precise time correlation.

The Time Tag logic consists of a storage register for the Time Tag value and a comparator to compare with all the digits of the Real Time Clock. When a match occurs, a signal is generated to interrupt the CPU.

C. Frequency Command Logic

1. **Frequency Ramp Control.** The frequency ramp control logic receives data from the microcomputer specifying the frequency ramps. It can be instructed to start and stop a ramp, command any fixed frequency, or command positive and negative frequency ramps of any magnitude within the operating range of the Dana Digiphase Synthesizer. The microcomputer writes into three data registers which are accessed by the ramp control logic. One is for the initial frequency value and the other two contain the incremental frequency values. The frequency ramp control logic consists of these data registers, a two-stage serial adder, and storage and control logic. The ramp control sequence is as follows.

The control logic receives a command to load the contents of the initial value register to the output. This operation occurs in the next 10 μsec and the initial value is transferred to the first stage of the output storage. Next, the control logic is commanded to load the incremental frequency into the adder and add this value to the initial value. Simultaneously the initial value is transferred to the record stage of output storage where it is output to the synthesizer. When the add cycle is complete, the new command is residing in the first stage of output storage. Thereafter, every 10 μsec, a new frequency value is produced in the same manner as described above and the values are transferred from stage one of the output storage to the output. This process continues until the microcomputer transmits a stop command.

2. **Phase Counter.** The phase counter monitors the synthesizer output and reports a cycle count to the microcomputer every 100 msec. The Phase Counter consists of a high-speed synchronized counter capable of running at a maximum rate of 51 MHz.

3. **Synthesizer Status.** The synthesizer status register consists of three re-triggerable one-shots, each monitoring a specific synthesizer clock signal including 100 kHz, 1 MHz and 5 MHz. If a clock signal is substantially off frequency or stops completely, the respective one-shot will flag the microcomputer. Other signals monitored are "Synthesizer Power On" and a latch that monitors the "Synthesizer No Lock" signal. If phase lock is lost at any time, a "Lock Lost" flag is set in the Controller and is automatically reset when reading the synthesizer status register. Three tell-tale contact closures are also

provided. They report "Synthesizer Ready," "Phase In-Lock" and "Synthesizer Power On" available via a connector to an external data monitor.

VI. Firmware Implementation

The firmware in the Controller uses a simple, dedicated, interrupt-driven "Foreground-Background" operating system. Background Tasks are entered into a task queue as a result of messages received from either of two interrupt-driven RS232 ports or from the currently active task. A Task Dispatcher selects the oldest task in the queue for execution. All Background Tasks run to completion and then return control to the Task Dispatcher.

Foreground Tasks are initiated by one of several Background Tasks and interrupt-driven thereafter. Foreground Tasks may be self-terminating or terminated by a Background Task. The Controller firmware is illustrated in Fig. 4 and consists of the following modules:

Control – contains system initialization logic and the Task Dispatcher

I/O – performs all I/O with the Controller electronics

RS232 – provides message-oriented I/O with two RS232 ports

Math – performs 32 digit BCD arithmetic, addition and subtraction in time format (ddd:hh:mm:ss) and conversion from time format to seconds

Report – formats status reports for output to the RS232 ports

List – formats listing of the Command List for output to the RS232 ports

Syntax – processes messages received from the RS232 ports and places calls to the indicated task in the Task Dispatcher

Ramp – provides two closely related functions – ramp control, which controls the execution of a frequency ramp series, and the Performance Monitor, which detects and reports errors in the operation of the Controller

Diagnostic – performs diagnostics on the Controller electronics

The Controller includes the firmware necessary to accomplish the following tasks:

(1) Accept data which defines up to 100 frequency ramps, calculate ramp rates, and store the parameters in a "Command List".

(2) Allow modification and display of the Command List.

(3) Output data from the Command List and send commands to the Controller electronics in the sequence required to generate the specified series of ramps.

(4) Monitor operation of the Controller electronics and the synthesizer and report errors and status as required.

(5) Perform diagnostics of the Controller electronics.

The hardware elements used by the firmware are illustrated in Fig. 5:

(1) Synthesizer Output Register – contains a frequency value which is output to the synthesizer every 10 μsec.

(2) Initial Frequency Register – The contents of this register are loaded directly into the Synthesizer Output Register whenever a specific frequency value is required (typically at the beginning of a ramp).

(3) Increment Registers – Two increment registers are provided. While a ramp is executing, the active Increment Register contains the value to be added to the Synthesizer Output Register every 10 μsec in order to generate the desired frequency ramp. The 2nd register is loaded with the increment value for the next ramp and becomes active when a change in ramp rate is required.

(4) Serial Adder – adds the selected Increment Register to the contents of the Synthesizer Output Register and stores the sum in the Synthesizer Output Register.

(5) Controller Clock – maintains time in days, hours, minutes, seconds, down to 10 μsec resolution. The clock is normally driven by an external time source. An interrupt to the processor is generated on every 100 msec clock edge.

(6) Time Tag Register – is loaded in the same format as the Controller clock with the time one of the events listed in item 7 is required to occur.

(7) Time Comparator – generates an output when the values in the Controller clock and the Time Tag Register are identical. This "Time Tag Match" signal generates an interrupt to the processor and also initiates one of the following actions:

(a) Load the Synthesizer Output Register with the contents of the Initial Frequency Register and stop the Serial Adder.

(b) Load the Synthesizer Output Register with the contents of the Initial Frequency Register, select Increment Register No. 1, and enable the Serial Adder.

(c) Load the Synthesizer Output Register with the contents of the Initial Frequency Register, select Increment Register No. 2, and enable the Serial Adder.

(d) Select Increment Register No. 1 and enable the Serial Adder.

(e) Select Increment Register No. 2 and enable the Serial Adder.

(8) Phase Counter – a 9 digit BCD counter which is incremented once by each cycle generated by the Synthesizer.

VII. Performance Monitor

Two mechanisms used to monitor performance of the system are the Cycle Count Monitor and the Watchdog Timer.

Cycle Count Monitor, a 9 digit BCD counter in the Controller, is incremented once with each cycle output by the synthesizer. The counter is never reset, it "rolls over" to zero. Every 100 msec the contents of the counter are latched into a register which can be read by the processor and the 100 msec interrupt to the processor is generated. When the interrupt is received the processor reads the cycle count value and calculates the absolute difference between the current reading and the reading taken at the previous 100 msec interrupt. This difference is the number of cycles output by the synthesizer in the previous 100 msec interval. The processor adds this value to a 30 digit BCD accumulator to obtain the total number of cycles generated since the counters were reset. Using the Commanded Frequency at the start of the interval and the Commanded Rate, the processor calculates the cycle count expected for the interval. This calculation is carried to 22 fractional digits. This value is then added to an accumulator which contains 30 integer and 22 fractional digits to give the expected cycle count. The integer portion of the expected cycle count is then compared with the generated cycle count. The error bound is +0, -1 since the actual cycle count is derived from a zero crossing detector and gives an uncertainty of one cycle.

The failure of the 100 msec interrupt signal could result in an undetected error condition. Failure of the Time Tag match logic or the Time Tag interrupt could give a similar result since the Performance Monitor operates on the data presented when the Time Tag interrupt occurs. A programmable interval timer supplied on the ISBC 86/12 board is used to monitor the operation of the 100 msec clock interrupt. The device is configured as a programmable one-shot. The one-shot is retriggered by the 100 msec clock interrupt routine. If the 100 msec interrupt fails to appear at the proper time, this Watchdog Timer generates an interrupt to indicate the error condition.

Proper operation of the Time Tag logic is checked by the Performance Monitor, which is driven by the 100 msec clock interrupt. A counter which contains the time interval until the next programmed time tag is maintained in the Performance Monitor. This counter is loaded by the Time Tag interrupt routine and is decremented by the Performance Monitor every 100 msec.

VIII. Diagnostics

A portion of the microcomputer firmware is dedicated to checking the condition of the Controller electronics. Two hardware features are especially useful for troubleshooting purposes.

(1) A means for the processor to read the contents of the Synthesizer Output Register.

(2) A means to single step the Serial Adder. The diagnostic procedures are intended to fullfill two functions, Confidence Tests and Fault isolation.

Confidence Tests are executed during system power-up and on receipt of the appropriate command from the Command Port. They are intended to verify that the Controller electronics are functioning correctly.

Clock tests – The microcomputer performs several read/write tests on the Real Time clock. A "walking one" pattern series followed by a "walking zero" pattern series is used to test each bit used in the clock register. These tests are followed by a test of each decade. This is accomplished by writing the appropriate pattern, allowing the clock to count once, and then reading the clock value.

Time Tag tests – the Time Tag register, time comparator, and Time Tag interrupt logic is tested by writing the same "walking one" and "walking zero" patterns, first to the clock and then to the Time Tag register. Proper operation of the Time Tag interrupt is checked after each pattern write.

Initial Frequency Register tests – this register is tested by writing a pattern to the register, loading the frequency, setting the clock and Time Tag for a match and then reading the Synthesizer Command Register. "Walking" patterns are used to test each bit.

Increment Register tests – the two increment registers are independently tested. After a pattern is written to the register, the serial adder is stepped through one complete cycle. A correct comparison with the Synthesizer Command Register verifies proper operation. Again, walking bit patterns are used.

Fault Isolation Tests provide a means for maintenance personnel to narrow the fault location to a specific area of the electronics. These tests are identical to the tests performed by the Confidence Tests; however, they provide error data and control functions to a terminal connected to the Command Port. The error data consists of patterns indicating the bit pattern expected and the bit pattern generated by the Controller electronics.

References

1. "Dana Model 7010-S-179 Digiphase Frequency Synthesizer," Dana Publication No. 980428-S-179, July 1971.
2. Wick, M.R., "DSN Programmed Oscillator Development," in *The Deep Space Network Progress Report*, Technical Report 32-1526, Vol. VIII, pp. 111-124, Jet Propulsion Laboratory, Pasadena, California, April 15, 1972.
3. Wick, M. R., "DSN Programmed Oscillator," in *The Deep Space Network Progress Report 42-20*, pp. 167-177, Jet Propulsion Laboratory, Pasadena, California, April 15, 1974.

Table 1. Controller specifications

Frequency Control

Range: 40,000,000.000,000 to 50,999,999.999,999 Hz
Resolution: 1 μHz

External Time Source

Range: 999 days, 23 hours, 59 min, 59.999 sec
Resolution: 1 msec

Internal Time

Resolution: 10 μsec

Command Frequency Rates

Minimum ramp period:	100 msec
Maximum ramp rate:	100 kHz/sec
Ramp resolution:	1 μHz per 100 msec ramp

Instantaneous Frequency Error

At f = 45 MHz and a ramp rate of 100 kHz/sec

$$\frac{f \text{ error}}{f} = 2.22 \times 10^{-7}$$

At lesser ramp rates, $\frac{f \text{ error}}{f}$ is reduced proportionately.

A plot of this error is shown in Fig. 6.

Phase Error

Maximum accumulated phase error: 10^{-4} cycles/8 hour ramp

Data Storage

Maximum number of ramps: 100 ramps

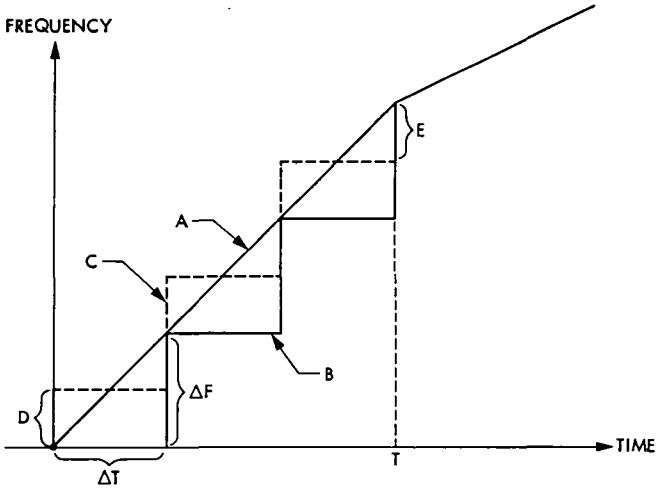

A : DESIRED RAMP
B : STAIRCASE RAMP (UNCORRECTED)
C : PHASE-CORRECTED RAMP
D : INITIAL 1/2 FREQUENCY INCREMENT CORRECTION
E : FINAL 1/2 FREQUENCY INCREMENT CORRECTION

Fig. 1. Frequency ramp construction

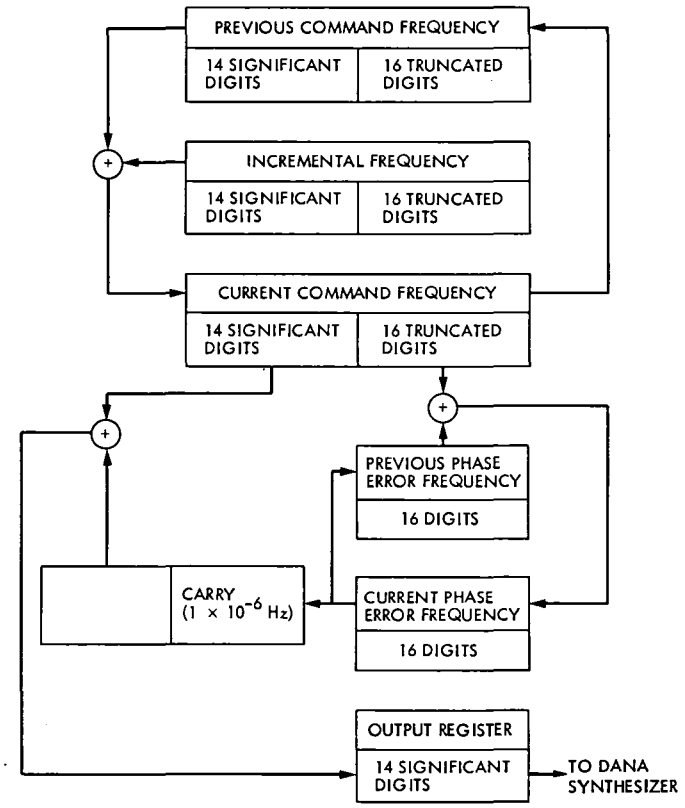

Fig. 2. Phase error correction mechanism

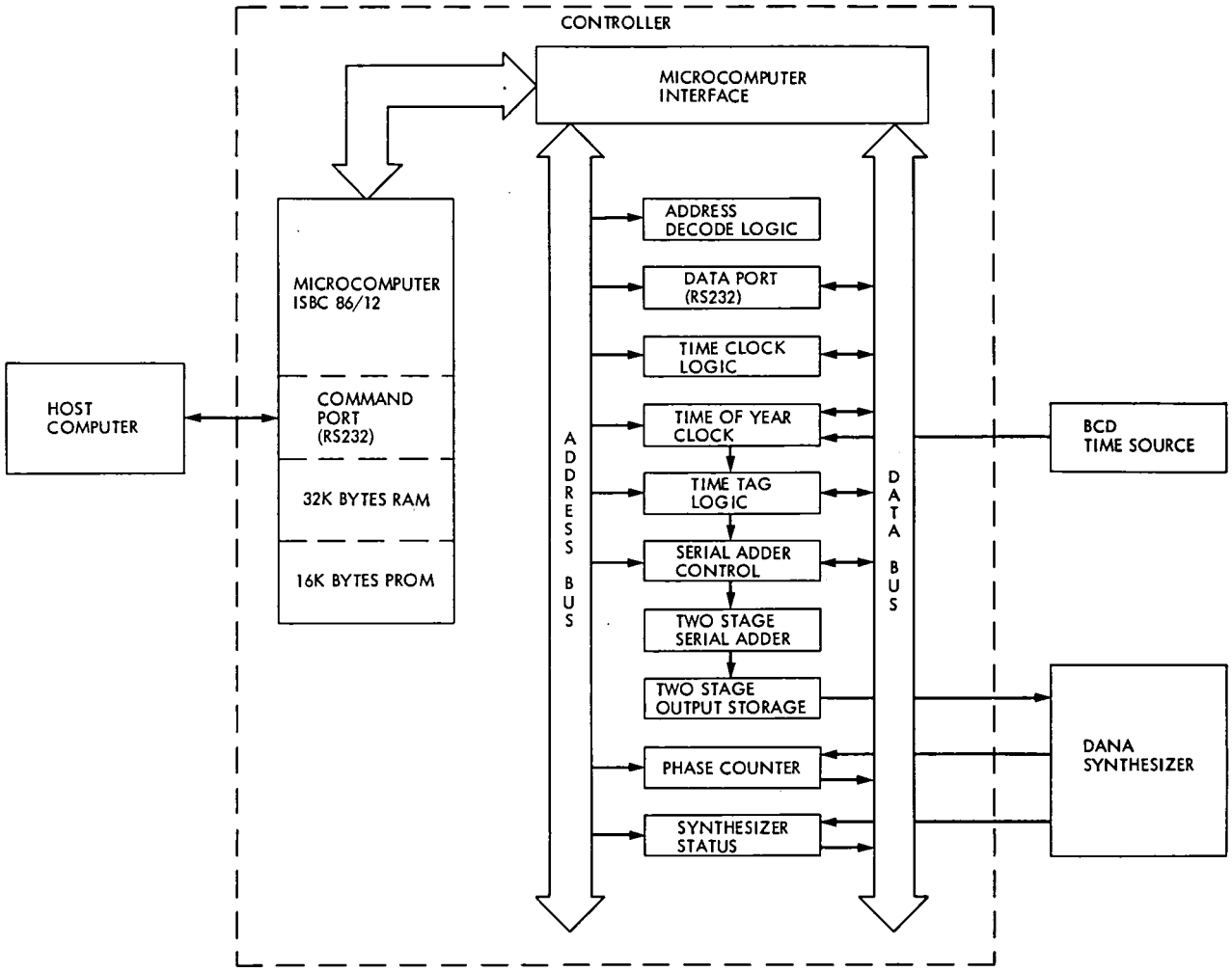

Fig. 3. Hardware block diagram

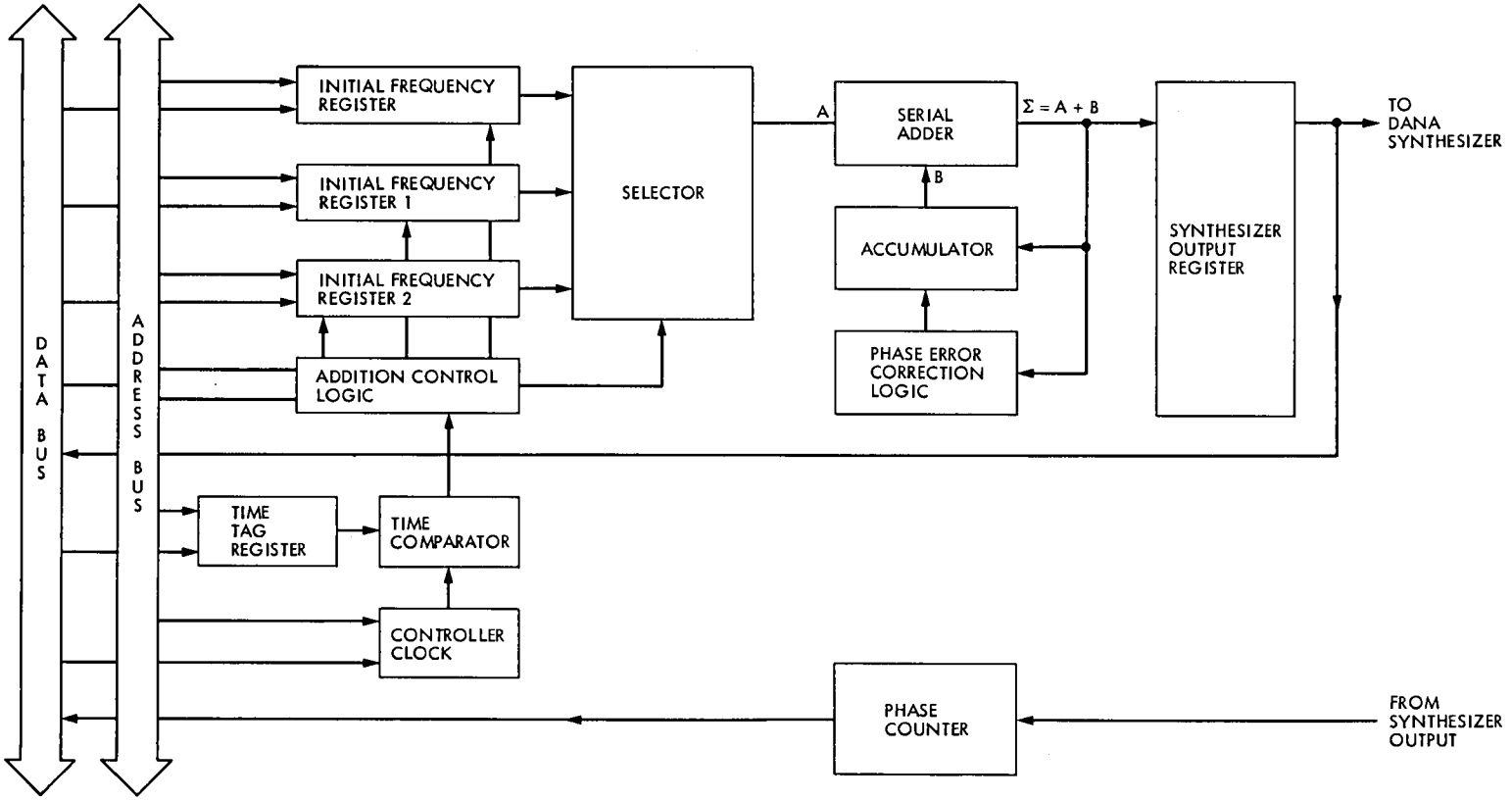

Fig. 4. Hardware elements used by the firmware

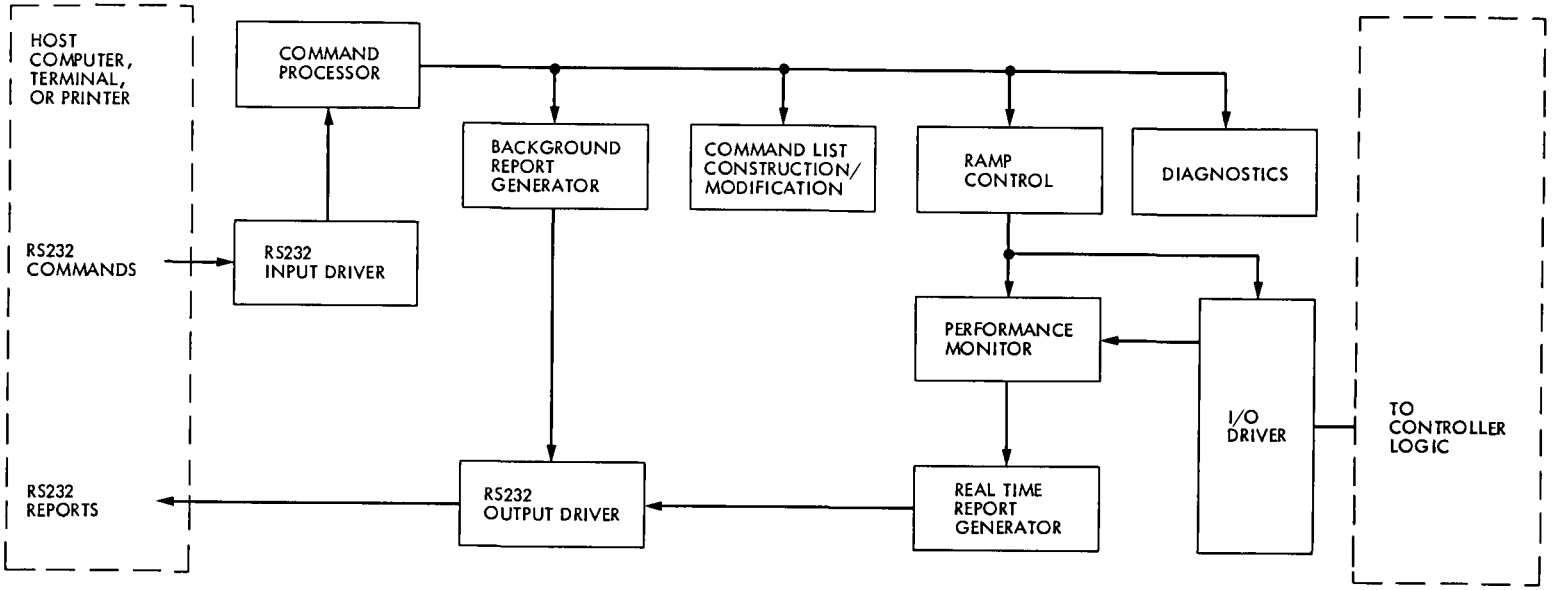

Fig. 5. Firmware block diagram

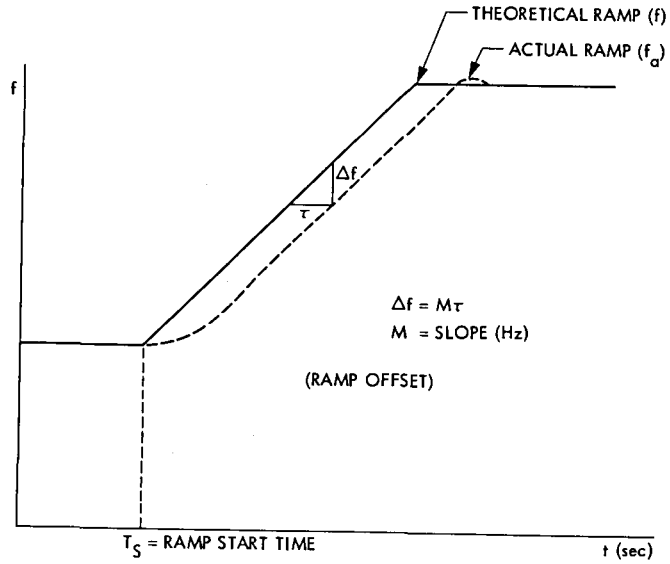

Fig. 6. Instantaneous frequency error

Damping of Temperature Fluctuations Using Porous Matrices

F. L. Lansing
DSN Engineering Section

This article examines the concept of utilizing the thermal attenuation characteristics of porous matrices and their thermal flywheel effect in damping the air temperature fluctuations for highly temperature-sensitive applications. The mathematical formulation of the problem in a dimensionless form is presented together with the relevant boundary conditions. The periodic temperature solution at a given matrix section has shown that the amplitude will be reduced by a logarithmic decrement and that the temperature cycle possesses a phase angle lag which depends on various flow and material properties, as well as the frequency of the temperature fluctuations. The effect of different material properties for porous matrix selection was examined by a numerical example.

I. Introduction

One of the major operation requirements for the frequency and timing subsystem for the Deep Space Network tracking antennas is the installation of a highly temperature-sensitive hydrogen maser oscillator to keep the microwave energy at a stable frequency. The maser oscillator is kept at a fixed predetermined temperature and is enclosed by several shields to isolate it from the effects of ambient temperature fluctuations. The hydrogen maser is housed in a special room which is air-conditioned by a conventional air-handler (fan-coil) unit. However, the system is thermally controlled to tolerate a very small periodic temperature fluctuation. This thermal protection was imposed in order to limit the operational frequency variations or drift to a minimum.

Although the early temperature control design of the air conditioner of the maser room was satisfactory, a better refinement of the temperature control has recently been sought to improve the system's operationability. Currently, several solutions are being investigated to reduce the frequency and temperature drifts due to the fluctuating room occupancy, maser wattage, ambient temperature, and solar irradiancy.

One of the suggested solutions is to let the conditioned air leaving the fan-coil unit pass through a porous matrix acting as a thermal flywheel which damps the temperature fluctuations up to the desired degree. This article addresses the mathematical analysis of the problem and the correlation between the relevant parameters. The objective is to obtain a

solution for the temperature distribution of an unsteady one-dimensional flow with constant transport properties through a porous matrix in which conduction and convection play a major role. Of major concern to the designer is the temperature profile at the fluid exit section, whereafter the fluid is directed to the maser oscillator. After the problem is analytically formulated, the system differential equation is solved and presented in Appendix A. The method of computations is given and illustrated by a numerical example. The matrix preliminary design procedure is also discussed briefly to acquaint the designer with the sequence to be followed.

II. Analysis

Consider an element of a porous matrix as shown in Fig. 1 with a thickness dx placed at a distance x from the inlet fluid section, with properties C, ρ, and K for the specific heat, density and thermal conductivity, respectively. The assumptions and the idealizations made in the analysis are as follows:

(1) The heat conduction and fluid flow through the porous matrix are one-dimensional. The cross sectional area of matrix is denoted by A.

(2) Thermal, physical, and transport properties of the matrix and the fluid are assumed to be spatially uniform over the entire control volume and independent of the operating temperature fluctuations.

(3) The fluid temperature at the entrance section ($x = 0$) is assumed to be sinusoidal. This is considered an adequate approximation to a temperature profile with a periodic drift due to the oscillations of ambient air temperatures, solar intensity, etc.

(4) The matrix boundary is assumed to be well insulated such that no heat exchange is taking place along the matrix length with environment.

Denoting the assumed uniform porosity (ratio of fluid volume in pores to matrix volume) by P, the fluid properties by the subscript (f), and the solid matrix properties by the subscript (s), the conservation of energy for the unsteady one-dimensional flow can be written as follows, for the fluid flowing in the positive x-direction

$$P K_f \frac{\partial^2 T_f}{\partial x^2} - \frac{\dot{m}_f C_f}{A} \frac{\partial T_f}{\partial x} + H\zeta (T_s - T_f) = P C_f \rho_f \frac{\partial T_f}{\partial \tau} \tag{1a}$$

where $\dot{m}_f$ is the fluid mass flow rate, H is the average heat transfer coefficient between the solid matrix and the fluid in the pores and ζ is the average fluid surface area of pores per unit matrix volume. The first term in the left hand side of Eq. (1a) represents the fluid conduction; the second term represents convection by the moving fluid; and the third term represents the heat gained due to the convection-radiation exchange between the fluid in the pores and matrix solid. Note that in formulating Eq. (1a), the effective fluid cross sectional area is PA and the effective elementary volume is $PAdx$, assuming that the pores are uniform and could be lumped together to form only one large pore next to a one lumped solid.

For the solid matrix, on the other hand, the energy equation is written as

$$(1 - P) K_s \frac{\partial^2 T_s}{\partial x^2} - H\zeta (T_s - T_f) = (1 - P) C_s \rho_s \frac{\partial T_s}{\partial \tau} \tag{1b}$$

The first term in the left hand side of Eq. (1b) represents the solid matrix conduction and the second term represents the heat lost to the fluid by convection-radiation exchange. Equations (1a) and (1b) represent a system of two simultaneous, partial differential equations in the two functions $T_f(x,\tau)$ and $T_s(x,\tau)$.

A cursory look at Eqs. (1a) and (1b) shows that the solution of fluid and solid matrix temperatures will be almost identical if the fluid rate is very small and that the heat-convection-radiation term is small. Although Eq. (1a) and (1b) could have been solved for T_f and T_s in sufficient detail and accuracy, almost all analytical studies of transpiration-cooled matrices avoid the resulting complexity by making an additional simplifying assumption. The latter is to treat the temperatures T_f and T_s as equal at any position throughout the flow (Refs. 1-6). This assumption may not be very accurate for matrix heat exchangers (regenerators) with large fluid flow rates or with a high rate of change of fluid temperatures. However, this idealization in the mathematical model is still considered of utmost value as described in Refs. 1-6.

III. Governing Differential Equation

By adopting the equal temperature assumption given in the last section, Eqs. (1a) and (1b) could be summed to form the new system differential equation in the temperature $T(x,\tau)$ as

$$K_e \frac{\partial^2 T}{\partial x^2} - G_f C_f \frac{\partial T}{\partial x} = \rho_e C_e \frac{\partial T}{\partial \tau} \tag{2}$$

where the subscript (e) refers to the effective fluid-solid matrix properties, G_f is the fluid mass flux ($\dot{m}_f/A$) and the effective properties K_e and $\rho_e C_e$ are determined from:

$$\left.\begin{aligned} \rho_e C_e &= \rho_f C_f P + \rho_s C_s (1-P) \\ K_e &= K_f P + K_s (1-P) \end{aligned}\right\} \quad (3)$$

By dividing Eq. (2) by K_e, the differential equation will be reduced to

$$\frac{\partial^2 T}{\partial x^2} - \frac{G_f C_f}{K_e}\frac{\partial T}{\partial x} = \frac{1}{\alpha_e}\frac{\partial T}{\partial \tau}$$

where α_e is the "effective" thermal diffusivity for the matrix, defined by

$$\alpha_e = K_e/\rho_e C_e \quad (4)$$

In order to obtain a general solution to this periodic heat-transfer problem regardless of the range of operating conditions or the physical units used in computations, a dimensionless form of Eq. (2) is sought. The dimensionless parameters for temperature θ, time N and distance X, were finally selected, after making several dimensioning and substitution trials, to be as follows:

$$\left.\begin{aligned} \theta &= \frac{T(x,\tau) - T_m}{\Delta_0} \\ N &= f\tau \\ X &= x\sqrt{f/\alpha_e} \end{aligned}\right\} \quad (5)$$

where the amplitude Δ_0, the mean temperature T_m and the frequency f are depicted in Fig. 2. Substituting in Eq. (2) using Eq. (5), the dimensionless form of the system's partial differential equation can be written for the temperature θ (X,N) after some manipulation as

$$\frac{\partial^2 \theta}{\partial X^2} - F\frac{\partial \theta}{\partial X} = \frac{\partial \theta}{\partial N} \quad (6)$$

where F is a dimensionless flow parameter, defined as

$$F = \frac{G_f C_f}{K_e}\sqrt{\frac{\alpha_e}{f}} \quad (7)$$

At zero flow factor F, which means at no flow condition or for the case of a solid surface, the differential equation is reduced to the one-dimensional transient heat transfer form with its known solution (Ref. 7). The existence of the term $F(\partial\theta/\partial X)$, however, makes the solution procedure somewhat different.

IV. General Solution

The partial differential equation, Eq. (6), could be solved by using the separation of variables procedure where the dimensionless temperature θ (X,N) is written in general as the product of the two functions $\phi(X)$ and $\psi(N)$; i.e.,

$$\theta(X,N) = \phi(X) \cdot \psi(N) \quad (8)$$

Substituting in Eq. (6), using the expression in Eq. (8) will yield, after dividing by θ for both sides,

$$\frac{\phi''(X) - F\phi'(X)}{\phi(X)} = \frac{\psi'(N)}{\psi(N)} \quad (9)$$

The right hand side of Eq. (9) is a function of N only, and its left hand side is a function of X only, which means that both sides must be equal to a common constant. The latter can be any one of four possibilities: a zero, a real positive number (λ^2), a real negative number ($-\lambda^2$) or an imaginary number ($\pm\lambda^2 i$). The first three possibilities are rejected since they will result in a nonoscillatory time solution at any position X, which does not fit the problem boundary conditions. The fourth possibility, ($\pm\lambda^2 i$), is the only choice which requires the solution of the two linear differential equations

$$\left.\begin{aligned} \phi''(X) - F\phi'(X) - (\pm i\lambda^2)\phi(X) &= 0 \\ \psi'(N) - (\pm i\lambda^2)\psi(N) &= 0 \end{aligned}\right\} \quad (10)$$

At this stage, two solutions will be generated in solving Eq. (10), using in one the positive sign ($+\lambda^2 i$) and using in the other the negative sign ($-\lambda^2 i$) of the imaginary constant. This is explained in Appendix A in detail. The general solution of θ (X,N) is expressed in Appendix A as Eq. (A-14), which is rewritten as

$$\theta = e^{aX}\left[B\cos(\lambda^2 N - bX) + D\sin(\lambda^2 N - bX)\right] \quad (11)$$

where B, D are arbitrary constants, and a, b are parameters given by Eq. (A-6).

V. Boundary Conditions

At the fluid entrance section ($X = 0$), the periodic temperature fluctuations, shown in Fig. 2 is written as:

$$T(0,\tau) = T_m + \Delta_0 \sin 2\pi f \tau$$

or in dimensionless form as

$$\theta(0,N) = \sin 2\pi N \tag{12}$$

Substituting in Eq. (11) at X=0 using Eq. (12) and comparing the sine and cosine coefficients, then

$$\begin{aligned} B &= 0 \\ D &= 1 \\ \lambda^2 &= 2\pi \end{aligned} \tag{13}$$

Hence, the solution for the dimensionless temperature (θ) becomes

$$\theta = \exp(aX) \sin(2\pi N - bX) \tag{14}$$

This means that as X increases (away from the entrance section), the amplitude of the sinusoidal fluctuations will decrease (a is always a negative quantity). Note that both the fluid and the matrix are assumed to be approximately at the same temperature.

For the periodic temperature fluctuations, at any section X, the temperature T should be such that

$$T(x,\tau) = T(x, \tau + n/f)$$

or in dimensionless form

$$\theta(X,N) = \theta(X, N+n) \tag{15}$$

where n is any integer representing the number of cycles. One can see that this boundary condition is satisfied when Eq. (14) is used for any number of cycles n.

A simple corollary could be derived from Eq. (14) about the mean temperature of the matrix at any distance x. By obtaining the mean value of the temperature $T(x,\tau)$ during one cycle, i.e., $[f \int_0^{1/f} T(x,\tau)\, d\tau]$, the mean temperature at the entrance section, T_m will be the same for any other section. The amplitude, however, will decrease as mentioned above.

VI. Temperature Profile

The solution of the temperature profile along a one-dimensional flow through a porous matrix is represented by Eq. (14) and is sketched in Fig. 3. The temperature cycle at a distance x from the fluid inlet section will experience a time lag τ^*, determined from Eqs. (5) and (14) as

$$\tau^* = \frac{bx}{2\tau\sqrt{f\alpha_e}} \tag{16}$$

The amplitude, on the other hand, will monotonically decrease by an exponential function, as x increases. At a distance L from the fluid inlet section, the temperature amplitude will be Δ_L, given by the logarithmic decrement written as

$$\ln\frac{\Delta_L}{\Delta_0} = aL\sqrt{\frac{f}{\alpha_e}} \tag{17}$$

where the parameters a and b are determined from Eq. (A-6) as

$$\left.\begin{aligned} a &= \frac{F}{2} - \frac{1}{2}(F^4 + 64\pi^4)^{1/4} \cos\delta/2 \\ b &= \frac{1}{2}(F^4 + 64\pi^4)^{1/4} \sin\delta/2 \end{aligned}\right\} \tag{18}$$

and

$$\delta = \tan^{-1}\frac{8\pi}{F^2}$$

The relationship between the parameter a and the flow factor F can be directly obtained from Eq. (18) as

$$a = \frac{F}{2} - \frac{1}{2\sqrt{2}}\sqrt{F^2 + \sqrt{(F^4 + 64\pi^2)}} \tag{19}$$

The relationship between a and F is plotted as shown in Fig. 4. The parameter a is always negative. Increasing the flow factor F will decrease the absolute value of a, thus requiring a larger matrix length L to damp a given amplitude ratio. Also, as seen from Eqs. (7) and (17), the use of a porous matrix having large

thermal conductivity (K_e) is preferred in order to reduce the matrix length L.

VII. Design Sequence

To illustrate the use of the above equations and the sequence followed, the following numerical example is given. Suppose that the air temperature profile at the matrix entrance section (X=0) has an amplitude Δ_0 of 0.05°C and that the air temperature frequency f could be approximated as four cycles/hr; then in order to reduce the air temperature amplitude down to 0.025°C at the exit section, a porous matrix of length L will be determined according to the following steps:

(1) Select the material to be used for the solid matrix and determine the transport properties ρ, C, K, and α at the mean operating temperature for both the fluid and solid matrix.

(2) Determine the porosity P either from specifications or by choosing a trial value for the design to be changed later. The equivalent properties ρ_e, C_e, K_e, and α_e could be determined using Eqs. (3) and (4).

(3) From the temperature frequency f, mass flux G_f and properties C_f, K_e and α_e, determine the dimensionless flow factor F using Eq. (7).

(4) Knowing the flow factor F the parameter a is evaluated from Eq. (19).

(5) Determine the length L required to satisfy the logarithmic decrement [$\ln (\Delta_L/\Delta_0)$] of Eq. (17).

(6) Repeat the above steps for different porosity values, matrix materials, air mass flow, frequency, etc., for parameterization.

Table 1 lists the results of one design trial at an arbitrary porosity of 0.2. The air mass flux G_f is calculated as 10,000 kg/(hr. m^2) at an air velocity of about 454 ft/min, and at an air temperature of 20°C (68°F). Four types of matrix materials were tried in Table 1, cotton wool, steel, brass and aluminum.

It can be seen from Table 1 that the effective diffusivity α_e is nearly independent of the porosity p for metallic matrices due to the large solid properties K_s and $\rho_s C_s$ compared to the fluid (air). However, as the porosity decreases, the equivalent thermal conductivity K_e decreases and the flow factor F decreases, which in turn will lead to a smaller matrix length L for damping the temperature fluctuations. Also, the smaller the mass flux G_f, and the higher the frequency f, the smaller the matrix length L as evidenced from Eqs. (7), (17), and (19). For the above numerical example, a brass matrix with a porosity of 0.2 and a length of 0.62 m would be theoretically sufficient to damp the temperature amplitude to one-half.

In practice, a somewhat longer matrix would be required to offset the differences between matrix and pores temperatures, which are neglected in Section II. The order of magnitude of the errors caused by using the approximate differential equation, Eq. (2), instead of the accurate one, Eq. (1), will be addressed in another report.

Table 1. Effect of matrix material on required matrix size for the given example

Matrix material	Solid density, kg/m^3	Solid sp. heat C_s, Wh/kg°C	Solid thermal cond. K_s, W/m°C	Equivalent solid thermal diffusivity α_s, m^2/hr	Equivalent[a] thermal cond. K_e, W/m°C	α_e, m^2/hr	Flow factor F	a	L, m
Cotton wool	80	0.360	0.042	0.0015	0.039	0.0017	1486	-3×10^{-7}	47,600
Steel	7750	0.134	39.5	0.0381	31.6	0.0382	8.6	-0.06	1.13
Brass	8500	0.107	106.4	0.1170	85.1	0.117	5.6	-0.19	0.62
Aluminum	2700	0.249	196.5	0.2925	157.2	0.2925	4.8	-0.27	0.69

[a]Properties of air at 20°C:

ρ_f = 1.205 kg/m^3, K_f = 0.0259 W/m°C

α_f = 0.0771 m^2/hr, C_f = 0.279 Wh/kg°C

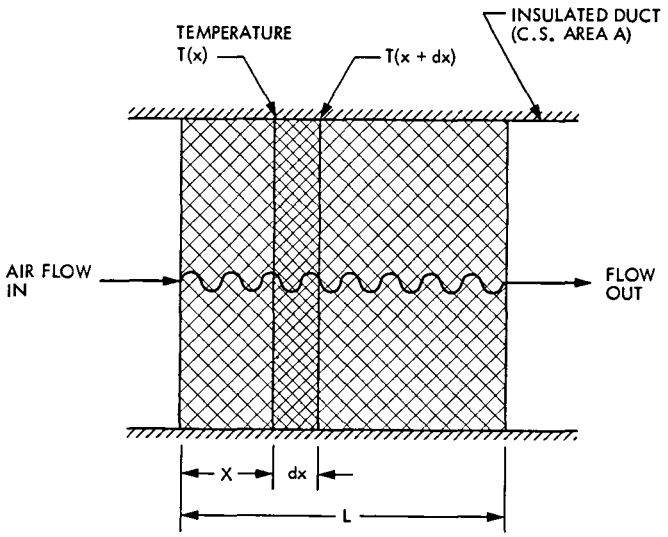

Fig. 1. Fluid through a porous matrix

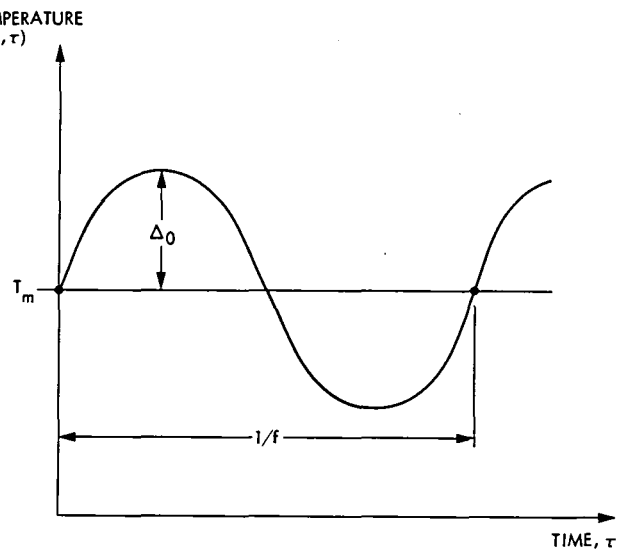

Fig. 2. Temperature fluctuations at the fluid entrance section (*X*=0)

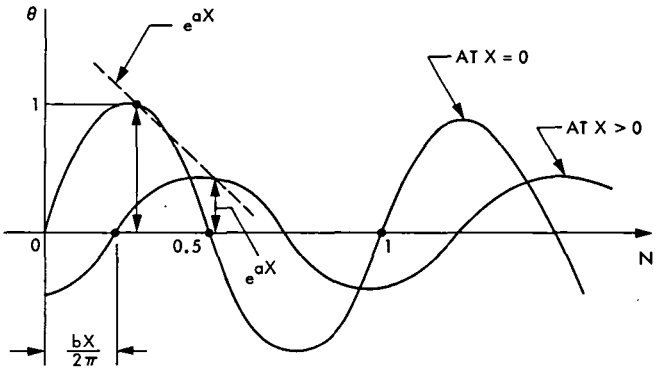

Fig. 3. Temperature oscillation at a distance *X* from the fluid entrance section

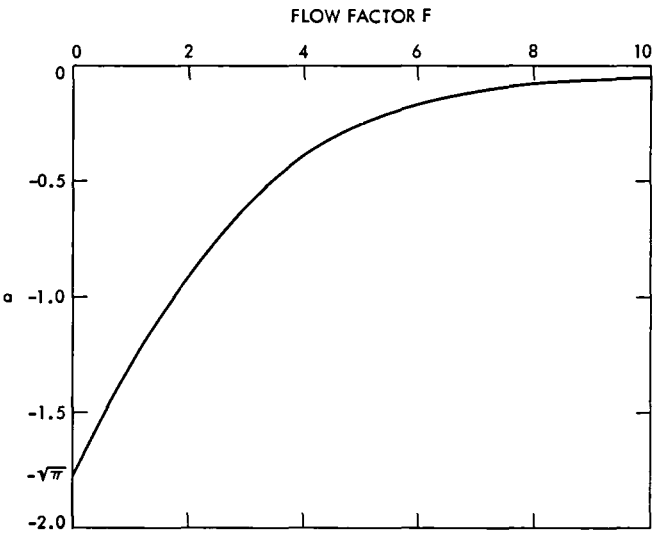

Fig. 4. Relationship between *a* and flow factor *F* for small values of *F*

Appendix A

Solution of the System Differential Equation

The two functions $\phi(X)$ and $\psi(N)$, expressed in Eq. (10), could be obtained by using either the positive imaginary constant $(i\lambda^2)$ or its negative conjugate $(-i\lambda^2)$. The two possible solutions can be generated for each case as explained next.

I. Taking the Positive Constant $(+ i\lambda^2)$

In this case, Eq. (10), in the text, can be written as

$$\left.\begin{aligned} \phi''(X) - F\phi'(X) - i\lambda^2\phi(X) &= 0 \\ \psi'(N) - i\lambda^2\psi(N) &= 0 \end{aligned}\right\} \quad \text{(A-1)}$$

The two functions $\phi(X)$ and $\psi(N)$ will then be solved as

$$\left.\begin{aligned} \phi(X) &= B_1 \exp(S_1 X) + B_2 \exp(S_2 X) \\ \psi(N) &= B_3 \exp(i\lambda^2 N) \end{aligned}\right\} \quad \text{(A-2)}$$

where B_1, B_2, and B_3 are arbitrary constants and S_1, S_2 are the roots of the auxiliary equation

$$S^2 - FS - i\lambda^2 = 0 \quad \text{(A-3)}$$

The roots S_1 and S_2 can be determined by solving Eq. (A-3) as

$$S_{1,2} = \frac{F \pm \sqrt{F^2 + 4i\lambda^2}}{2} \quad \text{(A-4)}$$

Using the complex number algebra, the square root in Eq. (A-4) can be rewritten in terms of the angle parameter δ. Accordingly, the roots S_1 and S_2 are expressed as:

$$\left.\begin{aligned} S_1 &= r + bi \\ S_2 &= a - bi \end{aligned}\right\} \quad \text{(A-5)}$$

where

$$\left.\begin{aligned} r &= \frac{F}{2} + \frac{1}{2}(F^4 + 16\lambda^4)^{1/4} \cos\delta/2 \\ a &= \frac{F}{2} - \frac{1}{2}(F^4 + 16\lambda^4)^{1/4} \cos\delta/2 \\ b &= \frac{1}{2}(F^4 + 16\lambda^4)^{1/4} \sin\delta/2 \end{aligned}\right\} \quad \text{(A-6)}$$

and

$$\delta = \tan^{-1}\frac{4\lambda^2}{F^2}$$

The solution of the dimensionless temperature θ_+ using the positive sign can thus be written as

$$\theta_+ = \exp(i\lambda^2 N)\,[B_1' \exp(r + bi)X + B_2' \exp(a - bi)X] \quad \text{(A-7)}$$

where the arbitrary constant B_3 is combined with the constants B_1 and B_2

II. Taking the Negative Constant $(- i\lambda^2)$

In this case, Eq. (10) in the text can be written as:

$$\left.\begin{aligned} \phi''(X) - F\phi'(X) + i\lambda^2\phi(X) &= 0 \\ \psi'(N) + i\lambda^2\psi(N) &= 0 \end{aligned}\right\} \quad \text{(A-8)}$$

The functions $\phi(X)$ and $\psi(N)$ after solving Eq. (A-8) will be written as

$$\left.\begin{aligned} \phi(X) &= B_4 \exp(S_1' X) + B_5 \exp(S_2' X) \\ \psi(N) &= B_6 \exp(-i\lambda^2 N) \end{aligned}\right\} \quad \text{(A-9)}$$

where B_4, B_5, and B_6 are arbitrary constants and S'_1, S'_2 are the roots of the auxiliary equation

$$S^2 - FS + i\lambda^2 = 0 \qquad \text{(A-10)}$$

The roots S'_1 and S'_2 can be determined by a procedure similar to that used for S_1 and S_2. Therefore,

$$\left.\begin{aligned} S'_1 &= r - b\,i \\ S'_2 &= a + b\,i \end{aligned}\right\} \qquad \text{(A-11)}$$

where the parameters a, b and r are as defined by Eq. (A-6). The solution of the dimensionless temperature θ_- using the negative sign can be reduced to

$$\theta_- = \exp(-i\lambda^2 N)\,[B'_4 \exp(r - bi)\,X + B'_5 \exp(a + bi)\,X] \qquad \text{(A-12)}$$

where the arbitrary constants B'_4 and B'_5 combine the constant B_6 with B_4 and B_5.

III. General Solution

By adding the two possible solutions in Eqs. (A-7) and (A-12), the general solution of the dimensionless temperature (θ) can be reduced, after some manipulation, to

$$\begin{aligned} \theta = \exp(rX) \cdot \{&B'_1 \exp[(\lambda^2 N + bX)\,i] \\ &+ B'_4 \exp[-(\lambda^2 N + bX)\,i]\} \\ &+ \exp(aX)\,\{B'_2 \exp[\lambda^2 N - bX)\,i] \\ &+ B'_5 \exp[-(\lambda^2 N - bX)\,i]\} \end{aligned} \qquad \text{(A-13)}$$

Since the value of r (from Eq. (A-6)), is always positive, no solution would exist from the first term in Eq. (A-13) where it is not conceivable to have an infinite temperature θ at X equals ∞. This will lead to the elimination of the arbitrary constants B'_1 and B'_4. The same conclusion would have been reached for the second term in Eq. (A-13) if the value of a was positive at any time. It can be easily proven that the value of a from Eq. (A-6) is always negative at any value of F or λ. The general solution of θ, therefore, will be only the second term of Eq. (A-13), which can be rewritten in the trigonometric form as

$$\theta = \exp(aX)\,[B\cos(\lambda^2 N - bX) + D\sin(\lambda^2 N - bX)] \qquad \text{(A-14)}$$

where B and D are arbitrary constants to be determined further from the initial and boundary conditions.

Definition of Symbols

A cross section area

B arbitrary constant

b parameter

C specific heat

D arbitrary constant

F dimensionless flow number

f frequency

G mass flux (flow rate per unit area)

H average heat transfer coefficient between solid matrix and fluid in pores

i $\sqrt{-1}$

K thermal conductivity

L matrix thickness

m mass flow rate

N number of cycles

p porosity (pore volume/total volume)

T temperature

X dimensionless distance

x distance measured from the fluid entrance

α thermal diffusivity = $K/\rho c$

Δ amplitude

δ angle parameter

ζ average pore surface area per unit matrix volume

θ dimensionless temperature

λ parameter

ρ density

τ time elapsed

ϕ,ψ functions

Suffixes

e "effective" property for matrix

f fluid

s solid matrix

m mean or average

References

1. Burch, D. M., and Peavy, B. A., "Transient Temperature Distribution in Heat – Generating Transpiration-Cooled Tubes and Plates," *J. Heat Transfer*, ASME Trans. Series C, Vol. 97, Aug. 1975.

2. Rohsensow, W. M., and Hartnett, J. P., *Handbook of Heat Transfer*, McGraw Hill Book Co., N.Y., 1973, Ch. 3.

3. Schneider, P. J., "Temperatures and Thermal Stresses in Transpiration-Cooled Power Producing Plates and Tubes," *Jet Propulsion*, Vol. 27, Aug. 1957, pp. 882-889.

4. Schneider, P. J., "Numerical Method for Porous Heat Sources," *J. Appl. Phys.*, Vol, 24, No. 3, Mar. 1973, pp. 271-274.

5. Green, L., "Gas Cooling of a Porous Heat Source," *J. Appl. Mech., Trans. ASME*, Vol. 19, No. 2, 1952, pp. 173-178.

6. Weiner, M. M., and Edwards, D. K., "Simultaneous Conduction, Convection, and Radiation in a Porous Bed," Proceedings of the 1963 Heat Transfer and Fluid Mechanics Institute held at the California Institute of Technology, Pasadena, Calif., June 12-14, 1963. pp. 236-250. Printed and distributed by Stanford Univ. Press, Stanford, Calif.

7. Chapman, A. J., *Heat Transfer*, Macmillan Publishing Co., Inc., Third edition, 1974, Ch. 4.

NASA–JPL–Coml., L.A., Calif.

End of Document